Nanodiamond-coated tungsten needle tips: Fabrication and characterization of a novel electron source designed for high brightness femtosecond laser-induced emission

Alexander Tafel

Erlangen 2020

Nanodiamond-coated tungsten needle tips: Fabrication and characterization of a novel electron source designed for high brightness femtosecond laser-induced emission

Alexander Tafel

Der naturwissenschaftlichen Fakultät
der Friedrich-Alexander-Universität Erlangen-Nürnberg
zur
Erlangung des Doktorgrades Dr. rer. nat.

vorgelegt von

Alexander Tafel

Als Dissertation genehmigt
von der naturwissenschaftlichen Fakultät
der Friedrich-Alexander-Universität Erlangen-Nürnberg
Tag der mündlichen Prüfung: 18.09.2020

Vorsitzender des
Promotionsorgans: Prof. Dr. Georg Kreimer

Gutachter:
Prof. Dr. Peter Hommelhoff
Prof. Dr. Thomas Fauster

List of acronyms

a.k.a.	also known as
DLA	dielectric laser accelerator
PA	particle accelerator
CRT	cathode ray tube
EM	electron microscopy
TEM	transmission electron microscopy
STM	scanning tunneling microscopy
rms	root mean square
cw	continuous wave
dc	direct current
VBM	valence band maximum
CBM	conduction band minimum
EA	electron affinity
NEA	negative electron affinity
PEA	positive electron affinity
CVD	chemical vapour deposition
HPHT	high pressure high temperature
NCD	nanocrystalline diamond
UNCD	ultra-nanocrystalline diamond
MEMS	microelectromechanical systems

Abstract

Electron beams are powerful tools with applications ranging from treating cancer to recording ultrafast microscopic movies. The temporal and spatial resolution of the latter is limited by the electron pulse duration and beam emittance, respectively. However, the electron sources used in state of the art ultrafast electron microscopes and our photonic laser acceleration setup were developed for dc operation. The high brightness Schottky and cold field emitters suffer from emission instability when triggered by femtosecond laser pulses.

The main goal of this work was to invent, fabricate and characterize a robust high brightness emitter designed for femtosecond laser-triggered operation: We present nanodiamond-coated tungsten needle tips.

This geometry results in a large DC field enhancement at the emitter apex, which enables operation at GV/m electrostatic fields. These large fields and the resulting acceleration of emitted electrons are crucial for mitigating space charge effects and achieving high beam brightness during high current density operation. To better understand the electrostatic field distribution at nanometer-sized emitters, we developed a differential phase contrast technique in a transmission electron microscope. Measuring electron deflection allows us to determine the 3D electrostatic field with nanometer resolution, even during dc field emission. We measured up to 2.92 V/nm at a 20 nm sized tungsten emitter and achieved quantitative agreement between experiment and simulation.

Another major advantage of the needle shape is the small effective electron source size both in dc and laser-triggered emission. This leads to a small source emittance, which is one of the key parameters for realizing a photonic particle accelerator on a chip, especially at low injection energies. The lower the injection energy is, the more compact the injector unit can be built due to reduced electrostatic field breakdown. We demonstrated electron acceleration using optical near fields in the vicinity of a periodic nanostructure with

energies as low as 9.6 keV.

As emitter material, we chose diamond as it is not only mechanically and chemically robust, but also exhibits high thermal conductivity. These properties promise a robust emitter which can withstand the high laser intensity of femtosecond laser pulses. Furthermore, the diamond surface exhibits negative electron affinity if it is terminated by hydrogen. Not only does this significantly lower the work function, it also boosts the photoelectron yield as the photoexcited carriers can be emitted into vacuum even after thermalizing to the conduction band minimum. The tungsten substrate was chosen as a metallic contact which can easily be fabricated in the desired needle shape.

We report a reliable fabrication recipe, which is based on dip-seeding of electrochemically etched tungsten in nanodiamond suspension, dry-blowing with pressurized nitrogen and microwave plasma-enhanced chemical vapor deposition of diamond. Electron energy loss spectroscopy and electron diffraction in a high resolution transmission electron microscope confirm conformal diamond coating. The crystallites have a columnar shape, are 20 nm in size and have graphitic grain boundaries.

Based on the band diagram of this heterostructure, we propose an emission model, which explains the femtosecond laser-induced multiphoton emission from the ultraviolet to the infrared (235-1932 nm). Depending on the laser wavelength and intensity, excitation across the direct band gap or direct emission into vacuum dominates, which is identified by the number of photons needed to emit one electron. Furthermore, emission is stable for all wavelengths and bunch charges investigated. We infer a normalized emittance of $<$0.20 nm rad and a normalized peak brightness of $> 1.2 \cdot 10^{12}$ A m^{-2} sr^{-1}. These values are already comparable to published values even though we used the geometrical source size for the calculation. Therefore, our results are promising for a future use of diamond-coated tungsten tips as high brightness ultrafast electron sources.

Zusammenfassung

Elektronenstrahlen sind leistungsstarke Werkzeuge, deren Anwendungen von Krebsbehandlung bis zur Aufnahme ultraschneller mikroskopischer Filme reichen. Die zeitliche und räumliche Auflösung der letzteren ist durch die Elektronenpulsdauer bzw. die Strahlemittanz begrenzt. Die in den modernsten ultraschnellen Elektronenmikroskopen sowie auch in unserem photonischer Laser-Beschleunigungsaufbau verwendeten Elektronenquellen wurden jedoch für den Gleichstrombetrieb entwickelt. Ein Nachteil von diesen Schottky- und Feldemittern ist, dass sie unter Instabilität leiden, wenn sie durch Femtosekunden-Laser gepulst werden.

Das Hauptziel dieser Arbeit war die Erfindung, Herstellung und Charakterisierung eines robusten Elektronenemitters mit hohem Richtstrahlwert, der für den Femtosekunden-Laser-getriggerten Betrieb ausgelegt ist: Wir präsentieren Nanodiamant-beschichtete Wolframspitzen.

Die Geometrie führt zu einer großen DC-Feldverstärkung an der Emitterspitze, was den Betrieb bei elektrostatischen Feldern von GV/m ermöglicht. Diese großen Felder und die daraus resultierende Beschleunigung der emittierten Elektronen sind entscheidend für die Abschwächung von Raumladungseffekten und das Erreichen eines hohen Strahrichtwerts bei Betrieb mit hoher Stromdichte. Um die elektrostatische Feldverteilung an nanometrischen Emittern in Nanometergröße besser zu verstehen, haben wir eine differentielle Phasenkontrasttechnik in einem Transmissionselektronenmikroskop entwickelt. Die Messung der Elektronenablenkung ermöglicht es uns, das elektrostatische 3D-Feld mit Nanometer-Auflösung zu bestimmen, sogar während der Feldemission. Wir haben bis zu 2,92 V/nm an einem 20 nm großen Wolfram-Emitter gemessen und eine quantitative Übereinstimmung zwischen Experiment und Simulation erreicht.

Ein weiterer großer Vorteil der Nadelform ist die geringe effektive Größe der Elektronenquelle sowohl bei der Gleichstrom- als auch bei der lasergetriggerten Emission. Dies führt zu einer kleinen Quellen-Emittanz, die einer der

Schlüsselparameter für die Realisierung eines photonischen Teilchenbeschleunigers auf einem Chip ist, insbesondere bei niedrigen Injektionsenergien. Je geringer die Injektionsenergie ist, desto kompakter kann die Injektionseinheit aufgrund des elektrostatischen Felddurchbruchs gebaut werden. Wir demonstrierten die Elektronenbeschleunigung mit optischen Nahfeldern in der Nähe einer periodischen Nanostruktur mit Energien von nur 9,6 keV.

Als Material für den neuartigen Emitter wählten wir Diamant, da er nicht nur mechanisch und chemisch robust ist, sondern auch eine hohe Wärmeleitfähigkeit aufweist. Diese Eigenschaften versprechen einen robusten Emitter, der der hohen Laserintensität von Femtosekunden-Laserpulsen standhalten kann. Darüber hinaus weist die Diamantoberfläche eine negative Elektronenaffinität auf, wenn sie durch Wasserstoff terminiert wird. Dies senkt nicht nur die Austrittsarbeit erheblich, sondern erhöht auch die Photoelektronenausbeute, da die photoangeregten Ladungsträger auch nach der Thermalisierung in das Leitungsbandminimum ins Vakuum emittiert werden können. Wolfram wurde als metallischer Kontakt gewählt, da Wolfram leicht in der gewünschten Nadelform hergestellt werden kann.

Wir berichten über ein zuverlässiges Herstellungsrezept, das auf dem Bekeimen von elektrochemisch geätztem Wolfram in Nanodiamantsuspension, dem Trockenblasen mit Stickstoff und der mikrowellenplasmaunterstützten chemischen Gasphasenabscheidung von Diamant basiert. Elektronenenergieverlustspektroskopie und Elektronenbeugung in einem hochauflösenden Transmissionselektronenmikroskop bestätigen eine konforme Diamantbeschichtung. Die Kristallite haben eine säulenförmige Form, sind 20 nm groß und haben graphitische Korngrenzen.

Basierend auf dem Banddiagramm dieser Heterostruktur schlagen wir ein Emissionsmodell vor, das die Femtosekundenlaser-induzierte Multiphotonenemission vom Ultraviolett bis zum Infrarot (235-1932 nm) erklärt. Abhängig von der Laserwellenlänge und -intensität dominiert die Anregung über die direkte Bandlücke oder die direkte Emission ins Vakuum, die durch die Anzahl der zur Emission eines Elektrons benötigten Photonen identifiziert wird. Darüber hinaus ist die Emission für alle untersuchten Wellenlängen und Pulsladung stabil. Wir schließen auf eine normalisierte Emittanz von <0,20 nm rad und einen normalisierten Strahlrichtwert von $> 1,2 \cdot 10^{12}$ A m^{-2} sr^{-1}. Diese Werte sind bereits mit publizierten Werten vergleichbar, obwohl wir für die Berechnung die geometrische Quellengröße verwendet haben. Daher sind unsere Ergebnisse vielversprechend für einen zukünftigen Einsatz diamantbeschichteter Wolframspitzen als ultraschnelle Elektronenquellen mit hohem Richtstrahlwert.

Preface

The main work of this thesis lies in the attached publications in chapter 5 - especially the work on nanodiamond-coated tungsten needle tips (Publications 5.1 and 5.2). While publication 5.3 presents a new method for measuring the electrostatic field at nanometric emitters, publications 5.4 and 5.5 show the need for a novel electron emitter designed for femtosecond laser-induced operation.

To acknowledge the work of all authors, I will use the ”we” form, whenever one of the publications is mentioned and the ”I” form otherwise.

The following chapters have the purpose to introduce the theoretical foundation for the publications as well as to integrate the publications into a larger context. Therefore, the scope of the following chapters is not to cover the entire research field of the respective topics. On the contrary, the goal is to neither overcomplicate nor to oversimplify the relevant theory for this work. Ideally, the following chapters enable the reader to see the main focus of this thesis:

The value of researching needle-shaped electron emitters and the potential of diamond-coated tungsten tips as novel electron emitters.

Contents

List of acronyms **vii**

Abstract **ix**

Zusammenfassung **xi**

Preface **xiii**

1 Characterization of particle beams **1**
- 1.1 Emittance 1
- 1.2 Brightness 3
- 1.3 Requirements of modern pulsed applications 3

2 Electron sources and their applications **7**
- 2.1 Thermionic emitters 8
- 2.2 Schottky emitters 9
- 2.3 Cold field emitters 10

3 Photoelectron emission from metallic surfaces **13**
- 3.1 Classical Photoemission 13
- 3.2 Nonlinear Photoemission 14

4 Diamond **17**
- 4.1 Properties and applications 17
- 4.2 Electron affinity 18
- 4.3 Nanocrystalline diamond 18
- 4.4 Diamond as an electron emitter 20
  - 4.4.1 Cold field emission 20
  - 4.4.2 Photoemission 21

Bibliography **31**

5 Publications **33**
5.1 *Diamond and Related Materials 2019* 35
5.2 *Physical Review Letters 2019* 43
5.3 *Applied Physics letters 2019* 51
5.4 *Journal of Applied Physics 2018* 58
5.5 *Journal of Physics B 2016* 70

Additional publications **79**

Acknowledgement **81**

Chapter 1

Characterization of particle beams

Many modern techniques and research fields like ultrafast electron microscopy [1, 2, 3, 4], ultrafast electron diffraction [5, 6, 7, 8], free electron lasers [9] and dielectric laser accelerators (DLAs) (see. 1.3) require pulsed femtosecond to attosecond electron beams with high spatial beam quality. In this chapter, I will introduce common measures of particle beam quality and elaborate on the beam requirements of DLAs.

1.1 Emittance

Every particle beam has a characteristic size $\sigma(z)$ and divergence θ at a given longitudinal position z. In the focal point, the product of σ and θ is called the transverse emittance ϵ. More generally speaking, the emittance is a measure of the phase space area occupied by the particle beam. The single particles are described by their transverse position x and angle $x' = \arctan(\frac{p_x}{p_z})$, where p_x and p_z are the transverse and longitudinal momenta, respectively. In Fig. 1.1, the phase space of a freely propagating particle ensemble is illustrated in focus, in the far field and after beam expansion to $\sqrt{2}$ of the focal size, which is a widely used value (characterized by β^*, the interested reader is referred to [10]).

Even though the beam size changes with propagation distance, the occupied phase space - and therefore also the emittance - remains constant. The transverse root mean square (rms) emittance is defined as

$$\epsilon_x = \sqrt{\langle x^2 \rangle \langle x'^2 \rangle - \langle xx' \rangle^2} \tag{1.1}$$

where the term $\langle xx' \rangle$ describes correlation between transverse momentum

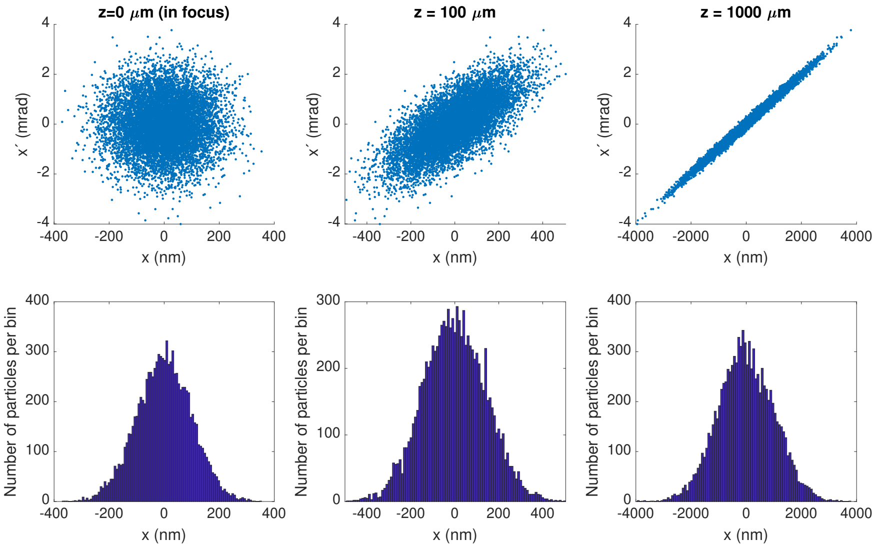

Figure 1.1: Transverse phase space of a freely propagating Gaussian electron beam with 100 pm rad rms emittance at three different longitudinal positions. In focus (left), there is no correlation between position and angle, but at the β^* position (center) and in the far field (right), there is correlation. The emittance is conserved if space charge can be neglected.

and space. This term vanishes in the focus of a particle beam. For curved surfaces of emitters $\langle xx' \rangle$ is nonzero. This means that the emittance of curved emitters, e.g. a hemisphere, can be lower compared to flat surfaces with the same geometric source size. In the literature, this effect is often explained via the term effective source size as the particles seem to originate from a surface which is smaller than the geometric source size of the emitter [11, 12]. For tungsten needle tips, the effective source size has been measured to be below 1 nm under direct current (dc), continuous wave (cw)[13, 11] and femtosecond laser-induced electron emission[12], approximately one order of magnitude smaller than the geometric source size. This is one of the reasons why state of the art electron microscopes are equipped with - and why we focused our work on - tip-shaped emitters.

For a beam moving along the z-axis, $x' \approx \frac{p_x}{\beta\gamma c}$, where β is the particle speed in unit of the speed of light and $\gamma = (1 - \beta^2)^{(-1/2)}$ is the Lorentz factor. Therefore, only the *normalized* emittance $\epsilon_{\text{norm}} = \beta\gamma\epsilon$ is conserved under uniform acceleration of the beam.

1.2 Brightness

Depending on the exact requirements of the application, not only the emittance but also the particle current J is relevant. While the emittance can be reduced via spatial filtering of the beam, this always comes at the cost of particle loss. As an example, the process time of electron beam lithography depends on the minimum desired resolution of the desired pattern.
To account for this, I introduce the brightness B, which is a measure for the phase space population. For best comparison with the most relevant literature [14, 15] for this work, I use the following definition for the normalized rms brightness:

$$B_{\mathrm{norm}} = \frac{J}{4\pi\epsilon_{norm,x}\epsilon_{norm,y}} \tag{1.2}$$

The higher the brightness, the more particles can be focused to a given spot size and divergence angle, often determined by the use case. In the case of pulsed beams, not only the average, but also the peak brightness is of importance, e.g. for pump probe experiments, free electron lasers and dielectric laser accelerators (DLAs).
The physical limit of the normalized brightness $B_{\mathrm{norm,max}}$ for fermions is given by the Pauli exclusion principle and the Heisenberg uncertainty of energy and time. For an energy width of 0.3 eV, this limit is $5 \cdot 10^{19}$ A m^{-2} sr^{-1} [16]. As we will show in chapter 2, typical brightness values are orders of magnitudes below this limit.

For more information on beam emittance and brightness, the reader is referred to [10, 17].

1.3 Requirements of modern pulsed applications

Treating all potential applications is beyond the scope of this thesis, therefore we will focus on DLA [18], which is directly related to this work. With a concise introduction of DLAs as an example application, we will deduce the approximate requirements for the particle beam emittance.

Dielectric laser acceleration

For a specific target particle energy, the length of today's particle accelerators (PAs) is limited by the acceleration gradient G, i.e. the energy gain (dE) per unit distance (dz).

$$G = \frac{\mathrm{d}E}{\mathrm{d}z} = q\frac{\mathrm{d}F}{\mathrm{d}z}$$

where e is the charge and F is the electric field.

Most of today's PAs including user facilities such as the Large Hadron Collider and the Linac Coherent Light Source are based on the excitation of electromagnetic modes in cavities. For those PA types G is ultimately limited by the damage threshold field F_{th} of the cavity material at the drive frequency. In conventional accelerators with metal structures and GHz frequencies, F_{th} is on the order of 100 MV/m and typical accelerating fields on the order of 20 MV/m [19]. As the damage threshold field of dielectrics at optical frequencies (typically $100 - 300$ THz) exceeds this value by up to two orders of magnitude [20], DLAs have the potential to shrink PAs drastically. Even a complete photonic PA on a silicon chip seems possible after the demonstration of acceleration [21, 22, 23], deflection [24] and focusing [25] using only optical near fields. To achieve the high peak electric fields without destroying the dielectric nanostructures, (sub-)picosecond laser pulses are used [26, 21, 22, 23, 24, 27, 28], the electron pulse duration should be shorter than the laser pulse duration. The highest average gradient experimentally shown to date is 850 MeV/m over 0.5 mm [29]. However, this advantage of working with μm scale wavelengths comes along with the challenge of phase space acceptance, which is directly linked to the drive wavelength.

For continuous acceleration, the particles speed needs to be matched with the phase velocity of the acceleration mode. As a consequence, the acceleration mode is an optical near field mode which decays exponentially from the surface (e.g. decay length $\delta = 100$ nm at 2 μm wavelength and $\beta = 0.32$ [26]). By exciting the same mode from two periodic structures (e.g. two rows of pillars and Bragg mirror [26, 28] or double sided illumination [27]), a hyperbolic cosine mode with homogeneous field strength in the center can be excited. An example structure is shown in Fig. 1.2, which illustrates the demands on the electron beam: To avoid large particle loss at the aperture and to achieve uniform acceleration, the channel width d and the electron beam radius needs to be smaller than δ. To avoid additional particle loss during propagation through the structure, the acceptable divergence of the beam is on the order of $d/2L$, where L is the structure length. For $L = 100\mu$m, this results in $x' \approx 1$ mrad and $\epsilon < 0.1$ nm rad. The beam expansion of such a beam is illustrated in Fig. 1.1. Simulations show that comparable parameters (ϵ=100 pm rad, d=420 nm) suffice to guide and accelerate an electron beam from 83 keV to 1 MeV within 5 mm with 56 % survival rate of the particles [30]. The required brightness on the other hand highly depends on

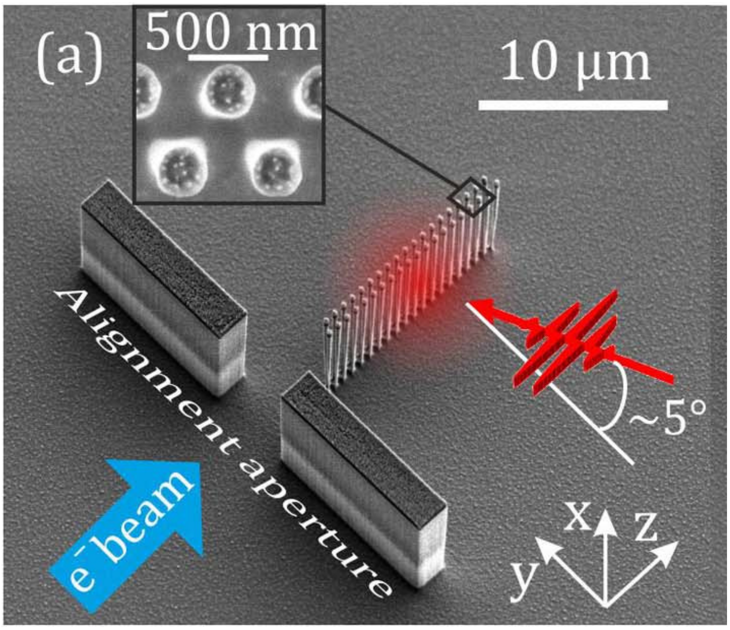

Figure 1.2: Setup of a DLA experiment with comparably short structure length (12 μm). The electron beam is focused into the 200 nm channel of the periodic nanostructure. The laser pulse excites an optical near field mode inside the channel. If the phase velocity of this mode is matched to the speed of the electrons, they are synchronously accelerated. Modified from [26].

the exact parameters. Nevertheless, the brightness is the key parameter for DLAs as it determines the achievable current for the required emittance. As an example, one electron per pulse at 30 keV (β=0.32) with a pulse duration of 100 fs requires a normalized peak brightness better than $1.4 \cdot 10^{13}\,\mathrm{A\,m^{-2}}$ and a normalized emittance better than 35 pm rad.

In publication 5.2, we present first measurements of the emittance and brightness of diamond-coated tungsten tips. Whereas the effective source size can be much smaller than the geometric source size, we used the geometric size as a first estimation of emittance and brightness. We infer a normalized emittance of < 200 pm rad and a normalized peak brightness of $> 1.2 \cdot 10^{12}\,\mathrm{A\ m^{-2}\,sr^{-1}}$. As these values represent only conservative bounds, this underlines the potential of diamond-coated tungsten tips.

For more details on DLAs the reader is referred to [19, 31, 25]. In the next chapter, we will introduce commonly used electron sources, their properties and operation principle.

Chapter 2

Electron sources and their applications

The invention of the thermionic cathode by Thomas Edison in 1883 and the discovery of the electron by E. Wiechert and J.J. Thomson in 1897 led to countless applications of electron beams in industry and science including the first diodes, cathode ray tubes (CRTs), PAs, electron lithography and electron microscopy (EM). PAs are used for cancer radiation therapy and led to the discovery of numerous particles like the Higgs boson [32, 33] . While television on CRTs has entertained & informed our society for decades, EM revolutionized imaging and material characterization due to the ability of focusing electrons to sub-nanometer waist size. Even single atoms can be resolved in transmission electron microscopy (TEM) and scanning tunneling microscopy (STM). As diverse as the applications of free electron beams are, as diverse are the requirements and properties of the electron sources.

In molecules and solids, electrons interact with the nuclei and the remaining electrons of respective elements via the Coulomb force. This interaction leads to eigenstates of the electrons in the Coulomb potential landscape of the nuclei. In order to excite electrons into vacuum, the energy difference between these states and the vacuum level has to be overcome. At 0 K temperature, the smallest energy difference, i.e. the difference between the highest occupied state and the vacuum level, is called ionisation potential I_p for molecules and work function Φ for solids. Even though electron sources with high beam quality can be built with gases and magneto optical traps [34], most electron sources are based on solid state materials.

To achieve femtosecond electron pulses with the small emittance and high brightness requirements introduced in chapters 1.1 and 1.2, state-of-the-art research setups of today are based on electron microscopes. Whereas all electron sources in these setups were originally designed for dc operation and repurposed for laser-induced operation, the diamond-coated tungsten needle tips developed in the scope of this work are specifically designed for laser-induced electron emission. Flat photocathodes are not described in this work as the emittance is typically limited by the laser spot size, the achievable dc fields are much smaller and they are harder to implement in microscope setups. In the following sections, the most commonly used electron emitter types are introduced and related to our work.

2.1 Thermionic emitters

Electrons are fermions and therefore obey the Fermi distribution in solids:

$$f(E) = \frac{1}{1 + \exp\frac{E-\mu}{k_B T}} \tag{2.1}$$

where E is the Energy state, μ is the chemical potential, k_B is the Boltzmann constant and T is the Temperature. Strictly speaking, μ at $T = 0\,\mathrm{K}$ is called Fermi Energy E_F. In practice, however, μ and E_F are often used as synonyms. If the condition $E - E_F > \Phi$ is fulfilled, electrons can be emitted into vacuum. During the emission process, the normal component of the particle's (crystal) momentum $k_\perp$ is conserved. By taking this into account, Owen Willans Richardson derived the following law for the current density J in 1912 [35]:

$$J = AT^2 \exp\left(-\frac{\Phi}{k_B T}\right) \tag{2.2}$$

where A is a constant which was later found to be material dependent. The combination of equations 2.1 and 2.2 yields that high temperature results in an increase of both the emitted current and the energy width of the electrons. The latter deteriorates the focusability of the emitted beam due to an increased mean transverse and longitudinal momentum (see 1.1) and the velocity-dependent focal length of common electrostatic and magnetic lenses. Additionally, the high operating temperature of tungsten emitters ($\approx$ 2800 K) results in oxidation and evaporation at the surface leading to short lifetimes ($\approx$100 h). To reduce the operating temperature, materials with low work functions like LaB_6 (2.3-2.8 eV [36]), which can be operated at $\approx$ 1900 K, are favorable for applications with focused beams. Advantages of thermionic emitters are that they are typically robust, low cost and easily replaceable. Furthermore, they can deliver high currents due to a large emitting area. LaB_6 emitters can also be used in laser-triggered operation [37]. However, emittance and brightness values of such a setup remain unpublished to the best of our knowledge.

Thermionic emission from diamond-coated tungsten tips was not investigated in this work for the following reasons: Surface terminations which reduce the electron affinity - and therefore the work function (see. 4.2) - are not stable at elevated temperatures [38]. Nanodiamond itself is also unstable at temperatures above 1100 K [39] as it transfers to its thermodynamically favored phase graphite.

2.2 Schottky emitters

To reduce the operating temperature, the barrier height for electron emission can be reduced by applying a strong electrostatic field. For a flat metal surface, this reduction can be calculated by finding the maximum of the total potential E. Outside of the metal, E consists of the image potential of the emitted electron and the electrostatic potential:

$$E = -\frac{e^2}{16\pi\epsilon_0}\frac{1}{z} - eFz \tag{2.3}$$

where z is the distance to the solid-vacuum interface and F is the electric field. F reduces the barrier height by the Schottky reduction $\Delta\Phi$:

$$\Delta\Phi \equiv max(E) = \sqrt{\frac{e^3F}{4\pi\epsilon_0}} \tag{2.4}$$

To achieve large fields (>10^8 V/nm) and low barrier heights, typical Schottky emitters consist of needle-shaped tungsten with low work function coating, e.g. zirconium oxide as shown in Fig. 2.1. The emission process can be approximately described using eq. 2.2 with the reduced work function calculated from eq. 2.4 as the emission is still thermionic. A typical Schottky emitter consists of a needle-shaped tungsten wire with a reservoir of zirconia (see Fig. 2.1). When the tip is heated to its operating temperature of $\approx$ 1800 K, the zirconium oxide electromigrates to the surface and significantly lowers the work function to 2.8 eV [40].
Advantages of Schottky emitters over pure thermionic emitters include increased lifetime and higher brightness ($3 - 5 \cdot 10^{13}$ A m^{-2} sr^{-1} [41, 42, 40]) and lower energy spread (0.4 eV [40]). Disadvantages include more complex fabrication and installation. Furthermore, ultrahigh vacuum is required.

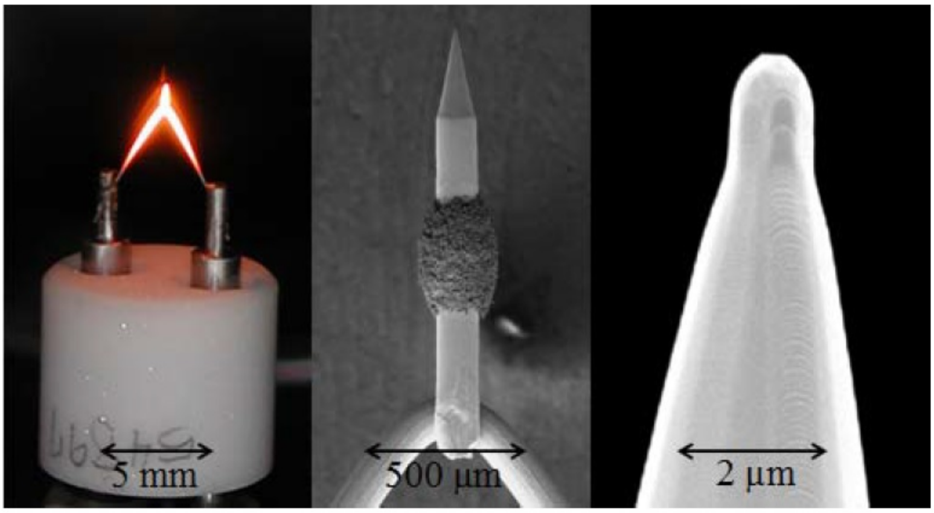

Figure 2.1: Schottky type emitter. A reservoir of zirconium oxide is located at the shaft of the needle shaped emitter. Heating increases the diffusivity of zirconia, which electromigrates to the maximum field at the apex and significantly reduces the work function. Taken from [44].

Schottky emitters are also used in femtosecond laser-triggered operation [1, 43, 14], but suffer from photocurrent decay on the timescale of hours [1, 43]. We have also observed this decay and reported it in publication 5.4. The highest published normalized peak brightness from Schottky emitters is $1.75 \cdot 10^{13}\,\mathrm{A\ m^{-2}\ sr^{-1}}$ at 13 pm rad and 2.5 electrons per pulse probe current [14]. However, the exact number of electrons per pulse at the source is not stated making it hard to compare source parameters.

Schottky emission was not investigated from diamond-coated tungsten for the same reasons stated in the previous section. For more information on Schottky type emitters, the reader is referred to [44].

2.3 Cold field emitters

Applying electric fields on the order of 10^9 V/nm bends the potential at the surface so strongly that electrons can tunnel through the narrow energy barrier into vacuum. To achieve these high fields, field emitters are typically needle shaped with a tip radius of in the nanometer range. Fowler and Nordheim calculated the emitted current density j in 1928 [45] and Murphy later refined the equation [46]:

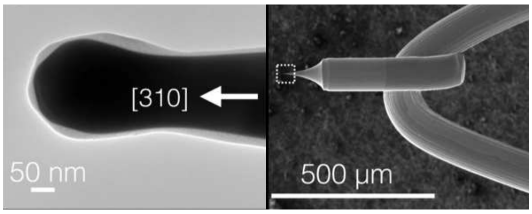

Figure 2.2: Scanning electron micrograph of a tungsten cold field emitter. The electrostatic field is enhanced at the apex of the needle shaped emitter. A [310] oriented wire is typically used as this surface facet has the lowest work function. Adopted from [15].

$$j = A(F, \Phi) \cdot \frac{F^2}{\Phi} \exp\left[-b(F, \Phi)\frac{\Phi^{2/3}}{|F|}\right] \approx A \cdot \frac{F^2}{\Phi} \exp\left(-b\frac{\Phi^{2/3}}{|F|}\right) \qquad (2.5)$$

where A and b are only weakly dependent on Φ and F, especially for low fields around the onset of field emission. For a more complete version of the equation, the reader is referred to [47]. Due to the exponential dependency on F, direct measurement of the local electric field is of high interest. We developed a method which allows direct measurement of the electrostatic field with nanometer resolution in a transmission electron microscope, even under field emission conditions (see publication 5.3). As eq. 2.5 does not depend on the temperature, field emission sources can be operated at room temperature or even at cryogenic temperatures. This is why these sources are often called cold field emitters. In practice, however, these sources are often heated to moderate temperatures to avoid adsorption of residual gases. Adsorption heavily impacts the emission behaviour due to local change in work function. This degradation is the main reason why commercially available field emitters need to undergo regular proprietary ”flashing” procedures. Furthermore, this is why cold field emitters have the highest vacuum requirements (10^{-8} Pa).

The most common cold field emitters are nanometer sized needle-shaped tungsten wires as shown in Fig. 2.2. This geometry is needed to achieve the high field strength at the apex. The main advantages of cold field emitters over all other dc emitters is that it provides the highest achievable brightness up to $1 \cdot 10^{15}$ A m^{-2} sr^{-1} [40, 48] and a reduced energy width [40]. Disadvantages over Schottky emitters include lower emission current, less stable emission, even higher vacuum requirement ($< 10^{-8}$ Pa) and the need to regularly ”flash” the tip, which is a proprietary procedure. The curved surface of the needle shaped emitters leads to an even reduced effective source size as the backtraced electron trajectories have a virtual crossover inside the tip (see chapter 1). This effective source size can be more than one order of magnitude smaller than the geometric source size not only in dc [11] operation, but also for laser-triggered emission [11, 12].

We routinely operated diamond-coated tungsten tips in dc field emission. Depending on the individual sample, the field emission threshold was found between 200-2000 V. Compared to bare tungsten emitter with the same size, the emission threshold was lower. However, DC emission was not the focus of this work and our statistics don't allow a more precise and quantitative statement.

Similarly to Schottky emitters, cold field emitters suffer from current degradation over time when used in femtosecond laser-triggered operation. The maximum peak brightness is estimated ”in the 10^{13} A m^{-2} sr^{-1}” range at 15 electrons per pulse [15].

Chapter 3

Photoelectron emission from metallic surfaces

The electron pulses studied in this work were generated via photoemission using femtosecond laser pulses of various wavelengths and intensities. This chapter describes the essential theory of photoelectron emission needed for the scope of this work. For the sake of simplicity and readability, this chapter focuses on photoemission from metal surfaces. The special case of electron emission from diamond-coated metal surfaces will be described in chapter 4.4.2 as it requires knowledge of the band structure, the surface termination and morphology of the diamond samples.

3.1 Classical Photoemission

The photoelectric effect, i.e. the observation that illumination of ultraviolet light on metals can induce a current, was observed in 1887 by Heinrich Hertz and Wilhelm Hallwachs. This could be attributed to an increase of free electrons after the discovery of the electron by Thomson in 1897. Surprisingly, the photoelectric effect seemed to be instantaneous and depended on the wavelength of the light. This observation could not be explained by the common theory, that light is a wave. Albert Einstein received the Nobel Prize in Physics 1921 for solving this puzzle. He introduced the concept of quantized light with energy $E_{ph} = \hbar\omega$ - nowadays called photons - in 1905 [49]. This concept explained the photoelectric effect of metals: Electrons absorb one photon, the remaining energy is converted to kinetic energy of the electrons.

$$E_{kin} = E_{ph} - \Phi = \hbar\omega - \Phi \tag{3.1}$$

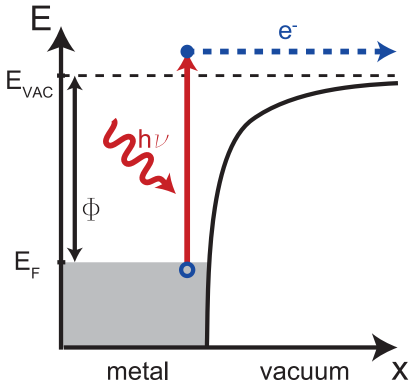

Figure 3.1: Sketch of the classical photoelectric effect in a metal. An electron absorbs one photon and is emitted into vacuum if the photon energy is larger than the work function. Taken from [50].

If the photon energy is smaller than the material's work function, the photocurrent drops dramatically. Measuring this drop enabled measurements of the material's work function. As the light field is shielded by free carriers inside the metal and the carriers typically thermalize within femto- to picoseconds, only carriers within a few atomic layers from a vacuum interface are effectively emitted. In publication 5.2, we also observe that this kind of photoemission is the dominant mechanism when using ultraviolet pulses with wavelength 235-260 nm. However, at high intensities as well as with longer wavelengths, we observed nonlinear photoemission.

3.2 Nonlinear Photoemission

In general, bound electrons inside solids can absorb more than one photon. Compared with the process of absorbing a single photon, the probability of absorbing several photons is in general lower as this involves additional steps. The photon densities, i.e. light intensities, needed to observe multi-photon photoemission were not accessible until the invention of the optical laser in 1960. Only one year later, two-photon photoemission was observed from CaF_2Eu^{2+} [51], where the photon energy was not sufficient for a single photon emission process. In 1965, Keldysh formulated a more general theory for photoemission which accommodates single-photon, multi-photon and tunneling emission [52] (see. Fig. 3.2). As all experimental parameters in the publications of this thesis were chosen to result in single- or multi-photon emission, we focus on these cases rather than covering a theory valid for all intensities, wavelengths and work functions.

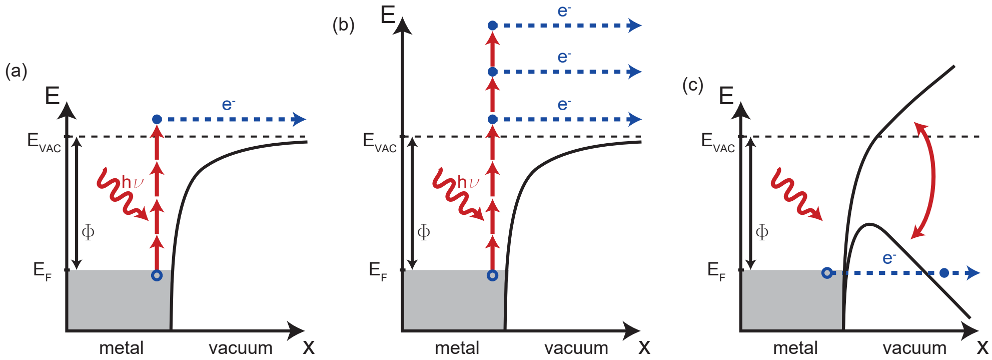

Figure 3.2: (a) Multiphoton electron emission. More than one photon is absorbed to overcome the barrier height. (b) Above-threshold emission. More photons than necessary are absorbed by one electron. (c) Light-induced tunneling. The light field is so large, that the potential at the surface oscillates strongly and electrons can tunnel into vacuum. Taken from [50].

In the perturbative regime, i.e. the electric field inside the matter is much larger than the laser field, the multiphoton electron emission process can be pictured as the simultaneous absorption of several photons. In this case the final probability is the product of the single absorptions. The probability of a single absorption is proportional to the laser intensity I, which is a measure for the photon density. The total emission current J is then given by the sum of all possible emission paths including absorbing more photons than needed to overcome the barrier height:

$$J = \sum_{n}^{\infty} J_n = \sum_{n}^{\infty} a_n \cdot I^n \tag{3.2}$$

where a is the prefactor and n is the number of absorbed photons. At low intensities, it is often sufficient to reduce eq. 3.2 to the lowest photon order n that fulfills $n \cdot E_{ph} > \Phi$ as this contribution is typically dominant.

$$J \approx a_n \cdot I^n \tag{3.3}$$

However, with increasing intensity, the higher order contributions become more relevant. I.e. some electrons absorb more photons than needed to overcome the potential barrier. This above-threshold-ionisation is illustrated in Fig. 3.2(b) and has been observed in the photoelectron spectra of solids [53, 54, 55] and gases [56]. Applying even stronger fields bends the atomic potential so strongly that electrons can tunnel into vacuum (see Fig. 3.2 c)).

In this scenario, the photon picture breaks down and the light fields can be pictured classically. These effects play a key role in the process of high harmonic generation for the generation of attosecond ultraviolet pulse trains [57].

As we conducted our experiments in the perturbative regime and never observed light-induced tunneling, we stay in the photon picture for the interpretation of our data. In this regime, eq. 3.3 can be used to identify the dominant emission channel in the investigated laser intensity window. Plotting eq. 3.3 double-logarithmically allows to directly extract n from the slope of the measurement data.

$$\log(J) = n \cdot \log(a_n \cdot I) \tag{3.4}$$

If the slope is integer, this can be interpreted as only one photoemission channel with photon order n contributing. Noninteger slopes are called effective nonlinearity and indicate multiple channels contributing. In publication 5.2, we use this technique to identify different emission channels of femtosecond laser-induced electron emission from diamond-coated tungsten tips.

Chapter 4

Diamond

4.1 Properties and applications

Diamond is a material with exceptional properties. Consisting of only one chemical element - carbon - diamond exhibits the highest hardness and the lowest compressibility of all naturally occurring materials. It is chemically inert to most acids, bases and solvents and has a high electric breakdown field. Despite being an electrical insulator, it also exhibits the highest thermal conductivity at room temperature of all naturally occurring materials. Due to these properties, diamond has a wide range of applications. The most well known use in society is gem stones. The comparably high refractive index and dispersion in the visible range give diamond gem stones their particularly nice look. One of the most common use of synthetic diamond is polishing and cutting due to its hardness. The high breakdown field and the high thermal conductivity make diamond a highly promising candidate for next generation high power electrical devices, even though major challenges need to be overcome: Despite decade long research, wafer scale production of single crystal diamond with low defect density remains the holy grail of diamond crystal growth. Additionally, only dopants with donor/acceptor levels above k_BT with activation energy of more than ten times the thermal energy at room temperature are available. The most important dopants are boron (0.35 eV), phosphorous (0.57 eV) and nitrogen (1.7 eV) [58].
From a solid state physics perspective, diamond is a wide band gap semiconductor with face centered cubic crystal structure with an indirect band gap of 5.5 eV [59] and a direct bandgap of 7.1 eV [60, 61]. The band gap is one of the key parameters in the absorption process of photons as it defines the minimum photoexcitation energy of the (ideal) semiconductor. However, it is the electron affinity (EA), which provides diamond with its exceptional

photoelectron emission properties, therefore we will briefly introduce it in the next section.

4.2 Electron affinity

In solid state physics, the EA χ is defined as the energy that is released, when an electron right in front of the solid's surface is moved to the conduction band minimum (CBM) inside the semiconductor. In other words, it is the energy difference between the vacuum level E_{vac} and the CBM.

$$\chi = E_{vac} - E_{CBM} \tag{4.1}$$

While the CBM at the surface is defined by the crystal structure and potential band bending, the EA is a surface property, which depends also on the chemical elements and associated dipole moment at the interface. As the work function Φ is defined as the difference between E_{vac} and E_F, Φ directly depends on χ

$$\Phi = E_{vac} - E_F = E_{CBM} - E_F + \chi \tag{4.2}$$

For most solids and their thermodynamically stable surfaces, the EA is positive. Only very few surfaces with negative electron affinity (NEA) exist. Diamond is one of these rare materials which can exhibit true NEA. While the EA is positive for a clean carbon surface and oxidized surfaces, hydrogen terminated surfaces exhibit NEA (see Fig. 4.1). It is the large dipole moment and the corresponding potential drop across the C-H bond which yields the NEA. Using only hydrogen and oxygen for surface termination, the EA is readily adjustable between +1.7 eV and -1.3 eV [62].
As we will show in chap. 4.4.2, NEA has a dramatic effect on the photoelectron emission properties.

4.3 Nanocrystalline diamond

All established techniques for the deposition of artificial diamond - chemical vapour deposition (CVD) as well as high pressure high temperature conversion from graphite - are comparatively expensive. To reduce costs and still make use of the properties of diamonds, there is a high demand for diamond coatings, e.g. as tribological coatings. To achieve thin films, the nucleation/seeding density needs to be high. The smaller the distance between seeds, the quicker the single grains grow into a dense film, i.e. the minimum achievable thickness is inversely proportional to the square root of

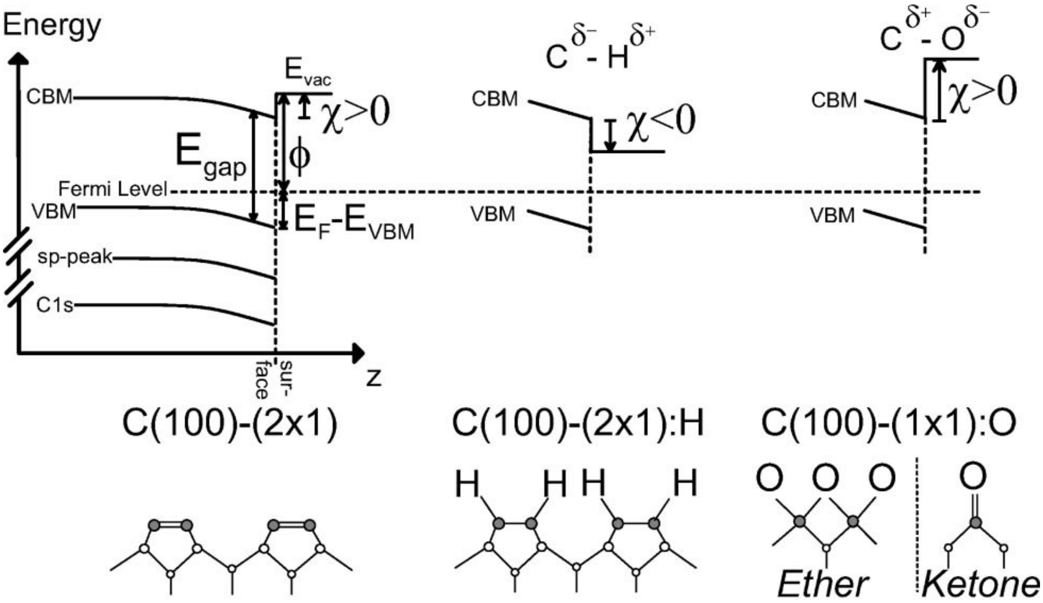

Figure 4.1: Electron affinity of different diamond surfaces. Depending on the surface termination, EA is positive (natural surface and oxygen terminated) or negative (hydrogen terminated). Taken from [62].

the seed density. Established methods for high nucleation/seeding density include mechanical scratching, bias enhanced nucleation and seeding with nanodiamond particles [63]. In our work, we achieved high seed densities by dip-seeding in nanodiamond suspension and adjusting the electrostatic force between seeds and substrate surface. We chose seeds with positive zeta potential as our substrate samples were oxidized and therefore exhibit negative zeta potential (see publication 5.1).

With subsequent CVD, this approach makes conformal coating of 3-dimensional substrates possible, even with sub-100 nm film thickness. During growth of the diamond grains, the atoms at the grain surface have fewer binding partners and therefore the chemical bonds show sp^2 character. This bond character remains at the grain boundaries even after the grains have grown together and formed a film. In publication 5.3, we could measure the relative sp^2 to sp^3 ratio with nanometer resolution and visualize the graphitic sp^2 paths along grain boundaries via scanning transmission electron microscopy in combination with electron energy loss spectroscopy. These paths provide electrical conductivity and also play a role in photoelectron emission as we show in publication 5.2. For more details on nanocrystalline diamond, the reader is referred to [64]. In the following section, we briefly review the properties of diamond as both cold field and photoelectron emitter.

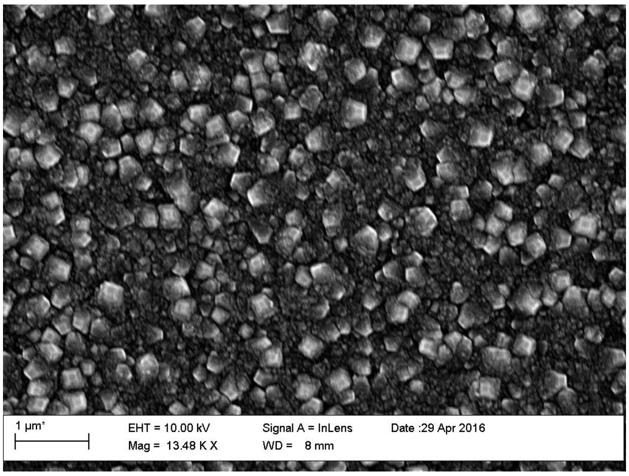

Figure 4.2: Scanning electron micrograph of nanocrystalline diamond. High seeding density allows deposition of sub-micrometer thin closed films. The interface between grains is graphitic, therefore conductive paths exist across the film. In publication 5.1, we developed a method for visualizing the sp^2 character of the grain boundaries. This character also plays an important role in the photoemission model in publication 5.2.

4.4 Diamond as an electron emitter

4.4.1 Cold field emission

Driven by the development of field emission flat panels [65], cold field emission from nanocrystalline diamond (NCD) was investigated in the 1990s [66, 67]. Diamond was a promising candidate due to the materials unique properties and the adjustability of both electrical conductivity and work function via doping and surface termination. The low work function - especially of n-doped and hydrogen-terminated diamond with NEA - and the microstructure of NCD results in low turn-on fields of flat surfaces below 1 V/μm [68]. This allows to work with low voltages which is advantageous for the electronic design of the circuit boards for flat panels. The main disadvantage of NCD surfaces is the heterogeneity of the emitted current density. This is a consequence of both the geometry, the resulting local electrostatic fields and the local work function of the coating (see Fig. 4.3). At the triple junction between vacuum, diamond and the graphitic grain boundaries, the electrons which originate from the conductive boundaries effectively feel the work function of the NEA diamond.

While dc emission from needle-shaped diamond emitters has been researched decades ago [69, 70, 71], the field of photoemission from such emitters re-

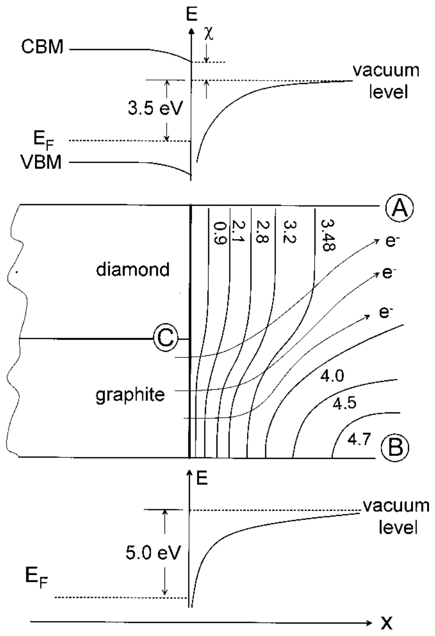

Figure 4.3: Band diagram of the diamond/vacuum junction (top), graphite/vacuum junction and the triple junction (center) with equipotential lines. Even though the electrons originate from graphite, they may effectively "see" the diamond work function if they are close to the triple junction of graphite, diamond and vacuum. Taken from [72].

mained to be discovered.

4.4.2 Photoemission

The combination of NEA and indirect band gap results in unique photoemission properties. The photoemission process can be divided into photoexcitation, thermalization, migration to the surface and transfer to vacuum. Quickly after the photoexcitation of electron-hole pairs across the band gap of diamond, the charge carriers thermalize via electron-electron and electron-phonon scattering. The length scale for this thermalization process is on the order of the inelastic scattering length, *i.e.* a few nanometers [73]. As diamond is an indirect band gap semiconductor, excitation and recombination require the absorption or creation of a phonon. This additional process and the high optical phonon energy (141 meV for the transverse optical phonon) reduce the recombination probability, which leads to a comparably long carrier lifetime up to microseconds [73]. Within this lifetime, the electrons can pass a distance on the order of the diffusion length inside the material, *i.e.* tens of micrometers. As the vacuum level lies below the CBM, electrons in the conduction band can be emitted into vacuum once they reach the surface. In other words, carriers can be excited deeply below the surface, migrate to the surface and be emitted into vacuum. This results in a photoyield, which is orders of magnitude larger compared to positive electron affinity (PEA) diamond, metals and semiconductors, where only electrons excited within in the short thermalization length can escape into vacuum [74, 75, 76].

The unique photoemission behaviour in combination with the materials robustness makes diamond a promising candidate for a stable high brightness photocathode. However, only single-photon photoemission with nanosecond pulses has been investigated [77]. After the submission of publication 5.2, one study on multiphoton emission from - single crystalline - diamond was published with signs of above-threshold photoemission [78].

Our work in publication 5.2 is the first work on femtosecond multiphoton emission from NCD and from a tip-shaped metal semiconductor heterostructure. We show that the physics of photoexcitation and -emission with femtosecond laser pulses is complex. Depending on the exact laser wavelength and intensity, different emission channels dominate. These channels are identified by the number of photons needed to photoemit one electron at a particular wavelength. For example, excitation across the direct band gap dominates at 512 nm excitation wavelength, whereas direct emission into vacuum dominates at 1932 nm. Based on the band alignment of the relevant junctions, we proposed an emission model, which explains the experimental data. We also show that the photoemission is stable from the UV (235 nm) to the infrared (1932 nm) at all bunch charges and repetition rates investigated.

The stable photoelectron current and the high brightness of the emitted electrons are encouraging to further investigate diamond-coated tungsten needle tips as an ultrafast electron source. Measuring the electron bunch duration is particularly interesting. Direct emission into vacuum is expected to be fast, whereas the consecutive absorption, migration and emission is expected to be slower.

Bibliography

[1] D.-S. Yang, O. F. Mohammed, and A. H. Zewail, "Scanning ultrafast electron microscopy," *Proceedings of the National Academy of Sciences*, vol. 107, no. 34, pp. 14993–14998, 2010.

[2] K. B. Schliep, P. Quarterman, J.-P. Wang, and D. J. Flannigan, "Picosecond fresnel transmission electron microscopy," *Applied Physics Letters*, vol. 110, no. 22, p. 222404, 2017.

[3] N. R. da Silva, M. Möller, A. Feist, H. Ulrichs, C. Ropers, and S. Schäfer, "Nanoscale mapping of ultrafast magnetization dynamics with femtosecond lorentz microscopy," *Physical Review X*, vol. 8, no. 3, p. 031052, 2018.

[4] G. Berruto, I. Madan, Y. Murooka, G. Vanacore, E. Pomarico, J. Rajeswari, R. Lamb, P. Huang, A. Kruchkov, Y. Togawa, T. LaGrange, D. McGrouther, H. Rønnow, and F. Carbone, "Laser-induced skyrmion writing and erasing in an ultrafast cryo-lorentz transmission electron microscope," *Physical Review Letters*, vol. 120, no. 11, p. 117201, 2018.

[5] B. J. Siwick, J. R. Dwyer, R. E. Jordan, and R. J. D. Miller, "An atomic-level view of melting using femtosecond electron diffraction," *Science*, vol. 302, no. 5649, pp. 1382–1385, 2003.

[6] P. Baum, D.-S. Yang, and A. H. Zewail, "4d visualization of transitional structures in phase transformations by electron diffraction," *Science*, vol. 318, no. 5851, pp. 788–792, 2007.

[7] G. Sciaini and R. J. D. Miller, "Femtosecond electron diffraction: heralding the era of atomically resolved dynamics," *Reports on Progress in Physics*, vol. 74, no. 9, p. 096101, 2011.

[8] Y. Morimoto and P. Baum, "Diffraction and microscopy with attosecond electron pulse trains," *Nature Physics*, vol. 14, no. 3, pp. 252–256, 2018.

[9] S. Ackermann, A. Azima, S. Bajt, J. Bödewadt, F. Curbis, H. Dachraoui, H. Delsim-Hashemi, M. Drescher, S. Düsterer, B. Faatz, M. Felber, J. Feldhaus, E. Hass, U. Hipp, K. Honkavaara, R. Ischebeck, S. Khan, T. Laarmann, C. Lechner, T. Maltezopoulos, V. Miltchev, M. Mittenzwey, M. Rehders, J. Rönsch-Schulenburg, J. Rossbach, H. Schlarb, S. Schreiber, L. Schroedter, M. Schulz, S. Schulz, R. Tarkeshian, M. Tischer, V. Wacker, and M. Wieland, "Generation of coherent 19- and 38-nm radiation at a free-electron laser directly seeded at 38 nm," *Physical Review Letters*, vol. 111, no. 11, p. 114801, 2013.

[10] J. B. Rosenzweig, *Fundamentals of Beam Physics.* Oxford University Press, 2003.

[11] D. Ehberger, J. Hammer, M. Eisele, M. Krüger, J. Noe, A. Högele, and P. Hommelhoff, "Highly coherent electron beam from a laser-triggered tungsten needle tip," *Phys. Rev. Lett.*, vol. 114, no. 22, p. 227601, 2015.

[12] S. Meier, T. Higuchi, M. Nutz, A. Högele, and P. Hommelhoff, "High spatial coherence in multiphoton-photoemitted electron beams," *Applied Physics Letters*, vol. 113, no. 14, p. 143101, 2018.

[13] B. Cho, T. Ichimura, R. Shimizu, and C. Oshima, "Quantitative evaluation of spatial coherence of the electron beam from low temperature field emitters," *Physical Review Letters*, vol. 92, p. 246103, jun 2004.

[14] A. Feist, N. Bach, N. R. da Silva, T. Danz, M. Möller, K. E. Priebe, T. Domröse, J. G. Gatzmann, S. Rost, J. Schauss, S. Strauch, R. Bormann, M. Sivis, S. Schäfer, and C. Ropers, "Ultrafast transmission electron microscopy using a laser-driven field emitter: Femtosecond resolution with a high coherence electron beam," *Ultramicroscopy*, vol. 176, pp. 63–73, 2017.

[15] F. Houdellier, G. Caruso, S. Weber, M. Kociak, and A. Arbouet, "Development of a high brightness ultrafast transmission electron microscope based on a laser-driven cold field emission source," *Ultramicroscopy*, vol. 186, pp. 128–138, 2018.

[16] C. Kealhofer, *Nanometer tip-based ultrafast electron sources: emission processes and direct pulse characterization techniques.* PhD thesis, Stanford University, 2013.

[17] M. Reiser, *Theory and Design of Charged Particle Beams.* Wiley, 2008.

[18] achip.fau.de and achip.stanford.edu.

[19] R. J. England, R. J. Noble, K. Bane, D. H. Dowell, C.-K. Ng, J. E. Spencer, S. Tantawi, Z. Wu, R. L. Byer, E. Peralta, K. Soong, C.-M. Chang, B. Montazeri, S. J. Wolf, B. Cowan, J. Dawson, W. Gai, P. Hommelhoff, Y.-C. Huang, C. Jing, C. McGuinness, R. B. Palmer, B. Naranjo, J. Rosenzweig, G. Travish, A. Mizrahi, L. Schachter, C. Sears, G. R. Werner, and R. B. Yoder, "Dielectric laser accelerators," *Reviews of Modern Physics*, vol. 86, no. 4, pp. 1337–1389, 2014.

[20] K. Soong, R. L. Byer, E. R. Colby, R. J. England, and E. A. Peralta, "Laser damage threshold measurements of optical materials for direct laser accelerators," *AIP Conference Proceedings*, vol. 1507, p. 511, 2013.

[21] E. A. Peralta, K. Soong, R. J. England, E. R. Colby, Z. Wu, B. Montazeri, C. McGuinness, J. McNeur, K. J. Leedle, D. Walz, and et al., "Demonstration of electron acceleration in a laser-driven dielectric microstructure," *Nature*, vol. 503, no. 7474, p. 91Â–94, 2013.

[22] J. Breuer and P. Hommelhoff, "Laser-based acceleration of nonrelativistic electrons at a dielectric structure," *Physical Review Letters*, vol. 111, no. 13, p. 134803, 2013.

[23] K. J. Leedle, A. Ceballos, H. Deng, O. Solgaard, R. F. Pease, R. L. Byer, and J. S. Harris, "Dielectric laser acceleration of sub-100 keV electrons with silicon dual-pillar grating structures," *Optics Letters*, vol. 40, no. 18, p. 4344, 2015.

[24] K. J. Leedle, R. F. Pease, R. L. Byer, and J. S. Harris, "Laser acceleration and deflection of 963 keV electrons with a silicon dielectric structure," *Optica*, vol. 2, no. 2, p. 158, 2015.

[25] J. McNeur, M. Kozák, N. Schönenberger, K. J. Leedle, H. Deng, A. Ceballos, H. Hoogland, A. Ruehl, I. Hartl, R. Holzwarth, O. Solgaard, J. S. Harris, R. L. Byer, and P. Hommelhoff, "Elements of a dielectric laser accelerator," *Optica*, vol. 5, no. 6, p. 687, 2018.

[26] P. Yousefi, N. Schönenberger, J. Mcneur, M. Kozák, U. Niedermayer, and P. Hommelhoff, "Dielectric laser electron acceleration in a dual pillar grating with a distributed bragg reflector," *Optics Letters*, vol. 44, no. 6, p. 1520, 2019.

[27] K. J. Leedle, D. S. Black, Y. Miao, K. E. Urbanek, A. Ceballos, H. Deng, J. S. Harris, O. Solgaard, and R. L. Byer, "Phase-dependent laser acceleration of electrons with symmetrically driven silicon dual pillar gratings," *Optics Letters*, vol. 43, no. 9, p. 2181, 2018.

[28] N. Schönenberger, A. Mittelbach, P. Yousefi, J. McNeur, U. Niedermayer, and P. Hommelhoff, “Generation and characterization of attosecond microbunched electron pulse trains via dielectric laser acceleration,” *Physical Review Letters*, vol. 123, no. 26, p. 264803, 2019.

[29] D. Cesar, S. Custodio, J. Maxson, P. Musumeci, X. Shen, E. Threlkeld, R. J. England, A. Hanuka, I. V. Makasyuk, E. A. Peralta, K. P. Wootton, and Z. Wu, “High-field nonlinear optical response and phase control in a dielectric laser accelerator,” *Communications Physics*, vol. 1, p. 46, Aug. 2018.

[30] U. Niedermayer, T. Egenolf, O. Boine-Frankenheim, and P. Hommelhoff, “Alternating-phase focusing for dielectric-laser acceleration,” *Physical Review Letters*, vol. 121, no. 21, p. 214801, 2018.

[31] K. Wootton, R. Assmann, D. Black, R. Byer, B. Cowan, H. Deng, T. Egenolf, R. England, S. Fan, J. Harris, I. Hartl, P. Hommelhoff, T. Hughes, J. Illmer, R. Ischebeck, F. Kaertner, W. Kuropka, Y. J. Lee, A. Li, F. Mayet, J. McNeur, A. Mittelbach, P. Musumeci, U. Niedermayer, M. Qi, L. Rivkin, A. Rühl, N. Sapra, N. Schoenenberger, O. Solgaard, A. Tafel, S. Tantawi, and J. Vuckovic, “Towards a fully integrated accelerator on a chip: Dielectric laser acceleration (dla) from the source to relativistic electrons,” *Proceedings of the 8th Int. Particle Accelerator Conf.*, vol. IPAC2017, pp. 2520–2525, 2017.

[32] G. Aad, T. Abajyan, B. Abbott, J. Abdallah, S. Abdel Khalek, A. Abdelalim, O. Abdinov, R. Aben, B. Abi, M. Abolins, and et al., “Observation of a new particle in the search for the standard model higgs boson with the atlas detector at the LHC,” *Phys. Lett. B*, vol. 716, no. 1, pp. 1–29, 2012.

[33] S. Chatrchyan, V. Khachatryan, A. Sirunyan, A. Tumasyan, W. Adam, E. Aguilo, T. Bergauer, M. Dragicevic, J. Er, C. Fabjan, and et al., “Observation of a new boson at a mass of 125 GeV with the CMS experiment at the LHC,” *Phys. Lett. B*, vol. 716, no. 1, pp. 30–61, 2012.

[34] W. J. Engelen, M. A. van der Heijden, D. J. Bakker, E. J. D. Vredenbregt, and O. J. Luiten, “High-coherence electron bunches produced by femtosecond photoionization,” *Nature Communications*, vol. 4, no. 1, p. 1693, 2013.

[35] O. Richardson, “LI. some applications of the electron theory of matter,” *The London, Edinburgh, and Dublin Philosophical Magazine and Journal of Science*, vol. 23, no. 136, pp. 594–627, 1912.

[36] J. Pelletier and C. Pomot, “Work function of sintered lanthanum hexaboride,” *Applied Physics Letters*, vol. 34, no. 4, pp. 249–251, 1979.

[37] D. A. Plemmons, P. K. Suri, and D. J. Flannigan, “Probing structural and electronic dynamics with ultrafast electron microscopy,” *Chemistry of Materials*, vol. 27, no. 9, pp. 3178–3192, 2015.

[38] J. B. Cui, J. Ristein, and L. Ley, “Dehydrogenation and the surface phase transition on diamond (111): Kinetics and electronic structure,” *Physical Review B*, vol. 59, no. 8, pp. 5847–5856, 1999.

[39] J. Chen, S. Z. Deng, J. Chen, Z. X. Yu, and N. S. Xu, “Graphitization of nanodiamond powder annealed in argon ambient,” *Applied Physics Letters*, vol. 74, no. 24, pp. 3651–3653, 1999.

[40] G. A. Schwind, G. Magera, and L. W. Swanson, “Comparison of parameters for schottky and cold field emission sources,” *Journal of Vacuum Science & Technology B: Microelectronics and Nanometer Structures*, vol. 24, no. 6, p. 2897, 2006.

[41] M. Fransen, M. Overwijk, and P. Kruit, “Brightness measurements of a ZrO/w schottky electron emitter in a transmission electron microscope,” *Applied Surface Science*, vol. 146, no. 1-4, pp. 357–362, 1999.

[42] A. H. V. van Veen, C. W. Hagen, J. E. Barth, and P. Kruit, “Reduced brightness of the ZrO/w schottky electron emitter,” *Journal of Vacuum Science & Technology B: Microelectronics and Nanometer Structures*, vol. 19, no. 6, p. 2038, 2001.

[43] J. Sun, V. A. Melnikov, J. I. Khan, and O. F. Mohammed, “Real-space imaging of carrier dynamics of materials surfaces by second-generation four-dimensional scanning ultrafast electron microscopy,” *The Journal of Physical Chemistry Letters*, vol. 6, no. 19, pp. 3884–3890, 2015.

[44] M. S. Bronsgeest, *Physics of Schottky Electron Sources.* PhD thesis, Delft University, 2009.

[45] R. Fowler and L. Nordheim, “Electron emission in intense electric fields,” *Proceedings of the Royal Society of London. Series A, Containing Papers of a Mathematical and Physical Character*, vol. 119, no. 781, pp. 173–181, 1928.

[46] E. L. Murphy and R. H. Good, “Thermionic emission, field emission, and the transition region,” *Physical Review*, vol. 102, no. 6, pp. 1464–1473, 1956.

[47] R. G. Forbes, “Physics of generalized fowler-nordheim-type equations,” *Journal of Vacuum Science & Technology B: Microelectronics and Nanometer Structures*, vol. 26, no. 2, p. 788, 2008.

[48] L. Swanson and G. Schwind, “Chapter 2 a review of the cold-field electron cathode,” in *Advances in Imaging and Electron Physics*, pp. 63–100, Elsevier, 2009.

[49] A. Einstein, “über einen die erzeugung und verwandlung des lichtes betreffenden heuristischen gesichtspunkt,” *Annalen der Physik*, vol. 322, pp. 132–148, 1905.

[50] M. Förster, *Investigation and control of strong-field photoemission from metal nanotips.* PhD thesis, Ludwig-Maximilians-Universität Münche, 2016.

[51] W. Kaiser and C. G. B. Garrett, “Two-photon excitation in CaF2:eu2,” *Physical Review Letters*, vol. 7, no. 6, pp. 229–231, 1961.

[52] L. Keldysh *et al.*, “Ionization in the field of a strong electromagnetic wave,” *Sov. Phys. JETP*, vol. 20, no. 5, pp. 1307–1314, 1965.

[53] S. Luan, R. Hippler, H. Schwier, and H. Lutz, “Electron emission from polycrystalline copper surfaces by multi-photon absorption,” *EPL (Europhysics Letters)*, vol. 9, no. 5, p. 489, 1989.

[54] M. Krüger, M. Schenk, and P. Hommelhoff, “Attosecond control of electrons emitted from a nanoscale metal tip,” *Nature*, vol. 475, no. 7354, pp. 78–81, 2011.

[55] M. Förster, T. Paschen, M. Krüger, C. Lemell, G. Wachter, F. Libisch, T. Madlener, J. Burgdörfer, and P. Hommelhoff, “Two-color coherent control of femtosecond above-threshold photoemission from a tungsten nanotip,” *Physical Review Letters*, vol. 117, no. 21, p. 217601, 2016.

[56] P. Agostini, F. Fabre, G. Mainfray, G. Petite, and N. K. Rahman, “Free-free transitions following six-photon ionization of xenon atoms,” *Physical Review Letters*, vol. 42, no. 17, pp. 1127–1130, 1979.

[57] F. Frank, C. Arrell, T. Witting, W. A. Okell, J. McKenna, J. S. Robinson, C. A. Haworth, D. Austin, H. Teng, I. A. Walmsley, J. P. Marangos, and J. W. G. Tisch, “Invited review article: Technology for attosecond science,” *Review of Scientific Instruments*, vol. 83, no. 7, p. 071101, 2012.

[58] C. J. Wort and R. S. Balmer, “Diamond as an electronic material,” *Materials Today*, vol. 11, no. 1-2, pp. 22–28, 2008.

[59] P. Dean, E. Lightowlers, and D. Wight, “Intrinsic and extrinsic recombination radiation from natural and synthetic aluminum-doped diamond,” *Physical review*, vol. 140, p. 352, 1965.

[60] S. Logothetidis, J. Petalas, H. M. Polatoglou, and D. Fuchs, “Origin and temperature dependence of the first direct gap of diamond,” *Physical Review B*, vol. 46, no. 8, pp. 4483–4494, 1992.

[61] F. Giustino, S. G. Louie, and M. L. Cohen, “Electron-phonon renormalization of the direct band gap of diamond,” *Physical Review Letters*, vol. 105, no. 26, p. 265501, 2010.

[62] F. Maier, J. Ristein, and L. Ley, “Electron affinity of plasma-hydrogenated and chemically oxidized diamond (100) surfaces,” *Phys. Rev. B*, vol. 64, no. 16, p. 165411, 2001.

[63] J. C. Arnault and H. A. Girard, “CHAPTER 10. diamond nucleation and seeding techniques: Two complementary strategies for the growth of ultra-thin diamond films,” in *Nanodiamond*, pp. 221–252, Royal Society of Chemistry, 2014.

[64] J. E. Butler and A. V. Sumant, “The CVD of nanodiamond materials,” *Chemical Vapor Deposition*, vol. 14, no. 7-8, pp. 145–160, 2008.

[65] A. Talin, K. Dean, and J. Jaskie, “Field emission displays: a critical review,” *Solid-State Electronics*, vol. 45, no. 6, pp. 963–976, 2001.

[66] C. Wang, A. Garcia, D. Ingram, M. Lake, and M. Kordesch, “Cold field emission from CVD diamond films observed in emission electron microscopy,” *Electronics Letters*, vol. 27, no. 16, p. 1459, 1991.

[67] K. Okano, K. Hoshina, M. Iida, S. Koizumi, and T. Inuzuka, “Fabrication of a diamond field emitter array,” *Applied Physics Letters*, vol. 64, no. 20, pp. 2742–2744, 1994.

[68] M. W. Geis, J. C. Twichell, N. N. Efremow, K. Krohn, and T. M. Lyszczarz, “Comparison of electric field emission from nitrogen-doped, type ib diamond, and boron-doped diamond,” *Applied Physics Letters*, vol. 68, no. 16, pp. 2294–2296, 1996.

[69] J. Liu, V. V. Zhirnov, G. J. Wojak, A. F. Myers, W. B. Choi, J. J. Hren, S. D. Wolter, M. T. McClure, B. R. Stoner, and J. T. Glass, "Electron emission from diamond coated silicon field emitters," *Appl. Phys. Lett.*, vol. 65, no. 22, pp. 2842–2844, 1994.

[70] W. B. Choi, J. J. Cuomo, V. V. Zhirnov, A. F. Myers, and J. J. Hren, "Field emission from silicon and molybdenum tips coated with diamond powder by dielectrophoresis," *Appl. Phys. Lett.*, vol. 68, no. 5, pp. 720–722, 1996.

[71] M. Q. Ding, "Field emission from amorphous diamond coated mo tip emitters by pulsed laser deposition," *Journal of Vacuum Science & Technology B: Microelectronics and Nanometer Structures*, vol. 15, no. 4, p. 840, 1997.

[72] J. B. Cui, M. Stammler, J. Ristein, and L. Ley, "Role of hydrogen on field emission from chemical vapor deposited diamond and nanocrystalline diamond powder," *J. Appl. Phys.*, vol. 88, no. 6, pp. 3667–3673, 2000.

[73] J. Ristein, W. Stein, and L. Ley, "Defect spectroscopy and determination of the electron diffusion length in single crystal diamond by total photoelectron yield spectroscopy," *Physical Review Letters*, vol. 78, no. 9, pp. 1803–1806, 1997.

[74] F. Himpsel, J. Knapp, J. VanVechten, and D. Eastman, "Quantum photoyield of diamond (111)Â—a stable negative-affinity emitter," *Physical Review B*, vol. 20, no. 2, p. 624, 1979.

[75] J. B. Cui, J. Ristein, and L. Ley, "Low-threshold electron emission from diamond," *Physical Review B*, vol. 60, no. 23, pp. 16135–16142, 1999.

[76] J. Cui, J. Ristein, M. Stammler, K. Janischowsky, G. Kleber, and L. Ley, "Hydrogen termination and electron emission from CVD diamond surfaces: a combined secondary electron emission, photoelectron emission microscopy, photoelectron yield, and field emission study," *Diamond Relat. Mater.*, vol. 9, no. 3-6, pp. 1143–1147, 2000.

[77] A. N. Obraztsov, P. G. Kopylov, A. L. Chuvilin, and N. V. Savenko, "Production of single crystal diamond needles by a combination of CVD growth and thermal oxidation," *Diamond and Related Materials*, vol. 18, no. 10, pp. 1289–1293, 2009.

[78] M. Borz, M. H. Mammez, I. Blum, J. Houard, G. D. Costa, F. Delaroche, S. Idlahcen, A. Haboucha, A. Hideur, V. I. Kleshch, A. N.

Obraztsov, and A. Vella, “Photoassisted and multiphoton emission from single-crystal diamond needles,” *Nanoscale*, vol. 11, no. 14, pp. 6852–6858, 2019.

Chapter 5

Publications

The following publications are displayed in their original form with permission of the respective journals. These publications represent the main work of this thesis.
At the beginning of each publication, the author's contributions are stated, which have been acknowledged and signed by all co-authors.

Author contribution for publication

"Fabrication and structural characterization of diamond-coated tungsten tips"

Authors: A.Tafel, M. Wu, E. Spiecker, P. Hommelhoff, J. Ristein

Diamond and related materials 97, 107446, **2019**

Co-Authors contributions:

- Support in writing of the manuscript
- Preparation for TEM measurements
- Conducting TEM measurements
- Discussion of methods and results
- Analyzing the results

A.Tafels contribution:

- Writing of the manuscript
- Participating during TEM measurements
- Discussion of methods and results
- Analyzing the results
- Etching of tungsten needle tips
- Development of recipe for selective seeding and diamond deposition
- Sample fabrication for TEM measurements

Diamond & Related Materials 97 (2019) 107446

Contents lists available at ScienceDirect

Diamond & Related Materials

journal homepage: www.elsevier.com/locate/diamond

Fabrication and structural characterization of diamond-coated tungsten tips

Alexander Tafel[a,*], Mingjian Wu[b], Erdmann Spiecker[b], Peter Hommelhoff[a], Jürgen Ristein[a]

[a] *Department of Physics, Friedrich-Alexander-Universität Erlangen-Nürnberg, Staudtstrasse 1, Erlangen D-91058, Germany*
[b] *Institute of Micro- and Nanostructure Research & Center for Nanoanalysis and Electron Microscopy (CENEM), Department of Materials Science, Friedrich-Alexander-Universität Erlangen-Nürnberg, Cauerstrasse 6, Erlangen D-91058, Germany*

ARTICLE INFO

Keywords:
Conformal coating
Nanocrystalline diamond
EELS
HRTEM
Nanoemitter

ABSTRACT

Coating metal nanotips with a negative electron affinity material like hydrogen-terminated diamond bears promise for a high brightness photocathode. We report a recipe on the fabrication of diamond-coated tungsten tips. A tungsten wire is etched electrochemically to a nanometer sharp tip, dip-seeded in diamond suspension and subsequently overgrown with a diamond film by plasma-enhanced chemical vapor deposition. With dip-seeding only, the seeding density declines towards the tip apex due to seed migration during solvent evaporation. The migration of seeds can be counteracted by nitrogen gas flow towards the apex, which makes coating of the apex with nanometer-thin diamond possible. At moderate gas flow, diamond grows homogeneously at shaft and apex whereas at high flow diamond grows in the apex region only. With this technique, we achieve a thickness of a few tens of nanometers of diamond coating within less than 1 μm away from the apex. Conventional transmission electron microscopy (TEM), electron diffraction and electron energy loss spectroscopy confirm that the coating is composed of dense nanocrystalline diamond with a typical grain size of 20 nm. High resolution TEM reveals graphitic paths between the diamond grains.

1. Introduction

Negative electron affinity (NEA) materials are of great interest for photocathodes due to their high photoelectron yield and low thermal emittance [1-3]. The electron affinity of diamond depends on the exact surface, i.e. chemical species, orientation and reconstruction, and is readily adjustable between +1.7 eV and −1.3 eV with only oxygen and hydrogen as chemisorbed atoms [4]. If the surfaces are terminated by hydrogen, they reveal a comparatively low work function and true NEA, i.e. a conduction band minimum (CBM) above the vacuum level at the solid-vacuum interface. This boosts the photoelectron yield by orders of magnitude, paving the way for a highly efficient photocathode. Photo-excitation happens in the bulk and electrons are emitted into vacuum when they reach the surface, even if they have thermalized to the CBM. This is in contrast to metals, where only photoelectrons excited within the thermalization length below the surface can escape into vacuum. The combination of NEA, high thermal conductivity and mechanical robustness under imperfect vacuum condition make diamond a desirable material for photocathodes.

As the electron emittance - a measure of beam quality - is directly connected to the electron source size, nanosized emitters are favored. Sharp tungsten tips are known as the brightest electron sources in scanning and transmission electron microscopes because of their extremely small virtual source size, which can be even smaller than the nanometer-sized geometrical source size [5,6]. Coating such a sharp tungsten tip with a NEA material like hydrogen-terminated diamond holds promise for an ever brighter photocathode. Since a small source size is important to be maintained, the diamond layer should be thin. The thickness also defines the mean migration time of the excited carriers to the surface. This migration influences the electron pulse duration after pulsed photo-excitation.

All these arguments favor a thin and dense diamond coating on a sharp tungsten tip. For the deposition of such thin layers, a high nucleation/seeding density is crucial. The shorter the mean distance between neighboring nucleation sites, the thinner the resulting dense film can be. Sufficiently high seed densities require appropriate adhesion of the seeds to the substrate, e.g. via electrostatic forces [7,8]. Rheological forces occurring during the drying process of dispersed particle suspensions influence the local seeding density and can lead to phenomena like ring stains, also known as “coffee ring effect” [9]. Therefore, zeta potential adjustment and counteracting of rheological forces are essential for the control of the seeding densities. Moreover, the morphology of the nanodiamond films will play a crucial role for the electron emission properties as well. sp^2-bonded carbon specifically located at the grain boundaries of the film is beneficial in terms of providing sufficient conductivity through the film to prevent charging

---

[*] Corresponding author.
E-mail address: alexander.tafel@fau.de (A. Tafel).

https://doi.org/10.1016/j.diamond.2019.107446
Received 27 July 2018; Received in revised form 5 June 2019; Accepted 6 June 2019
Available online 12 June 2019
0925-9635/ © 2019 Elsevier B.V. All rights reserved.

during operation.

Previous work reported the coating of tips based on electrophoresis [10-12], with bias-enhanced nucleation during chemical vapour deposition (CVD) [13,14], parafin wax and CVD [15] and ultrasonic seeding in nanodiamond slurry with and without a carburization step [16]. In this work, we report a new recipe on the fabrication of diamond-coated tungsten tips via dip-seeding, nitrogen gas flow and CVD. Furthermore, we characterize the structure of the resulting diamond coating. The results are promising for a high brightness diamond-based electron source. This approach is also valuable for the fabrication of samples for local electrode atom probe tomography to investigate the spatial distribution of dopants in ultrathin nanocrystalline diamond films.

2. Experimental

2.1. Tip fabrication

Tungsten wire is etched electrochemically with 3 mol/L aqueous NaOH via the lamellae drop-off technique [17]: A thin film of the electrolyte is trapped in a ring-shaped gold electrode. A bias voltage of 6 V is applied between this gold cathode and tungsten wire - which acts as the anode - until the wire is etched through. A second gold electrode with trapped electrolyte underneath the cathode detects the drop-off and shuts off the etching potential within less than 1 μs to prevent post-etching and blunting of the tip. Freshly etched tips are rinsed with deionised water to remove electrolyte residue. Resulting radii of tungsten tips with this method are typically 5–20 nm.

2.2. Diamond seeding

Sharp tungsten tips are dip-seeded for a few seconds in monodisperse nanodiamond suspensions of crystal diameter of 4–6 nm. Both 0.025 wt.% aqueous suspension from Carbodeon and 0.025 wt.% in dimethyl sulfoxide:methanol 1:3 from Adamas Nanotechnologies were used in this work with comparable results. Due to the oxidized tungsten surface after etching, the zeta potential of the freshly etched tungsten surface is presumably negative at the pH of the seeding suspensions. To ensure good adhesion of the diamond seeds, highly zeta-positive hydrogenated seeds are therefore used. Even though the exact zeta potential of the tungsten surface and of the seeds is not known, this qualitative approach has worked reliably on flat samples and nanotips. Experiments with zeta-negative seeds on flat tungsten samples showed more than one order of magnitude lower seeding densities. Directly after seeding of a nanotip by dip-coating, it is blown dry with pressurized nitrogen gas directed from the shaft towards the tip apex with adjustable flow rates between 0.5 and 2.5$\frac{L}{sec}$ through a nozzle with 3.5 mm diameter.

2.3. Diamond deposition

Diamond deposition is performed in a home-built microwave plasma-enhanced chemical vapor deposition (MPECVD) chamber at 2.5 GHz frequency and 512 W microwave power, at a pressure of 49 mbar using 50 sccm hydrogen and 2 sccm methane flow. The sample holder is heated to 600 °C and then lifted into the plasma. The plasma additionally heats the sample so that the local temperature of the tip apex region is expected to be higher than 600 °C. Deposition times range between 2 and 20 min with a growth rate of approximately 10 $\frac{nm}{min}$. After terminating the diamond growth by switching off the microwave power and sample heater, the sample cools down in a hydrogen atmosphere at 45 mbar. This recipe reliably results in a hydrogen-terminated diamond surface with negative electron affinity [4,18].

2.4. Characterization

Scanning electron microscopy (SEM) is used for routine imaging of the tip geometry and the morphology of the diamond films. In addition, a coated tungsten tip is characterized by imaging, electron diffraction and electron energy loss spectroscopy (EELS) in a Titan Themis transmission electron microscope (TEM) operating at 200 kV. The microscope is equipped with C_s-correctors both at the illumination and imaging side and a Gatan GIF Quantum ER spectrometer. The sample wire was inserted in a Nanofactory STM-TEM holder. The image corrector was tuned to negative C_s imaging condition where the first pass band corresponds to a resolution of 1 Å. We noticed that upon illumination of the tip area, the effective lens aberration can suffer from strong drift at high dose rate. Therefore, a moderate to low dose rate and careful grounding of the STM-TEM holder is necessary to obtain high-resolution TEM (HRTEM) images with good quality. The single electron energy loss (EEL) spectra were acquired directly in TEM diffraction-coupled mode with the largest collection angle - i.e. without objective aperture - to suppress the anisotropic effect in the study of graphite [19].

The EEL spectrum image was acquired in scanning TEM (STEM) mode with an effective collection angle of 30 mrad, a pixel size of 1.1 nm and a short dwell time to balance the sample drift. The low-loss and high-loss (i.e. zero-loss and Carbon 1s region in this study) are acquired with a dispersion of 0.25 eV/channel. The standard Fourier-Log deconvolution method using the recorded zero-loss and plasmon peaks is applied to account for multiple scattering [20]. We use an approximate quantification scheme to extract the sp^2/sp^3 ratio neglecting the anisotropy of the scattering cross section of the graphitic components.

3. Results and discussion

3.1. Diamond seeding and coating

Diamond films deposited after dip-seeding on tungsten foils show clear signs of evaporation dynamics and their influence on local seeding density (see Appendix A). A related effect can be observed when tungsten tips are dip-seeded with nanodiamond suspensions. Without dry-blowing of the dip-seeded tips, continuous and homogeneous coating with diamond was achieved at the shank of the tip, as can be seen in Fig. 1a) –c). The high nucleation density at the shank is presumably a result of the high positive zeta potential of seeds and the negative zeta potential of the tungsten surface. However, the density of diamond crystallites indicating the seeding density clearly decreases towards the tip. Solvent evaporation and the accompanying forces seem to redistribute the seeds, which are pushed away from the tip. To counteract this effect, we adopt a controlled flow of nitrogen gas towards the apex during the drying process. Without the nitrogen gas flow not a single sample out of ten samples was covered with diamond at the apex.

Using pressurized nitrogen gas for dry-blowing immediately after the dip-seeding and consecutive MPECVD, diamond was successfully grown on the tip apex with a 82% success rate (14 out of 17 samples). At moderate flows rates (0.5 –1.0 L/ s), homogeneous coating both at the shank and at the apex is achieved as can be seen in Fig. 1d) –f). Even the sharpest tips with approximately 5 nm radius were succesfully coated with this technique (Fig. 2). At high flow rates (up to 2.5 L/ s), the tungsten tips can even be coated selectively at the apex within less than 1 μm with 20 nm thin diamond (Fig. 1g) –i)). From these observations we deduce that the nitrogen flow successfully counteracts the migration of the seeds away from the apex. If the flow is high enough, the seeds start migrating towards the apex and remain there only.

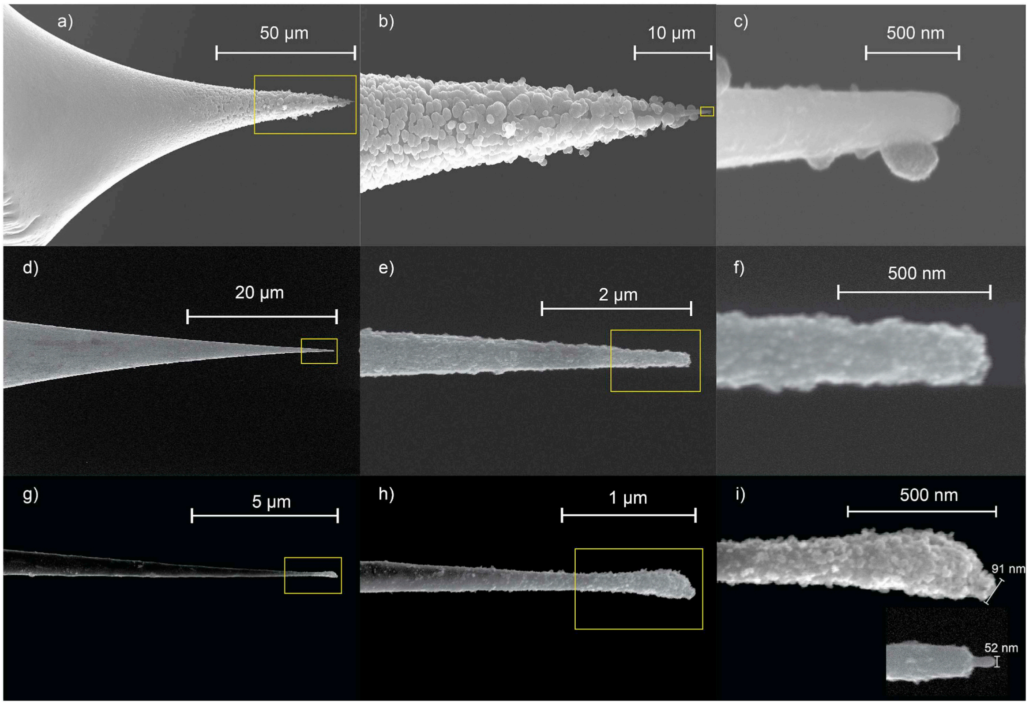

Fig. 1. SEM images of diamond-coated tungsten tips with different nitrogen flow after dip-seeding. a)–c) Zero flow: The seeding density clearly decreases along the tip shank and only few grains are found close to the apex. Homogeneous coating of the apex could not be achieved. d)–f) Moderate flow: The entire tip including the apex is densely covered with nanodiamond. g)–i) Strong flow: Here, the apex region is selectively coated with 20 nm thin diamond. Only the first 400 nm are coated with a dense layer of diamond. From ~ 800 nm behind the apex, the coating is almost absent. The inset in i) is the same tip prior to deposition.

3.2. Structural and chemical characterization

Carbon deposited by MPECVD results in various phases as graphite, diamond and amorphous carbon depending on the exact parameters. The nanocrystalline diamond (NCD) films are expected to be composites of graphitic and diamond phases. Their morphology and composition will have decisive influence on the electron emission properties from coated tips. In order to elucidate the structural details we performed an extensive TEM study on an ultrasharp tungsten tip (apex radius approximately 5 nm) covered by a 100 nm thin NCD film.

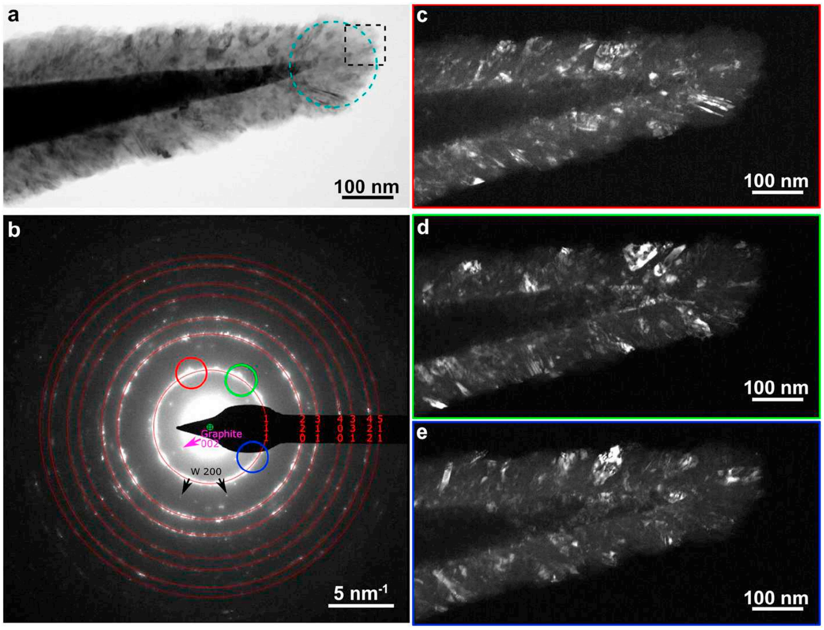

Fig. 2. The columnar nature of the diamond grains on the polycrystalline tungsten tip becomes visible under TEM inspection. (a) Bright-field TEM image of the diamond-coated tungsten tip. The radius of curvature of the coated tip is 100 nm, while the initial W tip radius is ~5 nm. (b) selected area electron diffraction (SAED) pattern of the sample. The calculated diamond powder ring pattern (using kinematical diffraction theory, red circles) is superimposed on the acquired pattern, indicating that the coating is dominated by crystalline diamond. Some weak spots can be assigned to tungsten and graphite as is exemplarily illustrated by the black arrows. (c–e) Dark-field images of the sample with the objective aperture placed at different positions of the {111} diffraction ring as indicated in (b) by the colored circles. Single grains oriented such that the {111} Bragg condition is satisfied are revealed this way and the columnar shape as well as the characteristic grain size of 20 nm is revealed. The high resolution image in Fig. 5 is obtained at the dashed black box in (a) and the EEL spectrum shown in Fig. 3 is acquired in the blue dashed circle region in (a).

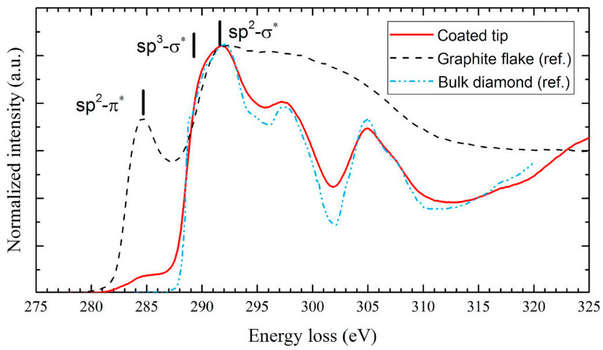

Fig. 3. EEL spectrum acquired in the blue dashed circle region in Fig. 2 (a) with characteristic peaks of nanocrystalline diamond, in-situ graphite reference (black) and bulk diamond (blue) [21].

Fig. 2a) shows a bright-field image of the tip. The tungsten is seen dark in the center and is covered by a gray layer of NCD. The selected area electron diffraction (SAED) pattern shown in Fig. 2b) was acquired using an aperture covering an area with about 200 nm radius over the tip region showing diffraction rings perfectly matching the powder pattern of diamond (red circles in Fig. 2b)). This confirms that the coated layer is dominated by diamond crystallites. Some additional weak spots that do not belong to diamond can be attributed to tungsten and graphite. Although the experimental diffraction ring pattern fills each circle completely, some sparse segments and strong spots can be seen especially on the {220} diffraction ring.

This is due to the textured structure of the diamond grains. However, the texture can hardly be retrieved from this diffraction pattern alone and will be a subject of future research. In order to reveal the shape of the diamond grains more clearly, a series of dark-field images was recorded with the objective aperture placed at different azimuth location of the diamond {111} diffraction ring as indicated by the colored circles in Fig. 2b). The corresponding images are displayed in Fig. 2 (c–e). The columnar shape of the diamond grains with a width of about 20 nm is clearly evidenced by these dark-field images. The grain columns seem to align themselves at a small angle to the surface normal. On closer inspection, the columnar grains are also faintly visible in the bright-field image in Fig. 2a).

Fig. 3 presents the background substracted EEL spectrum recorded from the tip region marked by the dashed circle in Fig. 2 (a), as well as graphitic and diamond reference spectra. The fine structure of the carbon K-edge in the EEL spectrum reflects the orbital character of the conduction band states. Transitions into $sp^2-\sigma^*$ antibonding states, which form the upper part of the graphite conduction band, create a broad and featureless band in the EEL spectrum with a maximum at 292 eV. The diamond conduction band with $sp^3-\sigma^*$ character is also reflected as a broad band in the K-edge EEL sprectrum with a threshold at about 290 eV and peaks at 292, 297 and 305 eV. These peaks are well resolved in the spectrum of the coated tip (Fig. 3) and their presence is a clear proof that the coating is diamond [21].

Both the tip and the graphitic reference spectrum show a well resolved peak at 285 eV loss energy that is assigned to electron transitions into $sp^2-\pi^*$ antibonding states. As the $sp^2-\pi^*$ signal is absent for

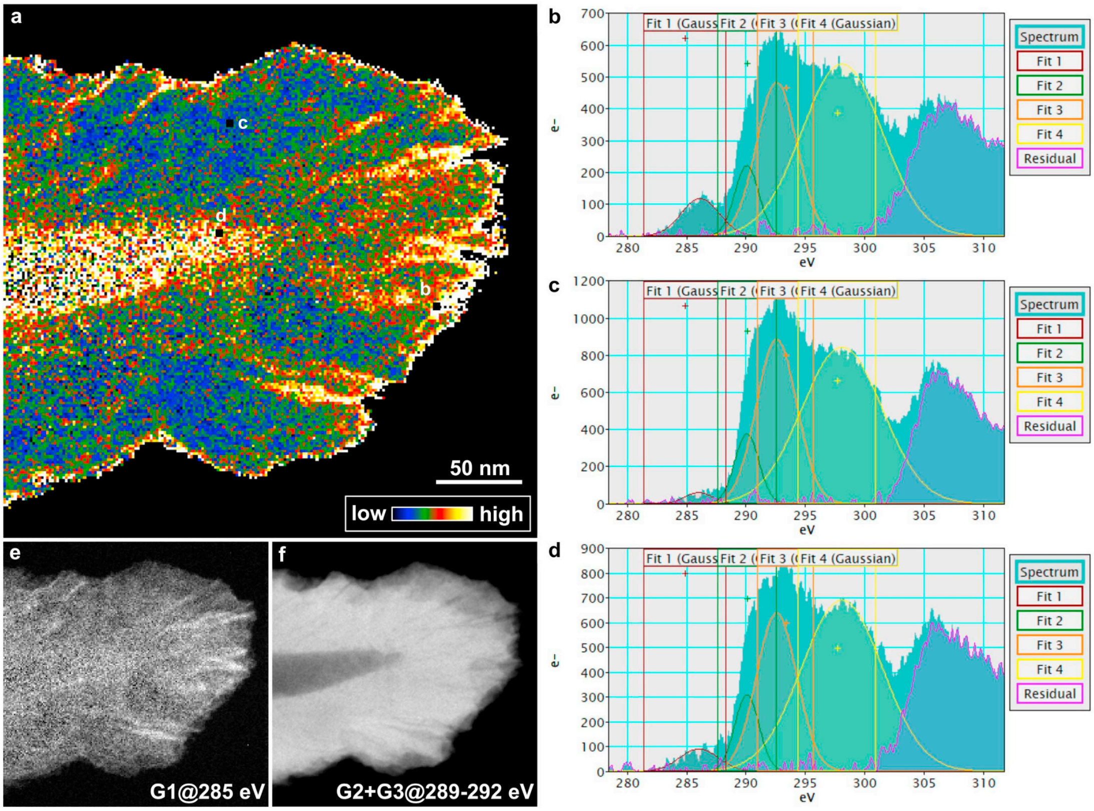

Fig. 4. Qualitative map of the ratio of sp^2- to sp^3-bonded carbon. (a) Evaluated map after the simple formula and processing method in Appendix B. More sp^2-bonded carbon is found in the axial region of the apex. The high ratio at the surface is due to carbon deposition (contamination) during the STEM-EELS measurement. The (deconvoluted and background subtracted) spectra denoted at positions b, c and d are shown in (b)–(d), respectively. (e) Intensity of extracted Gaussion peak 1 (G1) at 285 eV and (f) sum of Gaussian peak 2 and 3 (G2 + G3) at 289 and 292 eV, respectively.

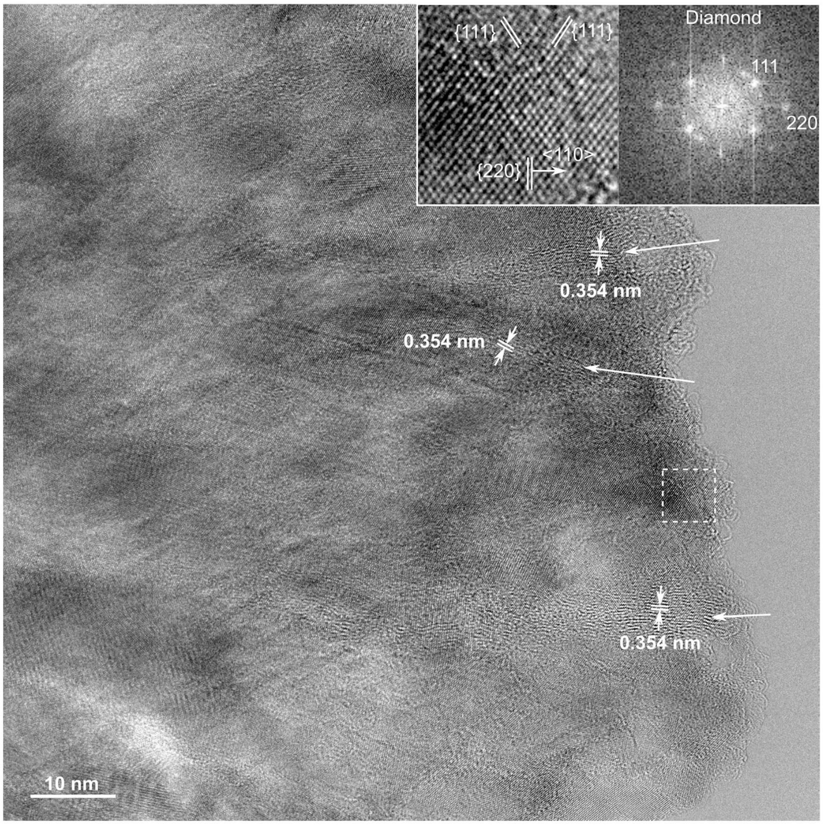

Fig. 5. HRTEM image of the diamond coating at the apex of the tungsten tip. Graphitic paths between the grains with interplane distance of 0.354 nm are visible. The dashed boxed region is magnified as inset with its Fourier transform shown on the right side.

monocrystalline diamond, the integral of appropriate energy windows holds quantitative information on the ratio of *sp*^{2}- to *sp*^{3}-bonded carbon [22-25]. Fig. 4 shows the pixel-wise evaluated *sp*^{2} to *sp*^{3} ratio from the spatially-resolved STEM-EELS spectra (for details of the evaluation, see Appendix B). The map reveals that the average *sp*^{2} content is larger at the apex and that paths of high *sp*^{2} content are present which align with the axes of the single grains (Fig. 2 & 4). The large *sp*^{2} content at the apex is attributed to a larger seeding density at the apex as Fig. 1 shows that the seeds adhere well to the apex after dry-blowing with nitrogen.

Further insight into the morphology of the film, specifically the location of the *sp*^{2}-bonded tissue, is given by the HRTEM image in Fig. 5. Wavy lattice fringes with a characteristic distance of 354 pm corresponding to the interlayer spacing of graphite can be seen. Some fringes are marked in white in Fig. 5 for easier identification. Apparently, the graphitic components form contiguous paths between the diamond crystallites, which promises sufficient conductivity of the composite film to prevent charging of the tip during electron emission in future applications.

At the tip, one can see a few grains showing 2D lattice fringes. From the lattice fringe distances, one can attribute the lattice plane indices and plane normal directions. A small region as marked by the dotted box in Fig. 5 is magnified in the inset with its Fourier transform on the upper right side. The {111} and {220} lattice planes can be easily recognized. However, drawing general conclusions about texture requires a thinner coating and will be a subject of future studies.

4. Conclusion

Tungsten tips with apex radii down to 5 nm have been successfully coated with dense nanocrystalline diamond films with a thickness as small as 20 nm. Solvent evaporation after seeding has a large effect on the local seeding density, especially at strongly curved surfaces, and must be engineered appropriately. To counteract evaporation forces, we adopt a nitrogen gas flow towards the tip apex. Diamond deposition on shaft only, apex only as well as homogeneous coating of shaft and apex is achieved by variation of the nitrogen flow. We achieved the growth of 20 nm thin diamond limited to less than 1 μm away from the tip apex by this technique. EELS and electron diffraction of a coated tungsten tip confirm the presence of diamond with a fraction of *sp*^{2}-bonded carbon, identified as graphitic paths in between grains via HRTEM images. A spatially resolved STEM-EELS measurement shows an elevated fraction of the relative *sp*^{2}-content at the tip apex. Furthermore, a columnar radial growth of diamond crystallites with a typical grain size of 20 nm is revealed. We expect that these diamond-coated tungsten tips with negative electron affinity offer a great potential for the use as high brightness photocathodes both in dc and ultrafast laser-triggered operation.

Acknowledgments

We thank J. Litzel for setting up and modernizing the MPECVD reactor. This work was supported by the ERC (European Research Counsil, EU) grant “Near Field Atto”, DFG (Deutsche Forschungsgemeinschaft, Germany) research training group “In-situ Microscopy with Electrons, X-rays and Scanning Probes”(GRK 1896) and DFG collaborative research center “Synthetic carbon allotropes” (CRC 953).

Appendix A. Deposition on tungsten foil

Diamond deposition on dip-seeded tungsten foils have shown signs of solvent evaporation effects. Circular spots with radially growing crystallite density were often observed (Fig. A.6 a)–c), sometimes accompanied by larger ring stains (Fig. A.6 d)). The former is a result of an evaporation front pushing seeds radially outwards whereas the latter is formed due to fluid dynamics inside the solvent happening due to evaporation [9]. These results are additional hints, that solvent evaporation plays an important role for the dip-seeding of nanotips.

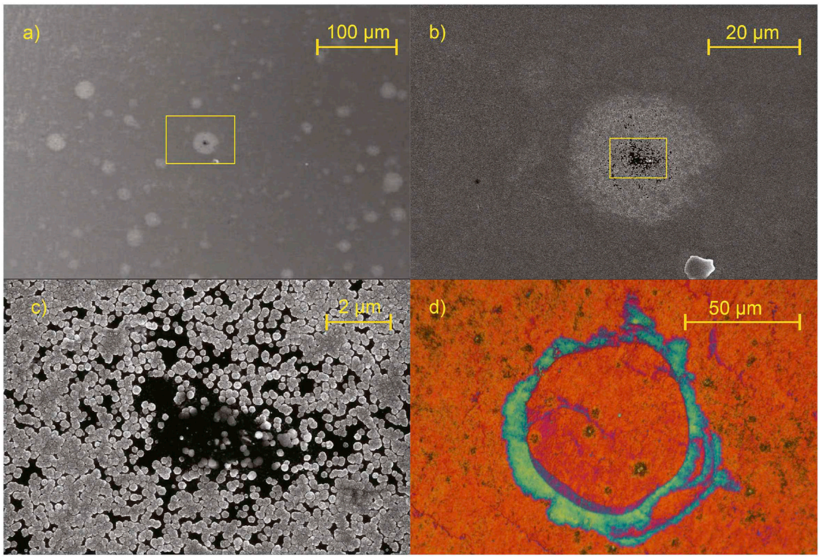

Fig. A.6. a)–c) SEM images at various magnifications of a flat tungsten foil coated with CVD diamond after dip-seeding in nanodiamond suspension. The patterns show characteristic circular features. Seeds are pushed radially outwards during evaporation. d) Optical microscope image with circular area of larger thickness; colors arise due to thin film interference. Ring stains form due to fluid dynamics during evaporation. (Different sample than a)–c)).

Appendix B. EELS analysis

A mixture of sp^2- and sp^3-bonded carbon with atomic sp^2-fraction x contains N_σ σ-orbitals and N_π π-orbitals.

$$N_\sigma = (3 \cdot x + 4 \cdot (1 - x)) \cdot N_{at} \tag{B.1}$$

$$N_\pi = x \cdot N_{at} \tag{B.2}$$

$$\rightarrow x = \frac{4 \cdot N_\pi}{N_\sigma + N_\pi} \tag{B.3}$$

Where N_{at} is the total number of carbon atoms. Therefore the ratio of sp^2- to sp^3-bonded carbon y becomes

$$y = \frac{x}{1 - x} = \frac{4 \cdot N_\pi}{N_\sigma - 3 \cdot N_\pi} \tag{B.4}$$

To deconvolute the contributions in the EEL spectra, we fit three gaussians with center energy 285, 289 and 292 eV to the spectrum. Assuming that N_π is proportional to the area under the gaussian centered at 285 eV and N_σ is proportional to the area under the other two Gaussians with the same proportionality factor, we calculate y for every pixel of the STEM-EEL spectrum. This is a simplified picture of the situation, but sufficient for a spatially resolved qualitative comparison of y. The graphitic reference spectrum shown in Fig. 3 cannot be used for a quantitative analysis due to the anisotropy of the scattering cross section with respect to crystal orientation, which was not matched between the coated tip and the reference sample.

Since graphite is highly anisotropic, the ratio between the inelastic scattering cross sections into σ^* and π^* orbitals depends strongly on the scattering angle and the angle between the incoming beam and the graphitic c-axis. Fortunately, this latter dependence vanishes for a specific so called magic scattering angle [26]. Choosing this angle in EELS experiments in combination with reference samples of known composition allows a quantitative imaging of y for arbitrary orientation of the graphitic fraction, i.e. independent of the substrate geometry and texture. Such experiments are a subject of ongoing research.

References

[1] W.E. Spicer, Negative affinity 3–5 Photocathodes: their physics and technology, Appl. Phys. 12 (2) (1977) 115–130, https://doi.org/10.1007/BF00896137 (feb 1977).

[2] F. Machuca, Y. Sun, Z. Liu, K. Ioakeimidi, P. Pianetta, R.F.W. Pease, Prospect for high brightness III–nitride electron emitter, J. Vac. Sci. Technol., B: Microelectron. Nanometer Struct. 18 (6) (2000) 3042, https://doi.org/10.1116/1.1321270.

[3] J. Cui, J. Ristein, M. Stammler, K. Janischowsky, G. Kleber, L. Ley, Hydrogen termination and electron emission from CVD diamond surfaces: a combined secondary electron emission, photoelectron emission microscopy, photoelectron yield, and field emission study, Diamond Relat. Mater. 9 (3-6) (2000) 1143–1147, https://doi.org/10.1016/S0925-9635(99)00279-4 (apr 2000).

[4] F. Maier, J. Ristein, L. Ley, Electron affinity of plasma-hydrogenated and chemically oxidized diamond (100) surfaces, Phys. Rev. B 64 (16) (2001) 165411, https://doi.org/10.1103/PhysRevB.64.165411 (oct 2001).

[5] J.C.H. Spence, High-Resolution Electron Microscopy, 4th ed., Oxford University Press, 2013.

[6] D. Ehberger, J. Hammer, M. Eisele, M. Krüger, J. Noe, A. Högele, P. Hommelhoff, Highly coherent electron beam from a laser-triggered tungsten needle tip, Phys. Rev. Lett. 114 (22) (2015) 227601, https://doi.org/10.1103/physrevlett.114.227601 (jun 2015).

[7] J. Hees, A. Kriele, O.A. Williams, Electrostatic self-assembly of diamond nanoparticles, Chem. Phys. Lett. 509 (1-3) (2011) 12–15, https://doi.org/10.1016/j.cplett.2011.04.083 (jun 2011).

[8] S. Mandal, E.L.H. Thomas, C. Middleton, L. Gines, J.T. Griffiths, M.J. Kappers, R.A. Oliver, D.J. Wallis, L.E. Goff, S.A. Lynch, M. Kuball, O.A. Williams, Surface zeta potential and diamond seeding on gallium nitride films, ACS Omega 2 (10) (2017) 7275–7280, https://doi.org/10.1021/acsomega.7b01069 (oct 2017).

[9] R.D. Deegan, O. Bakajin, T.F. Dupont, G. Huber, S.R. Nagel, T.A. Witten, Capillary flow as the cause of ring stains from dried liquid drops, Nature 389 (6653) (1997) 827–829, https://doi.org/10.1038/39827 (oct 1997).

[10] V. Zhirnov, W. Choi, J. Cuomo, J. Hren, Diamond coated Si and Mo field emitters: diamond thickness effect, Appl. Surf. Sci. 94-95 (1996) 123–128, https://doi.org/10.1016/0169-4332(95)00520-x (mar 1996).

[11] A.N. Alimova, N.N. Chubun, P.I. Belobrov, P.Y. Detkov, V.V. Zhirnov, Electrophoresis of nanodiamond powder for cold cathode fabrication, J. Vac. Sci. Technol., B: Microelectron. Nanometer Struct. 17 (2) (1999) 715, https://doi.org/10.1116/1.590625.

[12] W.B. Choi, J.J. Cuomo, V.V. Zhirnov, A.F. Myers, J.J. Hren, Field emission from silicon and molybdenum tips coated with diamond powder by dielectrophoresis, Appl. Phys. Lett. 68 (5) (1996) 720–722, https://doi.org/10.1063/1.116585 (jan 1996).

[13] J. Liu, V.V. Zhirnov, G.J. Wojak, A.F. Myers, W.B. Choi, J.J. Hren, S.D. Wolter, M.T. McClure, B.R. Stoner, J.T. Glass, Electron emission from diamond coated silicon field emitters, Appl. Phys. Lett. 65 (22) (1994) 2842–2844, https://doi.org/10.1063/1.112538 (nov 1994).

[14] S. Albin, W. Fu, A. Varghese, A.C. Lavarias, G.R. Myneni, Diamond coated silicon field emitter array, J. Vac. Sci. Technol. A 17 (4) (1999) 2104–2108, https://doi.org/10.1116/1.581733 (jul 1999).

[15] J. Palomino, D. Varshney, O. Resto, B.R. Weiner, G. Morell, Ultrananocrystalline Diamond-decorated silicon nanowire field emitters, ACS Appl. Mater. Interfaces 6 (16) (2014) 13815–13822, https://doi.org/10.1021/am503221t (jul 2014).

[16] Y.-F. Tzeng, C.-Y. Lee, H.-T. Chiu, N.-H. Tai, I.-N. Lin, Electron field emission properties on ultra-nano-crystalline diamond coated silicon nanowires, Diamond Relat. Mater. 17 (7-10) (2008) 1817–1820, https://doi.org/10.1016/j.diamond.2008.03.023 (jul 2008).

[17] M. Klein, G. Schwitzgebel, An improved lamellae drop-off technique for sharp tip preparation in scanning tunneling microscopy, Rev. Sci. Instrum. 68 (8) (1997) 3099–3103, https://doi.org/10.1063/1.1148249 (aug 1997).

[18] J.B. Cui, M. Stammler, J. Ristein, L. Ley, Role of hydrogen on field emission from chemical vapor deposited diamond and nanocrystalline diamond powder, J. Appl. Phys. 88 (6) (2000) 3667–3673, https://doi.org/10.1063/1.1288163 (sep 2000).

[19] R.D. Leapman, P.L. Fejes, J. Silcox, Orientation dependence of core edges from anisotropic materials determined by inelastic scattering of fast electrons, Phys. Rev. B 28 (5) (1983) 2361–2373, https://doi.org/10.1103/physrevb.28.2361 (sep 1983).

[20] R. Egerton, Electron Energy-Loss Spectroscopy in the Electron Microscope, Springer US, 2011, https://doi.org/10.1007/978-1-4419-9583-4.

[21] S.L.Y. Chang, A.S. Barnard, C. Dwyer, C.B. Boothroyd, R.K. Hocking, E. Ōsawa, R.J. Nicholls, Counting vacancies and nitrogen-vacancy centers in detonation nanodiamond, Nanoscale 8 (20) (2016) 10548–10552, https://doi.org/10.1039/c6nr01888b (2016).

[22] R. Lossy, D.L. Pappas, R.A. Roy, J.P. Doyle, J.J. Cuomo, J. Bruley, Properties of amorphous diamond films prepared by a filtered cathodic arc, J. Appl. Phys. 77 (9) (1995) 4750–4756, https://doi.org/10.1063/1.359411 (may 1995).

[23] J.J. Cuomo, J.P. Doyle, J. Bruley, J.C. Liu, Sputter deposition of dense diamond-like carbon films at low temperature, Appl. Phys. Lett. 58 (5) (1991) 466–468, https://doi.org/10.1063/1.104609 (feb 1991).

[24] D.L. Pappas, K.L. Saenger, J. Bruley, W. Krakow, J.J. Cuomo, T. Gu, R.W. Collins, Pulsed laser deposition of diamond-like carbon films, J. Appl. Phys. 71 (11) (1992) 5675–5684, https://doi.org/10.1063/1.350501 (jun 1992).

[25] S.D. Berger, D.R. McKenzie, P.J. Martin, EELS analysis of vacuum arc-deposited diamond-like films, Philos. Mag. Lett. 57 (6) (1988) 285–290, https://doi.org/10.1080/09500838808214715 (jun 1998).

[26] H. Daniels, A. Brown, A. Scott, T. Nichells, B. Rand, R. Brydson, Experimental and theoretical evidence for the magic angle in transmission electron energy loss spectroscopy, Ultramicroscopy 96 (3-4) (2003) 523–534, https://doi.org/10.1016/s0304-3991(03)00113-x (sep 2003).

Author contribution for publication

Femtosecond Laser-Induced Electron Emission from Nanodiamond-Coated Tungsten Needle Tip

Physical Review Letters 123, 146802, **2016**

Authors: A. Tafel, S. Meier, J. Ristein, P. Hommelhoff

Co-Author's contributions:

- Support in writing of the manuscript
- Support in conducting stability measurement with Ti:Sa oscillator
- Developing the emission model
- Interpretation of data

A. Tafel's contributions:

- Writing of the manuscript
- Sample fabrication
- Conducting all experiments
- Analyzing data
- Interpretation of data
- Developing the emission model

PHYSICAL REVIEW LETTERS **123,** 146802 (2019)

Femtosecond Laser-Induced Electron Emission from Nanodiamond-Coated Tungsten Needle Tips

A. Tafel,[*] S. Meier, J. Ristein, and P. Hommelhoff
Department of Physics, Friedrich-Alexander-Universität Erlangen-Nürnberg, Staudtstraße 1, D-91058 Erlangen, Germany

(Received 13 March 2019; revised manuscript received 19 July 2019; published 2 October 2019)

We present femtosecond laser-induced electron emission from nanodiamond-coated tungsten tips. Based on the shortness of the femtosecond laser pulses, electrons can be photoexcited for wavelengths from the infrared (1932 nm) to the ultraviolet (235 nm) because multiphoton excitation becomes efficient over the entire spectral range. Depending on the laser wavelength, we find different dominant emission channels identified by the number of photons needed to emit electrons. Based on the band alignment between tungsten and nanodiamond, the relevant emission channels can be identified as specific transitions in diamond and its graphitic boundaries. It is the combination of the character of initial and final states (i.e., bulk or surface-near, direct or indirect excitation in the diamond band structure), the number of photons providing the excitation energy, and the peak intensity of the laser pulses that determines the dominant excitation channel for photoemission. A specific feature of the hydrogen-terminated nanodiamond coating is its negative electron affinity that significantly lowers the work function and enables efficient emission from the conduction band minimum into vacuum without an energy barrier. Emission is stable for bunch charges of up to 400 electrons per laser pulse. We infer a normalized emittance of <0.20 nm rad and a normalized peak brightness of $>1.2 \times 10^{12}$ A m^{-2} sr^{-1}. The properties of these tips are encouraging for their use as laser-triggered electron sources in applications such as ultrafast electron microscopy as well as diffraction and novel photonics-based laser accelerators.

DOI: 10.1103/PhysRevLett.123.146802

Tip-shaped cathodes are among the most commonly used electron sources in electron microscopy due to their ability to provide a high quality beam. Typical materials are zirconia in common Schottky type emitters and lanthanum hexaboride because of their low work function, as well as tungsten due to the easy fabrication of sharp tips ideally suited for (cold) field emission [1]. Most of the commonly used emitters are operated under ultrahigh vacuum conditions in the 10^{-8}–10^{-9} Pa regime to minimize bombardment with ionized gas and adsorption on the emitter surface. Furthermore, they are heated for thermal enhancement of the emission or to achieve stable operation due to reduced adsorption.

Over the last decades, ultrafast electron microscopy has emerged [2–4]. Until today, emitters, which were designed for dc operation, are also used in ultrafast mode. In the latter case, the cathode is typically triggered by femtosecond laser pulses resulting in femto- to picosecond electron pulses [5–10]. One of the major drawbacks of these laser-triggered electron sources is the continuous decrease of emission current over time [5,9,10], which is attributed to laser-induced changes at the emitter surface. Femtosecond laser-induced photoemission from tip-shaped cathodes has been extensively studied for the materials of tungsten [11–16], gold [17–19], silver [20], hafnium carbide [21], and carbon nanotubes [22,23]. Pulsed photoemission from single crystal diamond tips has been investigated with nanosecond pulses [24]. Femtosecond photoemission from tip-shaped heterostructures offers promising opportunities yet to be discovered.

Diamond is one of the most robust materials due to its exceptional chemical inertness, mechanical strength, and thermal conductivity. Nanocrystalline diamond (NCD) is a good electron emitter, especially if the surface exhibits negative electron affinity (NEA) [25]. The graphitic grain boundaries in this composite material provide electrical conductivity, and the low work function of the diamond matrix that goes along with the NEA lowers the surface energy barrier for the electrons, even if they originate from the graphitic parts [25]. NEA is also known to boost the photoelectron yield due to fundamental absorption, i.e., optical excitation across the band gap: electrons photoexcited into the diamond conduction band can be emitted into vacuum without any barrier after migration to the surface [26,27]. The electron affinity of hydrogen-terminated diamond is as low as -1.3 eV for both main crystallographic surfaces (100) [28] and (111) [29].

The combination of high beam quality from tip-shaped photocathodes with the mechanical strength and the low work function of hydrogen-terminated diamond promises a robust and high-brightness photocathode. Here, we present the first photoemission results from a tip-shaped semiconductor/metal heterostructure—diamond-coated tungsten tips—triggered with femtosecond laser pulses, and

0031-9007/19/123(14)/146802(6) © 2019 American Physical Society

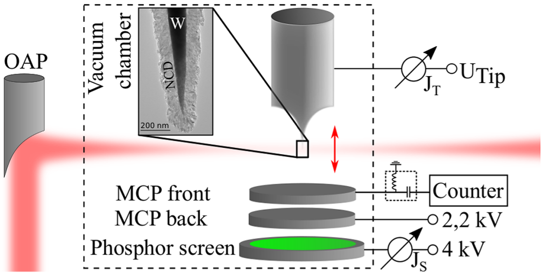

FIG. 1. Experimental setup. The laser is focused onto the diamond-coated tungsten tip with an off-axis parabolic mirror (OAP). The inset shows a transmission electron micrograph of the nanodiamond-coated tungsten tip. A voltage clearly below the dc field emission threshold is applied between the tip and the microchannel plate (MCP) to accelerate electrons towards the MCP. See text for details.

we characterize the underlying photoemission physics by identifying various emission channels. We define an emission channel as the combination of photon energy and energy states involved in the photoemission process of electrons.

To obtain the nanodiamond-coated tips, 100 μm diameter tungsten wire is electrochemically etched, resulting in a tip with a typical apex radius of roughly 10 nm. The freshly etched tip is dip seeded in nanodiamond suspension and dry blown with pressurized nitrogen. NCD is grown on the seeded tips with microwave-enhanced chemical vapor deposition, resulting in a dense film of hydrogen-terminated nanocrystalline diamond with negative electron affinity covering the tungsten surface (Fig. 1 inset). A thin layer of tungsten carbide (WC) is expected to be formed at the diamond-tungsten interface [30]. Samples used in this work have apex radii between 60 and 200 nm, including the diamond coating. Details of the fabrication process and a structural characterization of the tips are published elsewhere [31].

The so-fabricated tips are mounted in an ultrahigh vacuum chamber with a base pressure of 1×10^{-7} Pa. Femtosecond laser pulses are focused at the tip with the help of a 51 mm diameter off-axis parabolic mirror with a 152 mm focal length outside of the vacuum chamber, resulting in a measured spot radius of 3.8 μm at 512 nm ($1/e^2$ intensity radius). The employed commercial laser system consists of a regeneratively amplified Ti:Sa oscillator (1 kHz repetition rate, 80 fs pulse duration), an optical parametric amplifier, and a stage for second harmonic and sum-frequency generation. Additionally, a Ti:Sa oscillator (780 nm, 80 MHz, 6 fs) is used for long-term stability measurements. We apply a negative voltage below 50% of the dc field emission threshold (400–2000 V, depending on the individual tip). Due to the dielectric surface with a small work function of 2.8 eV [Eq. (2)], the Schottky reduction is lower as compared to metal tips and is neglected here. The dc field is chosen low enough that photon-assisted field emission does not occur: only multiphoton emission. The laser pulses are linearly polarized parallel to the tip axis. Photoemitted electrons are detected with a microchannel plate (MCP) with a grounded front plate. For bunch charges below one electron per laser pulse, we count detection events on the MCP; above one electron per pulse, we measure the calibrated MCP screen current; and for large average currents at high repetition rates, we are able to additionally measure the current through the tip.

In order to identify the different contributions to the photoelectron current J, we have measured its dependence on the peak intensity I_p. Due to the high I_p of the femtosecond laser pulses, optical excitation is not limited to one-photon absorption processes as the multiphoton absorption becomes efficient. The dependence of the photoelectron current J on I_p is expected to be a sum of power law contributions:

$$J = \sum_{n}^{\infty} a_n I_p^n, \tag{1}$$

where n reflects the number of photons necessary to provide the excitation energy, and a_n is the corresponding coefficient for the specific emission channel. Often, one channel is dominant; hence, the slope of $\log(J)$ vs $\log(I_p)$ directly reveals the photon order n. If more than one channel is involved with comparable strength, the linearized slope is a noninteger and is called effective nonlinearity. Depending on the photon energy and laser intensity, different emission channels can become dominant. We show the power dependence of the photoelectron current at wavelengths of 1932, 512, and 256 nm in Fig. 2. For 1932 nm, we find an integer slope of 5.0, indicating a single dominating emission channel with five photons. At 512 nm, the plot shows an effective nonlinearity of 3.4. This is indicative for two channels with photon orders of 3 and 4 contributing. At 256 nm, we observe a transition from photon order one at low intensities to photon order two at high intensities.

In the UV (235–350 nm), we have investigated the wavelength dependence of the effective nonlinearity in more detail. Figure 3(a) shows the $\log(J)$ vs $\log(I_p)$ plot for 235, 260, and 350 nm. We find effective nonlinearities of 1.1, 1.4, and 2.0, respectively. Again, this reflects the transition of the dominant emission channel from first to second order. Note that we do not observe a transition in the power dependence directly in contrast to Fig. 2(b). This is due to the restricted pulse energy range in Fig. 3. The effective nonlinearities for all wavelengths in the UV are summarized in Fig. 3(b), confirming the transition mentioned above.

For the interpretation of the data, we sketch the energy states relevant for this work in Fig. 4. Five junctions between W/WC, diamond, vacuum, and the graphitic grain boundaries (called graphite in Fig. 4) are formed.

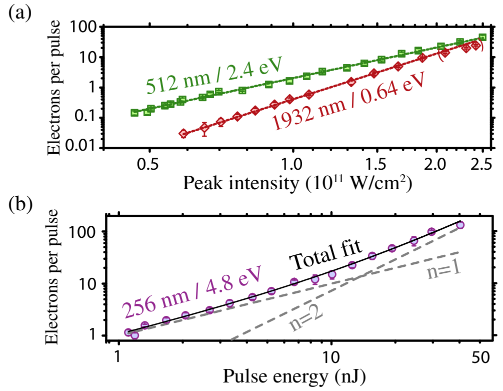

FIG. 2. (a) Photoemission at 1932 nm (red diamonds) and 512 nm (green squares), with slopes of 5.0 (red dashed line, with last three data points not included due to potential saturation effects) and 3.4 (green dashed line). (b) Transition from one- to two-photon emission at 256 nm. Gray dashed lines are corresponding contributions, and the solid black line is the sum of the two contributions. Note that we used pulse energy instead of peak intensity in Fig. 2(b) because we could not measure the laser spot size in the UV.

Diamond forms Schottky junctions with graphite and W/WC with Schottky barriers of $E_{B,G} = 1.4$ eV [32] and $E_{B,\mathrm{W/WC}} = 1.2$ eV [33], respectively. As the sample surface only consists of diamond grains and their graphitic boundaries, the junctions of diamond-vacuum and graphite-vacuum are the relevant ones for electron emission into vacuum. In a heterosystem involving metallic (W/WC and, in a good approximation, the half-metal graphite) and semiconducting (diamond) components, the Fermi level in the semiconductor relative to the valence band maximum (VBM) is identical to the Schottky barrier height as long as the dimensions of the semiconducting parts are much below the Debye length of the semiconductor. This is certainly the case for the diamond grains. We expect $E_{B,G}$ to dominate at the diamond surface because the average grain size (approximately 20 nm) is smaller than the thickness of the diamond film. Consequently, the Fermi level is $E_{B,\mathrm{W/WC}} = 1.2$ eV above the VBM at the back contact and $E_{B,G} = 1.4$ eV above the VBM at the free surface [see Fig. 4(a)]. The work function Φ is defined as the energy difference between the vacuum level and the surface Fermi level. Graphite has a work function of 4.7 eV [34], whereas the work function of diamond depends on the electron affinity χ, and $E_{B,G}$ and results in

$$\Phi_{\mathrm{dia}} = E_g - E_{B,G} + \chi = (5.5 - 1.4 - 1.3)\ \mathrm{eV} = 2.8\ \mathrm{eV}, \tag{2}$$

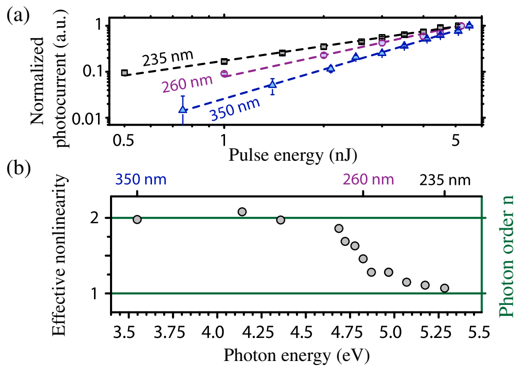

FIG. 3. Power scaling in the UV with transition from one- to two-photon emission as the dominant channel. (a) Data at 235 (black squares), 260 (violet circles), and 350 nm (blue triangles) with effective nonlinearities of 1.1, 1.4, and 2.0, respectively. (b) Effective nonlinearity vs Photon energy with a gradual transition from $n = 1$ to $n = 2$ at roughly 4.8 eV.

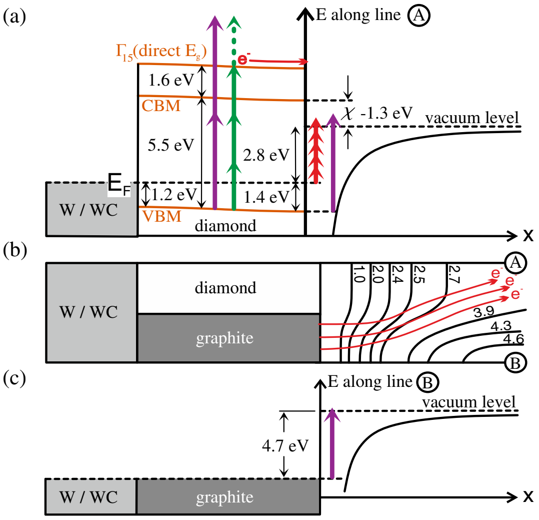

FIG. 4. Sketch of the relevant energy levels and optical excitation paths in the nanodiamond needle tip coating, including the graphitic boundaries. The concatenated arrows indicate excitation channels we identify as relevant here. The length and color of the arrows in Figs. 4(a) and 4(c) represent the photon energies of 0.64 (near infrared), 2.4 (green), and 4.8 eV (near ultraviolet). With these photoexcitation channels, we can explain the observed laser power and wavelength dependence discussed around Figs. 2 and 3. Intriguingly, this emission channel identification, except for the assignment of the one-photon process in the UV, seems to result in a unique attribution in spite of the intricate level structure. The work function of diamond is 2.8 eV for a negative electron affinity of $\chi = -1.3$ eV. In the diamond bulk, electrons can be excited across the indirect (5.5 eV) or direct band gap (7.1 eV), with two ultraviolet or three green photons, migrate to the surface, and cross the surface into vacuum. Alternatively, electrons can be excited into vacuum directly by one ultraviolet or five infrared photons. Even if the electrons originate from graphite close to the diamond interface, they effectively feel the work function of diamond, as indicated by their trajectories across the equipotential lines in Fig. 4(b). See text for details.

where we inserted −1.3 eV for the electron affinity of a fully hydrogen-terminated diamond surface [29,35]. The diamond work function also constitutes the low energy threshold for electrons originating from graphite [see Fig. 4(b)].

Based on this band diagram, we can identify electron emission channels with different energy thresholds, as indicated in Fig. 4(a). For diamond with negative electron affinity, the energy barrier between the conduction band minimum (CBM) at the surface does not exist: Electrons can be excited into the conduction band across the indirect (5.5 eV [36]) and direct band gaps (7.1 eV [37,38]), migrate to the surface, and escape straight into vacuum even if they have thermalized to CBM. Alternatively, direct optical excitation from electronic states at the surface to the plane-wave-like states in vacuum can lead to photoelectrons as well.

The emission probabilities of the different channels are complex functions of the densities of initial and final states, the number of photons necessary to provide the transition energy, and the laser intensity. We discuss them by referring to their signature in the $\log(J)$ vs $\log(I_p)$ plots in Figs. 2 and 3. Excitation with 1932 nm [$\hbar\omega = 0.64$ eV; red arrows in Fig. 4(a)] and observed photon order 5 can be identified as transitions at the surface from the Fermi level to the vacuum level. For clearer presentation, we have sketched the red arrows only in Fig. 4(a), although the initial states at the Fermi level can be assigned either to defects in the diamond or, more likely, to the graphitic grain boundaries [27].

At 512 nm ($\hbar\omega = 2.4$ eV; green arrows in Fig. 4), the effective nonlinearity equals 3.4, which we attribute to excitation across the direct band gap by three or by four photons.

With UV excitation ($\lambda < 350$ nm and $\hbar\omega > 3.5$ eV; violet arrows in Fig. 4), we observe one- and two-photon processes [Figs. 2(b) and 3]. We assign the one-photon process at low intensities to excitation at the surface from the Fermi level or the diamond VBM to the vacuum level. Evaluating energy differences only, the two-photon process ($\Delta E > 7.2$ eV for $\lambda < 350$ nm) could be assigned to all transitions in the band diagram of Fig. 4. We suggest, for this process, the transition across the direct band gap of diamond: The spatial overlap of the wave functions, the direct nature of the transition, and the large excitation volume make this process, by far, the most likely. This argument is supported also by the nonlinearity of 3.4, which we observe for 512 nm ($\hbar\omega = 2.4$ eV): Two photons of that energy would suffice to excite electrons from the VBM directly into vacuum. Nevertheless, this channel is not observed as the dominant one. The situation is different for 1932 nm ($\hbar\omega = 0.64$ eV): With this wavelength, excitation across the indirect band gap would require 9 photons and 11 photons across the direct band gap. These extremely high order processes are so unlikely that we observe the fifth order process at the surface as the dominant channel instead. For the spectral range investigated, we find no evidence of absorption across the indirect band gap as the dominant mechanism.

Lastly, we characterize the photoemission stability over time at different bunch charges and estimate the normalized peak brightness $B_{p,\mathrm{norm}}$. For the best comparison of $B_{p,\mathrm{norm}}$ with existing literature on ultrafast tip-shaped electron sources [8,9], we calculate all quantities as normalized root-mean-squared (rms) values and use the following definition:

$$B_{p,\mathrm{norm}} = \frac{J_p}{4\pi^2 \varepsilon_{x,\mathrm{norm}} \varepsilon_{y,\mathrm{norm}}}, \tag{3}$$

where J_p is the peak current, ε_i are the transverse emittances, and the subscript “norm” indicates normalized values. As an upper bound for the transverse emittances, we measure the emission angles α_i and we assume homogeneous emission across the geometrical radius of the emitter ($r = 170$ nm, $r_{\mathrm{rms}} = r/\sqrt{3}$). Note that the effective source size, and therefore the emittance of tip-shaped emitters, can be an order of magnitude smaller because the curved surface induces correlations between the origin and transverse momentum [16,39]. Photoemission at 1932 nm and 40 eV electron energy yields $\alpha_x = 0.16(6)$ rad, $\alpha_y = 0.15(9)$ rad, $\varepsilon_{x,\mathrm{norm}} = 0.20$ nm rad, and $\varepsilon_{y,\mathrm{norm}} = 0.19$ nm rad. Assuming that the emission duration matches the laser pulse duration, we calculate the normalized rms peak brightness of $B_{p,\mathrm{norm}} = 1.2 \times 10^{12}$ A m^{-2} sr^{-1} for one electron per pulse, which is comparable to a femtosecond cold field emitter at 15 electrons per pulse [9]. Because we use the geometrical and not the effective source size, and because we consider currents of one electron per pulse, we consider this peak brightness a lower bound.

The photoemitted current is stable over a timescale of at least half an hour at 256, 512, and 1932 nm with bunch charges of 55, 32, and 0.75 electrons per pulse, respectively (Fig. 5). With a stable 80 MHz Ti:Sa oscillator, the photocurrent is stable over more than 12 h and trillions of pulses. In contrast, the photoemission from an uncoated monocrystalline [310]-oriented tungsten tip decays over time (Fig. 5); a comparable behavior with even stronger decay was observed in a transmission electron microscope ($\hbar\omega = 2.4$ eV, $p = 1 \times 10^{-9}$ Pa [9]). Schottky emitters in scanning electron microscopes ($\hbar\omega = 3.6$ eV with reduced barrier height $\Phi_{\mathrm{eff}} = 1.6$ eV [5], and $\hbar\omega = 4.7$ eV with $\Phi_{\mathrm{eff}} = 2.8$–$3$ eV and $p < 4 \times 10^{-8}$ Pa [10]) show a similar behavior. Hence, nanodiamond-coated tungsten tips are more stable than these emitters: especially at low photon energies. (Working with low photon energies can be advantageous because the field enhancement at the apex [40] in combination with the nonlinearity enhances forward emission.)

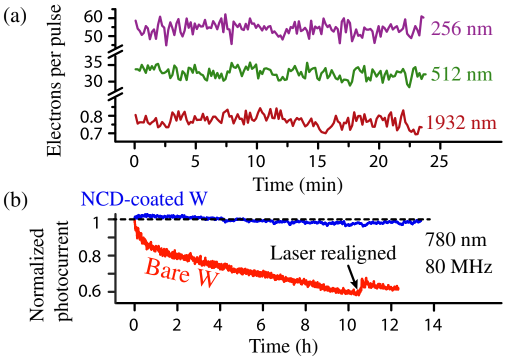

FIG. 5. (a) Photoemission at 1 kHz repetition rate is stable at 256, 512, and 1932 nm from the UV to the infrared, both below and above one electron per pulse. The noise is caused by laser power and pointing fluctuations. (b) Long-term photoemission at 80 MHz and 780 nm is stable from a diamond-coated tungsten tip (blue) and unstable from a bare tungsten tip (red). The short-term fluctuations (over 1 min) from the coated and uncoated tips are 3 and 5%; and the bunch charges at $t = 0$ are 25 and 6.5 electrons per pulse, respectively.

In dc field emission, occasional jumps occur, which is typical for cold field emission. The angular distribution in this emission mode is even smaller as compared to laser-induced emission.

We did not observe a change in laser-induced emission behavior during our experiments, with a laser fluence up to $30\ \mathrm{mJ/cm^2}$ and $3.4 \times 10^{11}\ \mathrm{W/cm^2}$ peak intensity. Hence, we find these as lower bounds of the damage threshold for diamond-coated tungsten tips. With 1932 nm pulses at $3.4 \times 10^{11}\ \mathrm{W/cm^2}$, we have measured 400 electrons per pulse. At these large bunch charges, pulse broadening due to Coulomb repulsion is expected to be severe [10,41], which is why we have focused on smaller bunch charges.

In conclusion, we have presented femtosecond laser-induced electron emission from diamond-coated tungsten tips at 235–350, 512, 780, and 1932 nm. Based on the involved junctions between tungsten, diamond, and the graphitic grain boundaries, we have proposed an emission model that explains our experimental data well. Individual emission channels can be selected by proper choice of laser intensity and wavelength. These channels are identified by the number of photons needed to emit an electron. Stable photoelectron current and the high brightness of the emitted electrons are encouraging to further investigate diamond-coated tungsten tips as an ultrafast electron source.

Before resubmission of this Letter, we became aware of new and related work [42].

The authors acknowledge Mingjian Wu and Erdmann Spiecker for the transmission electron micrograph. They also acknowledge funding from the Deutsche Forschungsgemeinschaft via Grant No. SFB 953 titled “Synthetic Carbon Allotropes,” from the European Research Council through the grant titled “Near Field Atto,” and the Gordon and Betty Moore Foundation via Grant No. GBMF4744 titled “Accelerator on a Chip International Program-ACHIP.”

[*] alexander.tafel@fau.de

[1] J. C. H. Spence, *High-Resolution Electron Microscopy*, 4th ed. (Oxford University, New York, 2013).
[2] O. Bostanjoglo, R. Elschner, Z. Mao, T. Nink, and M. Weingärtner, Ultramicroscopy **81**, 141 (2000).
[3] A. H. Zewail, Science **328**, 187 (2010).
[4] A. Arbouet, G. M. Caruso, and F. Houdellier, in *Advances in Imaging and Electron Physics* (Elsevier, New York, 2018), pp. 1–72.
[5] D.-S. Yang, O. F. Mohammed, and A. H. Zewail, Proc. Natl. Acad. Sci. U.S.A. **107**, 14993 (2010).
[6] D. A. Plemmons, P. K. Suri, and D. J. Flannigan, Chem. Mater. **27**, 3178 (2015).
[7] J. Sun, V. A. Melnikov, J. I. Khan, and O. F. Mohammed, J. Phys. Chem. Lett. **6**, 3884 (2015).
[8] A. Feist, N. Bach, N. R. da Silva, T. Danz, M. Möller, K. E. Priebe, T. Domröse, J. G. Gatzmann, S. Rost, J. Schauss, S. Strauch, R. Bormann, M. Sivis, S. Schäfer, and C. Ropers, Ultramicroscopy **176**, 63 (2017).
[9] F. Houdellier, G. Caruso, S. Weber, M. Kociak, and A. Arbouet, Ultramicroscopy **186**, 128 (2018).
[10] M. Kozák, J. McNeur, N. Schönenberger, J. Illmer, A. Li, A. Tafel, P. Yousefi, T. Eckstein, and P. Hommelhoff, J. Appl. Phys. **124**, 023104 (2018).
[11] P. Hommelhoff, Y. Sortais, A. Aghajani-Talesh, and M. A. Kasevich, Phys. Rev. Lett. **96**, 077401 (2006).
[12] P. Hommelhoff, C. Kealhofer, and M. A. Kasevich, Phys. Rev. Lett. **97**, 247402 (2006).
[13] B. Barwick, C. Corder, J. Strohaber, N. Chandler-Smith, C. Uiterwaal, and H. Batelaan, New J. Phys. **9**, 142 (2007).
[14] M. Krüger, M. Schenk, and P. Hommelhoff, Nature (London) **475**, 78 (2011).
[15] M. Bionta, B. Chalopin, J. Champeaux, S. Faure, A. Masseboeuf, P. Moretto-Capelle, and B. Chatel, J. Mod. Opt. **61**, 833 (2014).
[16] S. Meier, T. Higuchi, M. Nutz, A. Högele, and P. Hommelhoff, Appl. Phys. Lett. **113**, 143101 (2018).
[17] C. Ropers, D. R. Solli, C. P. Schulz, C. Lienau, and T. Elsaesser, Phys. Rev. Lett. **98**, 043907 (2007).
[18] R. Bormann, M. Gulde, A. Weismann, S. V. Yalunin, and C. Ropers, Phys. Rev. Lett. **105**, 147601 (2010).
[19] L. Wimmer, G. Herink, D. R. Solli, S. V. Yalunin, K. E. Echternkamp, and C. Ropers, Nat. Phys. **10**, 432 (2014).
[20] M. R. Bionta, S. J. Weber, I. Blum, J. Mauchain, B. Chatel, and B. Chalopin, New J. Phys. **18**, 103010 (2016).
[21] C. Kealhofer, S. M. Foreman, S. Gerlich, and M. A. Kasevich, Phys. Rev. B **86**, 035405 (2012).
[22] M. Bionta, B. Chalopin, A. Masseboeuf, and B. Chatel, Ultramicroscopy **159**, 152 (2015).
[23] C. Li, X. Zhou, F. Zhai, Z. Li, F. Yao, R. Qiao, K. Chen, M. T. Cole, D. Yu, Z. Sun, K. Liu, and Q. Dai, Adv. Mater. **29**, 1701580 (2017).

[24] V. Porshyn, V. I. Kleshch, E. A. Obraztsova, A. L. Chuvilin, D. Lützenkirchen-Hecht, and A. N. Obraztsov, Appl. Phys. Lett. **110**, 182101 (2017).

[25] J. B. Cui, M. Stammler, J. Ristein, and L. Ley, J. Appl. Phys. **88**, 3667 (2000).

[26] F. J. Himpsel, J. A. Knapp, J. A. VanVechten, and D. E. Eastman, Phys. Rev. B **20**, 624 (1979).

[27] J. B. Cui, J. Ristein, and L. Ley, Phys. Rev. B **60**, 16135 (1999).

[28] F. Maier, J. Ristein, and L. Ley, Phys. Rev. B **64**, 165411 (2001).

[29] J. B. Cui, J. Ristein, and L. Ley, Phys. Rev. Lett. **81**, 429 (1998).

[30] C. F. Davidson, G. B. Alexander, and M. E. Wadsworth, Metall. Mater. Trans. B **9**, 553 (1978).

[31] A. Tafel, M. Wu, E. Spiecker, P. Hommelhoff, and J. Ristein, Diam. Relat. Mater. **97**, 107446 (2019).

[32] J. B. Cui, J. Ristein, and L. Ley, Phys. Rev. B **59**, 5847 (1999).

[33] H. Shiomi, H. Nakahata, T. Imai, Y. Nishibayashi, and N. Fujimori, Jpn. J. Appl. Phys. **28**, 758 (1989).

[34] R. F. Willis, B. Fitton, and G. S. Painter, Phys. Rev. B **9**, 1926 (1974).

[35] J. Cui, J. Ristein, M. Stammler, K. Janischowsky, G. Kleber, and L. Ley, Diam. Relat. Mater. **9**, 1143 (2000).

[36] P. Dean, E. Lightowlers, and D. Wight, Phys. Rev. **140**, A352 (1965).

[37] F. Giustino, S. G. Louie, and M. L. Cohen, Phys. Rev. Lett. **105**, 265501 (2010).

[38] S. Logothetidis, J. Petalas, H. M. Polatoglou, and D. Fuchs, Phys. Rev. B **46**, 4483 (1992).

[39] D. Ehberger, J. Hammer, M. Eisele, M. Krüger, J. Noe, A. Högele, and P. Hommelhoff, Phys. Rev. Lett. **114**, 227601 (2015).

[40] S. Thomas, G. Wachter, C. Lemell, J. Burgdörfer, and P. Hommelhoff, New J. Phys. **17**, 063010 (2015).

[41] B. Cook and P. Kruit, Appl. Phys. Lett. **109**, 151901 (2016).

[42] M. Borz, M. H. Mammez, I. Blum, J. Houard, G. D. Costa, F. Delaroche, S. Idlahcen, A. Haboucha, A. Hideur, V. I. Kleshch, A. N. Obraztsov, and A. Vella, Nanoscale **11**, 6852 (2019).

Author contribution for publication

"Determination of 3D electrostatic field at an electron nano-emitter"

Authors: M. Wu, A. Tafel, P. Hommelhoff, E. Spiecker

Applied Physics letters 114, 013101, **2019**

Co-Author's contributions:

- Writing of the manuscript
- Sample preparation
- Conducting experiments
- Developing the algorithm for analysis
- Analyzing the results
- Running simulations

A. Tafel's contributions:

- Support in writing of the manuscript
- Sample preparation
- Setting up and validating the simulation
- Running simulations
- Developing an alternative analysis

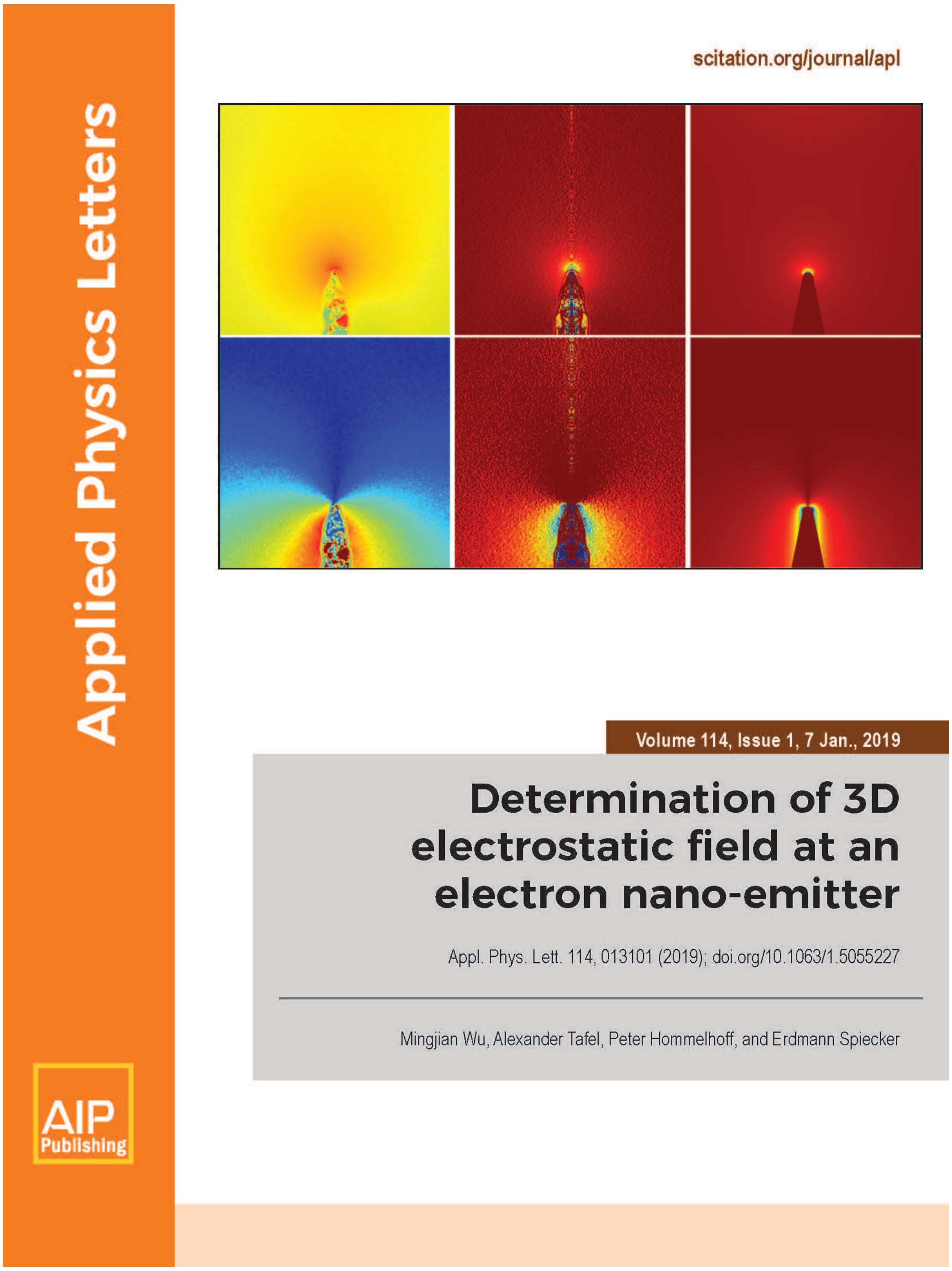

Applied Physics Letters

scitation.org/journal/apl

Volume 114, Issue 1, 7 Jan., 2019

Determination of 3D electrostatic field at an electron nano-emitter

Appl. Phys. Lett. 114, 013101 (2019); doi.org/10.1063/1.5055227

Mingjian Wu, Alexander Tafel, Peter Hommelhoff, and Erdmann Spiecker

AIP Publishing

Figure 5.1: Cover image of Applied Physics Letters Volume 114, Issue 1, in which the following publication 5.3 was published.

Applied Physics Letters

Determination of 3D electrostatic field at an electron nano-emitter

Cite as: Appl. Phys. Lett. **114**, 013101 (2019); https://doi.org/10.1063/1.5055227
Submitted: 06 September 2018 . Accepted: 12 November 2018 . Published Online: 02 January 2019

Mingjian Wu, Alexander Tafel, Peter Hommelhoff, and Erdmann Spiecker

COLLECTIONS

F This paper was selected as Featured

View Online Export Citation CrossMark

ARTICLES YOU MAY BE INTERESTED IN

Squeezing-enhanced rotating-angle measurement beyond the quantum limit
Applied Physics Letters **113**, 261103 (2018); https://doi.org/10.1063/1.5066028

Detection of nonmagnetic metal thin film using magnetic force microscopy
Applied Physics Letters **113**, 261601 (2018); https://doi.org/10.1063/1.5079763

Thermally activated, light-induced electron-spin-resonance spin density reflected by photocurrents in a perovskite solar cell
Applied Physics Letters **114**, 013903 (2019); https://doi.org/10.1063/1.5053830

MMR TECHNOLOGIES
THE WORLD'S RESOURCE FOR
VARIABLE TEMPERATURE
SOLID STATE CHARACTERIZATION
WWW.MMR-TECH.COM
OPTICAL STUDIES SYSTEMS
SEEBECK STUDIES SYSTEMS
MICROPROBE STATIONS
HALL EFFECT STUDY SYSTEMS AND MAGNETS

AIP Publishing

© 2019 Author(s).

Applied Physics Letters ARTICLE scitation.org/journal/apl

Determination of 3D electrostatic field at an electron nano-emitter

Cite as: Appl. Phys. Lett. **114**, 013101 (2019); doi: 10.1063/1.5055227
Submitted: 06 September 2018 · Accepted: 12 November 2018 · Published Online: 02 January 2019

Mingjian Wu,[1,a)] Alexander Tafel,[2] Peter Hommelhoff,[2] and Erdmann Spiecker[1,a)]

AFFILIATIONS

[1] Institute of Micro- and Nanostructure Research and Center for Nanoanalysis and Electron Microscopy (CENEM), Department of Materials Science, Universität Erlangen-Nürnberg, Cauerstraße 6, D-91058 Erlangen, Germany
[2] Chair of Laser Physics, Department of Physics, Universität Erlangen-Nürnberg, Staudtstraße 1, D-91058 Erlangen, Germany

ABSTRACT

Differential phase contrast in scanning transmission electron microscopy has been applied to image nanoscale electrostatic fields of a sharp tungsten electron emitter with an apex radius of about 20 nm and under field emission conditions. Assuming axial symmetry of the nano-emitter, we derived a method based on the inverse Abel transform to quantitatively reconstruct an axial slice of the 3D electrostatic field from a single projection measurement. The highest field strength of 2.92 V/nm is measured at the nano-emitter apex under the condition of a bias voltage of -140 V with respect to the grounded counter electrode located at about 650 nm from the apex, resulting in an emission current of more than 2 μA. The experimental results are compared with simulations based on a finite element numerical Maxwell equation solver. Quantitative agreement between experiment and simulation has been achieved.

Published under license by AIP Publishing. https://doi.org/10.1063/1.5055227

Revealing and quantifying the 3-dimensional (3D) electrostatic field at nanometer resolution around sharp tips has found great interest in the community of electron field emission (FE) and atom probe tomography (APT). In the case of FE, it is the key to answer the fundamental question of how the field interacts with the sharp tips, which has not yet been adequately addressed despite its long history.[1] For this purpose, the local electrostatic field around the apex of metal emitter tips has to be accurately measured at a nanometer scale, while the emission current (density) is simultaneously logged. In the case of APT, the knowledge of electrostatic field topography around the tip apex may form the basis of an aberration correction scheme for APT.[2] The electrostatic field in both FE and APT is usually very strong around the apex and extends to large distances, thus requiring techniques that are able to deliver the resolution and a large field of view (FOV). For this purpose, off-axis electron holography (EH) has been applied to similar studies of field emission tips qualitatively[3–6] and a few quantitative studies have been reported.[4,5] Despite the high sensitivity of EH to measure phase shifts, studying strong and extended electrostatic fields locally and quantitatively with EH is quite challenging due to the limits of the setup. First, the strong and extended field at field emission tips can cause the distortion of the reference wave, which is utilized to form the interference fringes. Therefore, quantification of the local field requires iterative modeling which is usually problem specific. Furthermore, the extremely high field at the tip may not be measurable if the gradient of the phase shift exceeds 2π/pixel when recorded with digital cameras.[7] Alternatively, in-line holography was also proposed for such studies, but also facing considerable challenges including calibration issues, necessity of modeling and simulation, etc.[3]

Here, we determine the 3D electrostatic field at an electron nano-emitter during *in situ* biasing the tip to field emission conditions. The (projected) field is determined by accurate measurement of the electron beam deflection via differential phase contrast in scanning transmission electron microscopy (DPC-STEM). Assuming axial symmetry, we show that the axial slice of the electrostatic field can be retrieved with an algorithm based on the inverse Abel transform, and quantitative agreement with simulation can be achieved.

The tungsten nano-emitter is prepared by standard electro-chemical etching followed by plasma etching in an

---

[a)] Authors to whom correspondence should be addressed: mingjian.wu@fau.de and erdmann.spiecker@fau.de ultra-high vacuum chamber. The *in situ* manipulation and biasing are realized with a Nanofactory STM-TEM holder. A gold rod (electro-chemically etched) is inserted into the fixed side and grounded, while the W nano-emitter is installed on top of the piezo-tube [movable side, cf. Fig. 1(a)]. The axis between them is carefully aligned, so their distance can be measured directly from images. The I–V curve is always logged during ramping up and down of voltages (typically 1–2 s), while the DPC experiments were performed at a constant bias voltage [Fig. 1(b)]. A typical I–V curve and the emission current during the DPC measurement (inset) are shown in Fig. 1(c).

The DPC experiments were performed on a ThermoFischer Scientific Titan Themis[3] 300 electron microscope, operating at 200 kV in micro-probe STEM mode. The vacuum in the column is typically 2×10^{-7} mbar. One of the annular detectors (DF4) is quadrant segmented (referred to as the DPC detector hereafter), which is used to acquire the four quadrant images via Velox software. A typical probe beam current between 150 and 250 pA and a pixel dwell time of 20–30 μs (thus, 25–35 s for the 1024 pixel square frame) is used. Data conversion, processing, and visualization are realized with Python and Gatan DigitalMicrograph scripts.

The DPC signal is calculated by the intensity differences $I_{\mathrm{A-C}}$ and $I_{\mathrm{B-D}}$ of the opposing quadrants [cf. Fig. 1(d)] and is then normalized to the local sum intensity $I_{\mathrm{A+B+C+D}}$

$$\mathbf{S}_{\mathrm{DPC}}(x,y) = \frac{I_{\mathrm{A-C}}(x,y)\hat{e}_{x'} + I_{\mathrm{B-D}}(x,y)\hat{e}_{y'}}{I_{\mathrm{A+B+C+D}}(x,y)}, \tag{1}$$

in which $\hat{e}_{x'}$ and $\hat{e}_{y'}$ denote the unit vectors in the $x' - y'$ plane, where the base axis is defined by the orientation of the installed detector quadrants. Whereas at the sample, the plane x–y depends on how the sample is inserted and can be arbitrary (due to the possible scan rotation applied). Their relative rotation about the commonly defined z-axis and the possible in-plane flip is carefully calibrated and corrected. A vacuum frame under identical conditions as the experimental one is acquired for the correction of the scan artifacts, so that the corrected DPC signal is

$$\mathbf{S}^{\mathrm{corr}}_{\mathrm{DPC}}(x,y) = \mathbf{S}^{\mathrm{raw}}_{\mathrm{DPC}}(x,y) - \mathbf{S}^{\mathrm{ref}}_{\mathrm{DPC}}(x,y). \tag{2}$$

The beam convergence half-angle $\alpha = 4$ mrad and the beam disk (area) coverage of about 60% on the annual DPC detector were applied. This is considered to be a compromised condition to measure strong fields (in our case expected to result in deflections up to about 3 mrad) while keeping the DPC signal in the linear region of calibration. We also have to balance the large FOV, where a scan pivot point problem may arise, and sensitivity (which favors small detector coverage). The deflection angle can be converted from the DPC signal by $\boldsymbol{\beta}(x,y) = k \cdot \mathbf{S}^{\mathrm{corr}}_{\mathrm{DPC}}(x,y)$. The calibration factor k is obtained with the procedure as described in our previous study.[8]

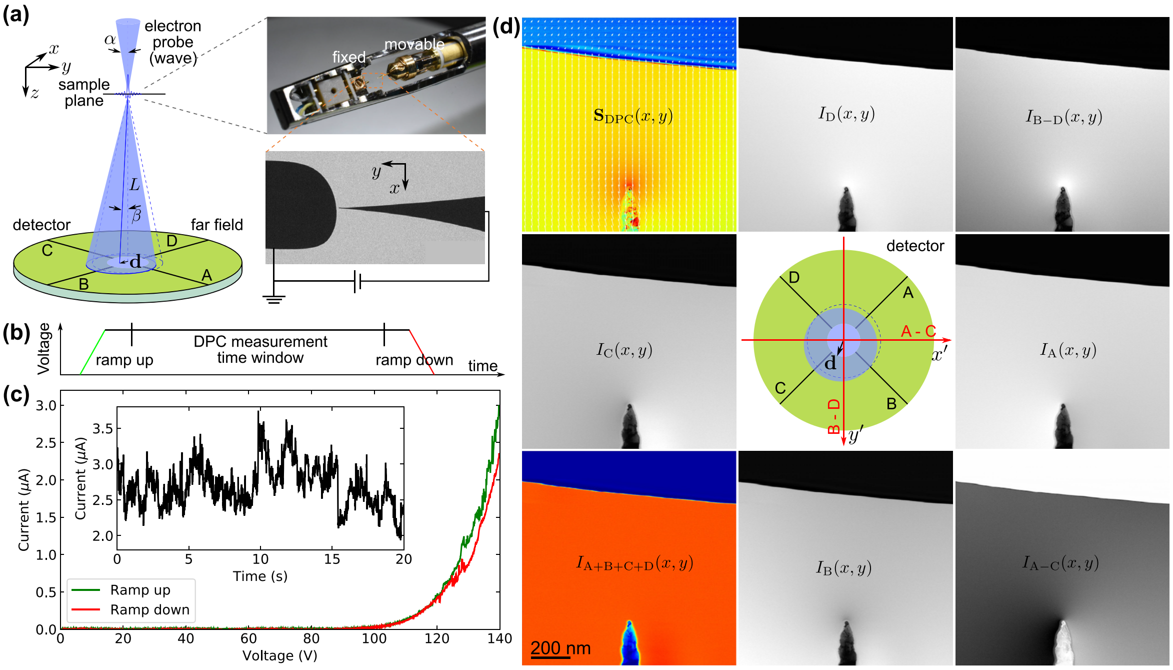
(a)
electron probe (wave)
α
x
y
z
sample plane
fixed
movable
y
x
L
β
detector
far field
C
D
B
A
d
(b)
Voltage
ramp up
DPC measurement time window
ramp down
time
(c)
Current (μA)
3.0
2.5
2.0
1.5
1.0
0.5
0.0
0
20
40
60
80
100
120
140
Voltage (V)
Current (μA)
3.5
3.0
2.5
2.0
0
5
10
15
20
Time (s)
Ramp up
Ramp down
(d)
$\mathbf{S}_{\mathrm{DPC}}(x,y)$
$I_{\mathrm{D}}(x,y)$
$I_{\mathrm{B-D}}(x,y)$
$I_{\mathrm{C}}(x,y)$
detector
D
A
A - C
x'
d
C
B
B - D
y'
$I_{\mathrm{A}}(x,y)$
$I_{\mathrm{A+B+C+D}}(x,y)$
$I_{\mathrm{B}}(x,y)$
$I_{\mathrm{A-C}}(x,y)$
200 nm

FIG. 1. (a) Scheme of the DPC-STEM setup. (b) Voltage-time curve of the DPC experiment. (c) I-V curve showing the field emission and the current-time plot revealing fluctuations of emission current during the DPC measurement (inset). (d) DPC signals and data processing and visualization.

The differential phase shift of electrons passing through a vacuum area (along the defined beam path direction z) with respect to an area of local electrostatic potential $U(x, y, z)$ is

$$d\phi(x,y) = C_E \cdot U(x,y,z)dz, \tag{3}$$

where C_E is the interaction constant, depending only on the corresponding incident electron energy. The differential beam deflection along z at position (x, y) is the in-plane gradient of $d\phi(x, y)$

$$\begin{aligned} d\boldsymbol{\beta}(x,y) &= \frac{\lambda}{2\pi}\nabla_{xy}d\phi(x,y) = \frac{\lambda C_E}{2\pi}\nabla_{xy}U(x,y,z)dz \\ &= C_{E'}\left(\frac{\partial U(x,y,z)}{\partial x}\hat{e}_x + \frac{\partial U(x,y,z)}{\partial y}\hat{e}_y\right)dz. \end{aligned} \tag{4}$$

Here, the reduced interaction constant $C_{E'} = \lambda C_E/2\pi$ has been introduced. For 200 keV electrons used in this study, $C_E = 7.288$ mrad $V^{-1}nm^{-1}$ and $C_{E'} = 2.9092\ \mu$rad V^{-1}. The partial differentials $\partial U/\partial x$ and $\partial U/\partial y$ are the x and y components of the electrostatic field $\mathbf{F}$ at position (x, y, z), i.e., $\mathbf{F}(x,y,z) = F_x(x,y,z)\hat{x} + F_y(x,y,z)\hat{y}$. Therefore, the beam deflection projected along z as measured by the detector at the electron probe position (x, y) is

$$\boldsymbol{\beta}(x,y) = C_{E'}\int_{-\infty}^{\infty}(F_x(x,y,z)\hat{e}_x + F_y(x,y,z)\hat{e}_y)dz. \tag{5}$$

Here, the high-energy assumption is implied and should hold, since the deflection angles are small (0.1–3 mrad). The beam deflection $\boldsymbol{\beta}(x, y)$ is a 2D vector with components

$$\beta_y(x,y) = C_{E'}\int_{-\infty}^{\infty}F_y(x,y,z)dz, \tag{6a}$$

$$\beta_x(x,y) = C_{E'}\int_{-\infty}^{\infty}F_x(x,y,z)dz. \tag{6b}$$

For a sharp tip with a (presumed) circular symmetric axis defined to be coincident with the y-axis and

$$\rho^2 = x^2 + z^2, \quad dz = \frac{\rho d\rho}{\sqrt{\rho^2 - x^2}},$$

the potential function can be reduced: $U(x,y,z) \rightarrow U(\rho,y,\theta)$ with $\partial U/\partial\theta = 0$, and the field can be reduced to

$$\mathbf{F}(x,y,z) \rightarrow \mathbf{F}(\rho,y) = F_\rho(\rho,y)\hat{e}_\rho + F_y(\rho,y)\hat{e}_y.$$

After rearranging, Eq. (6a) becomes (since F_y is even in ρ)

$$\frac{\beta_y(x,y)}{C_{E'}} = \int_{-\infty}^{\infty}F_y(x,y,z)dz = 2\int_x^{\infty}\frac{F_y(\rho,y)}{\sqrt{\rho^2 - x^2}}\rho d\rho, \tag{7}$$

where the right side is the forward Abel transform. Therefore, the local field $F_y(\rho, y)$ can be obtained from the inverse Abel transform of $\beta_y(x,y)/C_{E'}$

$$F_y(\rho,y) = -\frac{1}{\pi C_{E'}}\int_\rho^{\infty}\frac{\partial\beta_y(x,y)}{\partial x}\frac{1}{\sqrt{x^2-\rho^2}}dx. \tag{8}$$

Similarly, the local field component $F_\rho(\rho, y)$ can be obtained from the inverse Abel transform of $\beta_x(x,y)/C_{E'}$

$$F_\rho(\rho,y) = -\frac{1}{\pi C_{E'}}\int_\rho^{\infty}\frac{\partial\beta_x(x,y)}{\partial x}\frac{1}{\sqrt{x^2-\rho^2}}dx. \tag{9}$$

At the slice $z = 0$, one can find that $F_x(\rho, y) = F_\rho(\rho, y)$. Numerical evaluation of Eqs. (8) and (9) involves numerical differentiation and integration. In this study, we applied the Hansen and Law algorithm[9] as implemented in the PyAbel package to obtain the numerical inverse Abel transform. This algorithm works in principle as "onion-peeling" from the outer most pixel and iteratively proceeds until the axial pixel is reached. Therefore, for 2D data, it calculates each axial strip of data [i.e., horizontal lines in Figs. 2(a) and 2(b)] independently. Gaussian filtering with a 3 × 3 kernel was applied to the raw DPC signal before the inverse Abel transform to produce results with much lower noise level.

Electrostatic field simulations between the nano-tip and the anode assuming cylindrical symmetry were performed using a finite element method Maxwell equation solver (COMSOL v5.3). The nano-tip is modeled by a cone with 15° tapering angle, a rounded apex with 20 nm radius and a total wire length of 2 mm, which is simplified but based on observations in the experiments. The anode has a defined cone radius of 750 nm, the same tapering angle and the total length as the nano-tip. The tip to anode distance was set to 650 nm, and −140 V potential is applied to the nano-tip side, while the anode is grounded, identical as in the experiment. The potential drop due to the small emission current is negligible and was not implemented in the simulation. Grid size close to the tip (about 1 μm) region is defined to be smaller than 1 nm. The results were exported and plotted similar to experimentally reconstructed data.

The experimentally measured electron beam deflection maps, calibrated and dissociated into axial and radial components, are shown in Figs. 2(a) and 2(b), respectively. These maps were acquired at a lower sampling rate of 1.1 nm/pixel and 1024 pixels squared in order to cover enough field-of-view for reconstruction; otherwise, the boundary conditions may cause strong artifacts to the field reconstruction. Deflection maps closer to the tip apex acquired immediately after but at a higher sampling rate of 0.27 nm/pixel are shown as insets. The higher beam dose at high magnification has caused the growth of the contamination layer from a few nm to more than 10 nm. Nevertheless, one can clearly observe that the beam deflection (in vacuum) is highly localized at the apex, where the local surface curvature is the highest. The axial component is several times stronger than the radial component, as expected. The "deflection measurement" inside the tip and the electrode does not directly provide the true beam deflection due to the electrostatic field in the materials, but rather a measure of center of mass deflection of the beam, due to the contribution of the mean inner potential of materials, the diffraction contrast, and the dynamic scattering effect.[8,10,11] Therefore, we cannot directly interpret the deflection magnitude inside materials simply as the expected field, and we will restrict our data interpretation to the vacuum region only.

The local electrostatic fields in the two directions, reconstructed according to Eqs. (8) and (9), are presented in Figs. 2(c)–2(f). The center vertical line in the reconstructed maps is the typical artifact of the algorithm applied to noisy data. The triangles close to the counter electrode [Fig. 2(c)–2(f)] are also artifacts, due to inclination of the electrode and therefore

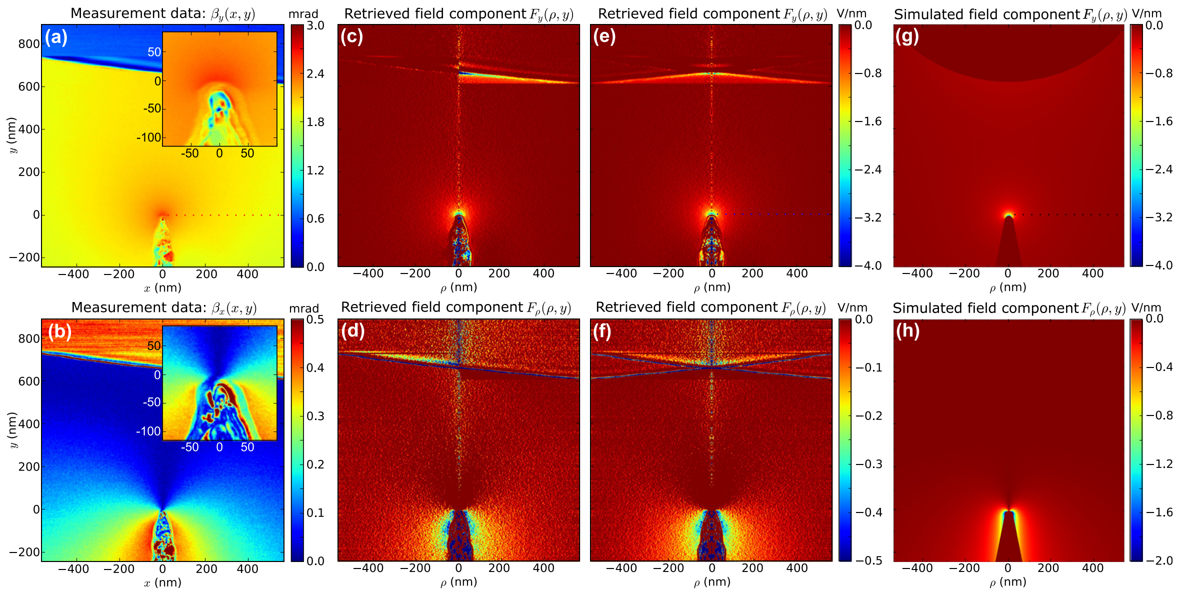
Measurement data: $\beta_y(x,y)$
Retrieved field component $F_y(\rho,y)$
Retrieved field component $F_y(\rho,y)$
Simulated field component $F_y(\rho,y)$
Measurement data: $\beta_x(x,y)$
Retrieved field component $F_\rho(\rho,y)$
Retrieved field component $F_\rho(\rho,y)$
Simulated field component $F_\rho(\rho,y)$

FIG. 2. Experimental beam deflection components (a) $\beta_y(x, y)$ and (b) $\beta_x(x, y)$. The insets are beam deflection components close to the tip region. Reconstructed axial slice of the electrostatic field components $F_y(\rho, y)$ and $F_\rho(\rho, y)$ of the nano-tip at −140 V, directly derived from the deflection maps (c) and (d) and derived after making the deflection maps symmetric (e) and (f). Simulated results of the respective field components $F_y(\rho, y)$ and $F_\rho(\rho, y)$. The center vertical lines in (c)–(f) are reconstruction artifacts. The reconstructed results close to and at the counter electrode are not directly interpretable due to the deviation of symmetry required by the applied reconstruction algorithm. The data points along the color dotted lines as marked in (a), (e), and (g) are plotted in Fig. 3.

deviate from cylindrical symmetry. Whereas Figs. 2(c) and 2(d) were reconstructed directly from the experimental deflection maps, the results in Figs. 2(e) and 2(f) were reconstructed from the symmetrized experimental results. Symmetrization was simply realized by flipping the images horizontally (keeping the tip always aligned in the center) and average with respect to the original images. Under the assumption of axial symmetry, half plane of the data (i.e., on either side of the axis) would be enough to calculate the axial slice of the electrostatic field. This is indeed the case in Figs. 2(c) and 2(d) where the left and right sides of the results were reconstructed from the deflection measure of the respective half planes. Hence, the comparison of the results with and without symmetrization can be regarded as a measure of the quality of the assumption of axial symmetry. Indeed, in the results presented in Fig. 2, the agreement is very good in the vicinity of the tip but deteriorates towards the anode.

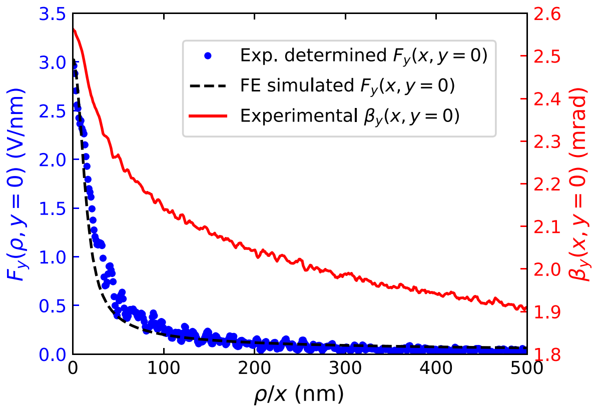

FIG. 3. Line profiles of the measured beam deflection $\beta_y(x, y=0)$ and experimentally derived as well as the simulated field component $F_y(\rho, y=0)$, corresponding to the dashed lines marked in Figs. 2(a), 2(e), and 2(g).

The results of the simulated electrostatic field are presented in Figs. 2(g) and 2(h). One can immediately see that the topology of the field, in both axial and radial components, fits quite well to the experimental results. The field strength of the axial component even matches quantitatively to the experimental one. A radial line of data of the axial field component, starting at the tip and extending to about 500 nm, as marked by the blue and black dashed-lines in Figs. 2(e) and 2(g), respectively, is extracted and plotted in Fig. 3. The highest field strength, normal to the local curvature of the tip is measured to be 2.92 V/nm, and decays rapidly along its radial distance. Both features are very well reproduced in simulation. Nevertheless, the decay speed of the measured field strength close to the tip (<80 nm) seems to be slightly slower than that of the simulated results. This can be attributed to two factors: (1) the geometry of the tip was simplified as a cone in simulation, whereas in experiment, the emitter tip has a local shape that deviates from a cone, and (2) the emitter tip was contaminated and covered by about 3–4 nm carbon at the time when the measurement was conducted. Lastly, we note that the noisiness of the deflection measurements strongly limits the quality of the reconstructed field.

From the application point of view, one may wonder whether there is a simpler way to estimate the strongest field strength from just the highest beam deflection without the inverse Abel transform. This is however not trivial. The measured deflection at the tip apex is a projection integral due to the field topology, i.e., Eq. (5). To obtain the peak field strength from one single projection, even assuming axial symmetry, one has to "peel off" the field contribution on top and bottom (of the axial slice of the tip apex) to the beam deflection by using pixels far enough on the left/right side (in the image). This is the reason why the FOV and sensitivity to weaker fields far away from the tip are equally important for obtaining good quality in the inverse Abel transform. Nevertheless, the characteristic function of the profile (from apex to far enough) of the measured beam deflection carries the quantitative information of the field at the apex [cf. red curve shown in Fig. 3, which is extracted from Fig. 2(a)]. This function depends sensitively on the geometry and the tapering angle of the emission tip.

So far, we have demonstrated quantitative measurements of strong and long-ranged electrostatic fields with high spatial resolution using DPC-STEM. This method has several advantages: First, no reference wave distortion issue occurs (as in off-axis EH); therefore, the results can be interpreted straightforwardly. Second, this technique is able to balance the FOV (set by the scanning area) and the resolution (determined by the probe size and the sampling rate, i.e., pixel size). Finally, it is easy to calibrate the signal.

Besides technology developments in STEM detectors and cameras, there is still room to optimize the parameters of the experimental acquisition.[12] Balanced resolution and detection sensitivity to lower field strength and hence a lower noise level of the reconstruction can be expected. These include the following considerations. With aberration corrected optics, the STEM probe can reach well below an Ångström with a large opening angle ($\alpha > 25$ mrad). Indeed, atomic resolution DPC signals were recorded[13,14] and interpreted after the electron probe has penetrated thin crystal samples.[10,14] Therefore, vacuum electric field measurements at resolution below an Ångström is definitely possible, and interpreting the DPC signals at the interface of the last atomic surface of the tip and vacuum can be expected. In the latter case, the higher order fringes of the point spread function of the probe [cf. blue curve in the electron probe in Fig. 1(a), an example of a probe wave function] has to be considered.[8,11] However, due to the 3D volume of the vacuum field, it is also important to record the weak and extended field, as argued before. In our DPC setup, higher sensitivity favors a smaller beam convergence angle α (typically in similar range as the expected beam deflection angles), a longer camera length L, and a smaller beam coverage on the detector, which may cause non-linearity of the DPC signal with respect to the beam deflection.[12]

Although we have to apply the strong symmetry constrain due to the limited available datasets (single projection measurement), the principle should also work for the study of fields around tips of general shape with tilt series acquisition and tomography algorithms based on Radon transform.[15,16] In this case, a stable and reproducible field emission condition during such tilt series acquisition is necessary. In this respect, the limiting factor is the relatively poor vacuum in the normal TEM column (on the order of 10^{-7} mbar), under which contamination of the tips is hardly avoidable. The contaminates will not only change the work function, but also alter the local curvature, which will cause instability of the emission current [cf. inset in Fig. 1(c)]. These are all crucial parameters to study electron field emission.

In conclusion, we have determined the 3D electrostatic field at a nano-emitter under field emission conditions by DPC-STEM and the inverse Abel transform assuming cylindrical symmetry. At a tip-electrode distance of about 650 nm and −140 V bias voltage, the local field at the tip apex is determined to be 2.92 V/nm. The reconstructed field topology and field strength show almost perfect agreement with simulations.

M.W. and E.S. acknowledge financial support by DFG via research training group GRK 1896 "*In-situ* Microscopy with Electrons, X-rays and Scanning Probes" and usage of instrumentation acquired within the DFG Cluster of Excellence EXC 315 "Engineering of Advanced Materials". A.T. and P.H. acknowledge funding by the ERC grant "Near Field Atto."

REFERENCES

[1] R. G. Forbes and J. H. Deane, Proc. R. Soc. A: Math., Phys. Eng. Sci. **463**, 2907 (2007).
[2] T. F. Kelly, Microsc. Microanal. **23**, 34 (2017).
[3] M. Beleggia, T. Kasama, D. J. Larson, T. F. Kelly, R. E. Dunin-Borkowski, and G. Pozzi, J. Appl. Phys. **116**, 024305 (2014).
[4] J. Cumings, A. Zettl, M. R. McCartney, and J. C. Spence, Phys. Rev. Lett. **88**, 056804 (2002).
[5] L. de Knoop, F. Houdellier, C. Gatel, A. Masseboeuf, M. Monthioux, and M. Hýtch, Micron **63**, 2 (2014).
[6] G. Matteucci, G. F. Missiroli, M. Muccini, and G. Pozzi, Ultramicroscopy **45**, 77 (1992).
[7] N. Verrier and M. Atlan, Appl. Opt. **50**, H136 (2011).
[8] M. Wu and E. Spiecker, Ultramicroscopy **176**, 233 (2017).
[9] E. W. Hansen and P.-L. Law, J. Opt. Soc. Am. A **2**, 510 (1985).
[10] K. Müller, F. Krause, A. Béché, M. Schowalter, V. Galioit, S. Löffler, J. Verbeeck, J. Zweck, P. Schattschneider, and A. Rosenauer, Nat. Commun. **5**, 5653 (2014).
[11] K. Müller-Caspary, F. F. Krause, T. Grieb, S. Löffler, M. Schowalter, A. Béché, V. Galioit, D. Marquardt, J. Zweck, P. Schattschneider, J. Verbeeck, and A. Rosenauer, Ultramicroscopy **178**, 62 (2017).
[12] J. Zweck, F. Schwarzhuber, J. Wild, and V. Galioit, Ultramicroscopy **168**, 53 (2016).
[13] N. Shibata, S. Findlay, Y. Kohno, H. Sawada, Y. Kondo, and Y. Ikuhara, Nat. Phys. **8**, 611 (2012).
[14] N. Shibata, T. Seki, G. Sánchez-Santolino, S. D. Findlay, Y. Kohno, T. Matsumoto, R. Ishikawa, and Y. Ikuhara, Nat. Commun. **8**, 15631 (2017).
[15] P. A. Midgley and R. E. Dunin-Borkowski, Nat. Mater. **8**, 271 (2009).
[16] J. Frank, *Electron Tomography: Methods for Three-Dimensional Visualization of Structures in the Cell* (Springer, 2006).

Published under license by AIP Publishing

Author’s contribution for publication:

“Ultrafast scanning electron microscope applied for studying the interaction between free electrons and optical near-fields of periodic nanostructures”

Authors: M. Kozák, J. McNeur, N. Schönenberger, J. Illmer, A. Li, A. Tafel, P. Yousefi, T. Eckstein and P. Hommelhoff

JOURNAL OF APPLIED PHYSICS 124, 023104, **2018**

Co-Author’s contributions:

- Writing of the manuscript
- Setting up experiments
- Conducting experiments
- Analyzing results
- Conducting simulations

A.Tafels contributions:

- Support in writing of the manuscript
- Support in setting up experiments
- Support in conducting experiments
- Support in analyzing results

Ultrafast scanning electron microscope applied for studying the interaction between free electrons and optical near-fields of periodic nanostructures

M. Kozák, J. McNeur, N. Schönenberger, J. Illmer, A. Li, A. Tafel, P. Yousefi, T. Eckstein, and P. Hommelhoff

Citation: Journal of Applied Physics **124**, 023104 (2018); doi: 10.1063/1.5032093
View online: https://doi.org/10.1063/1.5032093
View Table of Contents: http://aip.scitation.org/toc/jap/124/2
Published by the American Institute of Physics

Articles you may be interested in

On the method of photoconductive detection of defects in semiconductors by vibrational mode-related Fano resonances
Journal of Applied Physics **124**, 025704 (2018); 10.1063/1.5037412

Propagation of THz acoustic wave packets in GaN at room temperature
Applied Physics Letters **112**, 061903 (2018); 10.1063/1.5008852

Thermal conductivity model for nanofiber networks
Journal of Applied Physics **123**, 085103 (2018); 10.1063/1.5008582

Radiation defect dynamics in GaAs studied by pulsed ion beams
Journal of Applied Physics **124**, 025701 (2018); 10.1063/1.5038018

Enhanced collection efficiencies and performance of interband cascade structures for narrow bandgap semiconductor thermophotovoltaic devices
Journal of Applied Physics **124**, 023101 (2018); 10.1063/1.5030904

Mid-wavelength high operating temperature barrier infrared detector and focal plane array
Applied Physics Letters **113**, 021101 (2018); 10.1063/1.5033338

AIP | Journal of Applied Physics SPECIAL TOPICS
LEARN MORE

JOURNAL OF APPLIED PHYSICS **124**, 023104 (2018)

Ultrafast scanning electron microscope applied for studying the interaction between free electrons and optical near-fields of periodic nanostructures

M. Kozák,[1,2,a)] J. McNeur,[1] N. Schönenberger,[1] J. Illmer,[1] A. Li,[1] A. Tafel,[1] P. Yousefi,[1]
T. Eckstein,[1] and P. Hommelhoff[1]
[1]*Department of Physics, Friedrich-Alexander-Universität Erlangen-Nürnberg (FAU), Staudtstrasse 1, 91058 Erlangen, Germany*
[2]*Faculty of Mathematics and Physics, Charles University, Ke Karlovu 3, 12116 Prague 2, Czech Republic*

(Received 2 April 2018; accepted 12 June 2018; published online 13 July 2018)

In this paper, we describe an ultrafast scanning electron microscope setup developed for the research of inelastic scattering of electrons at optical near-fields of periodic dielectric nanostructures. Electron emission from the Schottky cathode is controlled by ultraviolet femtosecond laser pulses. The electron pulse duration at the interaction site is characterized via cross-correlation of the electrons with an infrared laser pulse that excites a synchronous periodic near-field on the surface of a silicon nanostructure. The lower limit of 410 fs is found in the regime of a single electron per pulse. The role of pulse broadening due to Coulomb interaction in multielectron pulses is investigated. The setup is used to demonstrate an increase in the interaction distance between the electrons and the optical near-fields by introducing a pulse-front-tilt to the infrared laser beam. Furthermore, we show the dependence of the final electron spectra on the resonance condition between the phase velocity of the optical near-field and the electron propagation velocity. The resonance is controlled by adjusting the initial electron energy/velocity and by introducing a linear chirp to the structure period allowing the increase of the final electron energy gain up to a demonstrated value of 3.8 keV. *Published by AIP Publishing.* https://doi.org/10.1063/1.5032093

I. INTRODUCTION

Inelastic scattering of electrons by optical near-fields, excited by femtosecond laser pulses in the vicinity of various nanoobjects, has been studied in recent years from different perspectives. The resulting energy modulation imprinted to the electron beam on sub-optical cycle time scales is interesting for various fields of physics. It is considered for electron acceleration,[1–13] for enhancing the visibility of low-contrast nanostructures in photon-induced near-field electron microscopy (PINEM),[14–17] for studying the quantized interactions between light and electrons[18–22] as well as for improving the temporal resolution of ultrafast electron diffraction and microscopy experiments.[20,23–29] This technique can help to overcome the temporal resolution limitations (typically few hundreds of femtoseconds) given by the dispersive broadening of electron pulses during their propagation from the source to the specimen. Achieving sub-optical cycle temporal control of freely propagating electrons by their coherent interaction with light may enable direct access to probing ultrafast coherent electronic dynamics with electrons or the full characterization of optical near-fields of various nanostructures, including phase-resolved spectroscopy.

The interaction between electrons and optical near-fields is based on modifying the dispersion relation of light propagating in vacuum close to an object with refractive index $n > 1$. The phase velocity of the evanescent near-field can be matched to the propagation velocity of an electron near the scattering object, leading to a synchronous interaction between the field and the electron.[6–10,15,16,30] The spatial distribution of the electromagnetic near-fields in the vicinity of a nanostructure can be described using, e.g., Mie scattering theory in the case of a single nanosphere[16] or numerical techniques in the case of more complex nanostructures of various shapes.[9,30] Generally, the near-field amplitude decreases with increasing distance from the object ($\sim 1/r^3$ for a sphere, $\sim e^{-r/\Gamma}$ for periodic structures) on sub-wavelength scales. Hence to maximize the current of electrons interacting with the generated evanescent field, the transverse dimensions of the electron beam have to be smaller than the field decay length (typically $\Gamma = \lambda\beta\gamma/2\pi = 10$–$100\,\mathrm{nm}$, where λ is the light wavelength, β is electron velocity in units of speed of light c, and $\gamma = (1-\beta^2)^{-1/2}$ is the Lorentz factor of electrons). Furthermore, due to the necessity of high field amplitudes allowing reaching measurable electron energy modulation, short laser pulses with durations of fs-ps ($\sim 10^{-15}$–10^{-12} s) are required for the excitation of the near-fields. For the interaction of all generated electrons with the optical near-fields, the duration of the electron pulse has to be comparable to or shorter than the laser pulse duration.

These two requirements, namely, the electron beam that can be focused to a spot with clearly sub-micron-sized transverse dimensions and a pulsed operation with the femtosecond duration of electron pulses, are met in ultrafast electron microscopes, where the electron emission is triggered by ultrashort laser pulses.[31–38] There are several reasons why transmission electron microscopes (TEMs) equipped with field-emission electron sources are considered ideal for this application. They offer a high degree of transverse coherence [coherence length of $\sim 1\,\mu$m (Ref. 37)] and monochromaticity (absolute energy spread of $\Delta E \sim 0.5\,\mathrm{eV}$, resulting in a

---

[a] Author to whom correspondence should be addressed: martin.kozak@fau.de

relative energy spread of $\Delta E/E = 10^{-5}$–10^{-6}) of the electron beam. Further advantages of TEMs are built-in high quality imaging systems and the possibility to acquire images and diffraction patterns in the same measurement setup by adapting the electron imaging optics. The energy resolution of spectrometers used for electron energy-loss spectroscopy (EELS) of ∼0.1 eV further enables spectroscopy of the electrons after their interaction with optical fields and allows resolving quantum coherent features.[14–16,18–21] However, for some applications, the energy acceptance window of these spectrometers, which is typically limited to ∼10 keV, is not sufficient. In experiments focused on electron acceleration by laser fields, the observed energy gains at sub-relativistic electron energies are already approaching several keV[9,10] and higher gains are expected in the future.[8] Furthermore, the specimen chamber in most TEMs has very small dimensions (few millimeters in the electron beam direction). This fact significantly limits the freedom of choice of light coupling geometries and also makes the implementation of experiments with more than one laser beam complicated.

In this paper, we describe the development of an experimental setup based on an ultrafast scanning electron microscope (USEM)[38] equipped with a heated Schottky-type field-emission tip cathode (in the following referred to as Schottky cathode). The setup serves for the research of the inelastic interaction between free electrons and optical near-fields and will be used in the future as a tool for studying different structure geometries and coupling schemes for efficient electron acceleration[9,39–41] and for the implementation of different techniques for transverse and longitudinal manipulation with freely propagating electrons on sub-optical cycle time scales in time-resolved electron imaging and diffraction experiments.[23,29,42] The vacuum chamber of the USEM accommodates both a dielectric nanostructure, where the optical near-fields are generated by femtosecond laser pulses, and a detection setup based on an electromagnetic spectrometer and a microchannel plate (MCP) detector, which allows us to measure the post-interaction electron spectra. The spectra are studied as a function of the time-delay between the pulsed electron beam and the pulsed optical near-fields, the electron initial energy, and/or the parameters of the nanostructure (material, geometry, etc.). This paper is focused on describing the details and capabilities of this new USEM. Furthermore, we show a few examples of applications of this setup. We investigate the temporal broadening of the electron pulses due to repulsive Coulomb interaction between the electrons. Furthermore, we study the role of the resonance condition between the electrons and the synchronous optical near-field mode. Finally, we demonstrate the extension of the interaction length in electron acceleration driven by pulse-front-tilted laser beam at a chirped grating nanostructure.

II. EXPERIMENTAL SETUP

A. Laser source

In the experiment, two synchronized femtosecond laser pulses are used both to temporally control the emission of the electron pulse and to excite the optical near-fields in the interaction region inside the USEM vacuum chamber (see the layout of the experimental setup in Fig. 1). Ultraviolet (UV) laser pulses induce electron photoemission in the USEM electron gun, while infrared (IR) laser pulses excite the optical near-fields on the surface of the nanostructure. The IR pulses are generated in an optical parametric amplifier (OPA) pumped by a Ti:sapphire regenerative amplifier running at a repetition rate of $f_{\mathrm{rep}} = 1$ kHz. The small repetition rate was chosen to achieve high peak powers, which enables increasing the interaction distance between electrons and laser fields in acceleration experiments while keeping the amplitude of the field strength on the order of 10 GV/m. Depending on the wavelength, the pulse duration and the

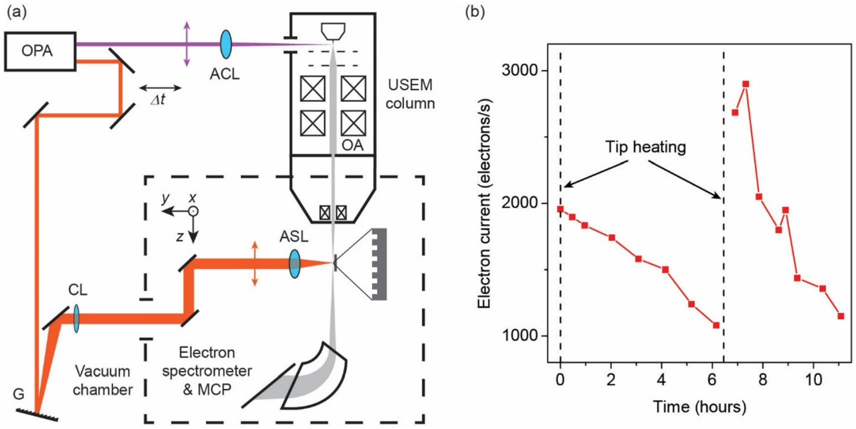

FIG. 1. (a) Layout of the ultrafast scanning electron microscope (USEM) experimental setup. The pulsed UV laser beam (violet) is focused by an achromatic lens (ACL) to the USEM Schottky tip, where the electrons are photoemitted. The electron beam (grey) passes through the objective aperture (OA) and is focused to the interaction region close to the surface of a periodic dielectric nanostructure. The pulsed IR laser beam (red), which is used for optical near-field generation, is delayed by an optical delay line (Δt) and dispersed by a diffraction grating (G), whose surface is imaged by a cylindrical lens (CL) and an aspherical lens (ASL) to the surface of the nanostructure in the USEM vacuum chamber. Electron spectra are measured by an electromagnetic spectrometer and a micro-channel plate detector (MCP). (b) Photoemission electron current as a function of time from tip flashing (heating to ∼1600 K). Excitation photon energy is E_{UV}=4.7 eV, and pulse energy is 12 nJ.

pulse energy of the OPA signal and idler waves are $\tau_{\mathrm{FWHM}} = 50$–$100$ fs and $E_{\mathrm{p}}>100$ μJ. The UV pulses for electron photoemission are generated by sum-frequency mixing the signal wave from the OPA (wavelength of 1100–1600 nm) and part of the basic amplifier output at $\lambda_0 = 800$ nm, and subsequent second harmonic generation. The UV laser beam at a wavelength of $\lambda_{\mathrm{UV}} = 251$–$285$ nm is focused on the USEM Schottky cathode through the vacuum window from a direction perpendicular to the tip symmetry axis with linear polarization parallel to the electron emission direction. The pulse energy is 0.5–30 nJ and the spot radius is $w_{\mathrm{UV}} \approx 6$ μm. The laser beam is aligned to the front facet of the Schottky cathode by heating the tip to high temperature ($T > 1500$ K). The black-body radiation in the visible and infrared is used to align two irises in the beam-path by maximizing the power transmitted through the two apertures using a CCD camera. The UV laser beam is then aligned to these two irises. The fine alignment is done by optimizing the emitted electron current detected by the MCP.

B. Pulsed electron beam

The femtosecond pulsed electron beam is generated by photoemission in a standard SEM (FEI XL 30 FEG) equipped with a Schottky cathode.[43] The cathode consists of a tungsten tip with a flat front facet (100–500 nm in diameter) oriented in the $\langle 100 \rangle$ crystallographic direction. The electrons are emitted by a single-photon process using the UV femtosecond pulses to control the emission time. The height of the surface potential barrier for electrons at the front facet of the cathode [workfunction at the $\langle 100 \rangle$ tungsten surface is $\Phi = 4.6$ eV (Ref. 44)] is lowered to 2.8–3 eV by the Schottky effect due to the applied field strength of 0.8 GV/m and by a layer of ZrO_x which is supplied on the tip front facet when the tip is heated to 1800 K during continuous operation.[43] However, when the tip is kept at room temperature to suppress the DC electron current in the photoemission operation mode, the barrier height is slowly increasing on time scales of several hours [see Fig. 1(b)], probably due to deposition of impurities and adsorbates on the surface and slow removal of ZrO_x by laser illumination. This drop of the electron current is present even for relatively good gun vacuum levels of $p < 4 \times 10^{-10}$ mbar. We found that the increase in the effective barrier height saturates at the value of $\Phi_{\mathrm{eff}} = 4.5$–$5$ eV determined from the photon energy, at which the single-photon photo-emitted current drops to zero after approx. 1 hour of operation. A similar growth of the effective barrier height was previously observed in experiments with optical field emission from tungsten nanotips.[34] To reach single-photon operation with a stable emission current, we typically use the wavelengths of $\lambda_{\mathrm{UV}} = 251$–$285$ nm corresponding to the photon energy of $E_{\mathrm{UV}} = 4.35$–4.95 eV.

The decrease in the electron current with time can be partially suppressed by heating the cathode to a moderate temperature of 1100–1300 K, where the DC current is still negligible but the contamination of the surface is slower due to the elevated temperature. However, this temperature level is still too low to reach diffusion of ZrO_x from the reservoir to the tip apex. Due to this reason, we regularly flash the tip by heating it to temperatures of ~1600 K (similar to Ref. 37). After this procedure, the photoemission current returns back to its original value.

To find out the influence of the laser illumination on the drop of the photoemission current, we measured the current with different time delays after flashing the tip with and without continuous illumination by fs pulses. Here, we observed that the trend of decreasing emission current with time is independent of the illumination but the slope of this decrease $-dI/dt$ growth with laser power. From the results, we anticipate that the illumination plays a significant role only at high power levels. There are two possible reasons for this behavior: 1) The multiphoton ionization of residual gas in the gun leads to production of ions that are attracted by the cathode. When considering the gun pressure, laser repetition rate, and illuminated volume, enough ions can be produced to cover tens of percent of the front facet of the tip after one hour. 2) At high intensities, also the surface geometry of the front facet of the Schottky cathode can change, similar to observations made with a cold field-emission tip.[45] This influences the field enhancement on the surface and thus both the emitted electron current and the spatial distribution of emitted electrons.

After photoemission, the electrons are accelerated by electrostatic fields to the final kinetic energy of $E_{\mathrm{kin}} = 1$–30 keV. The electron beam is focused by the objective lens to the focal plane with a working distance of w_{d}=20 mm reaching a transverse spot size of w_{e}~50–100 nm ($1/e^2$ radius) using a 100 μm diameter objective lens aperture (the objective aperture is shown in Fig. 1). To increase the number of electrons available for the interaction, the condenser lens of the USEM column is set to the highest probe current setting, in which the electron beam is almost perfectly collimated during its propagation through the column (see the calculated electron trajectories in Fig. 5).

C. Optical near-fields, pulse-front-tilt

The optical near-fields used for the interaction with electrons are excited by the IR pulses on the surface of a nonresonant silicon nanograting.[10,23] The spatial distribution of the synchronous spatial harmonics can be described as an evanescent wave exponentially decaying with the distance from the surface and propagating in the direction of the grating k-vector.[13] The cycle-averaged force acting on the electrons during the interaction in the case of nonresonant structures (without resonant enhancement of the near-field amplitude of the synchronous mode) can be written as $F(t,z) \simeq |E(t)| \exp(-\Gamma x) \sin(\omega t)$, where $E(t)$ is the temporal envelope of the driving laser pulse electric field.

The time delay between the UV and IR laser pulses is controlled by a standard optical delay line (0–600 ps, precision of 10 fs), effectively controlling the arrival time of electrons with respect to the optical near-fields. For the light coupling geometry with the laser and electron beams perpendicular to each other,[30] the distance over which the electrons interact with the near-fields is limited by the pulse duration for the flat intensity-front beam. The interaction distance can be significantly increased by using a pulse-front tilted (PFT) laser beam[46,47]

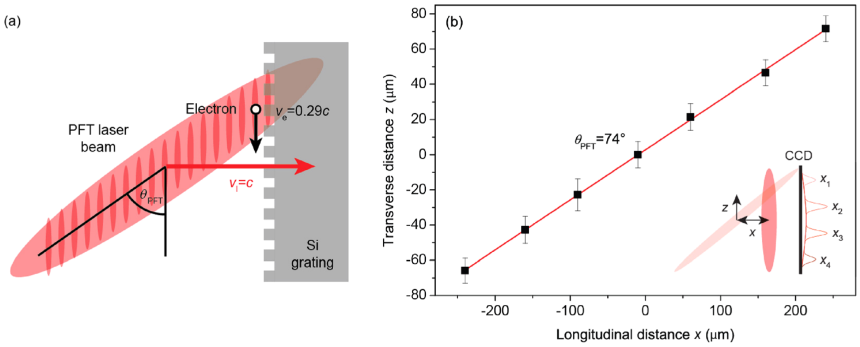

FIG. 2. (a) Layout of the interaction between an electron propagating downwards along the surface of a silicon grating and optical near-fields generated by a pulse-front-tilted IR laser beam propagating horizontally from the left to the right. (b) Measured transverse position (along electron propagation direction *z*) of the peak of the cross-correlation signal between PFT and flat-intensity front laser pulses on the CCD chip as a function of the longitudinal distance between the two pulses (*x*-coordinate in the inset) adjusted by a translation stage. Inset: Sketch of the PFT characterization, where the change in the relative longitudinal distance between the PFT and flat-intensity front pulses leads to the transverse position dependence of the nonlinear detection signal on the CCD chip, labeled as x_i.

[see the sketch of the interaction between the travelling electron and the PFT laser beam in Fig. 2(a)] generated by a dispersive element and the imaging optics shown in Fig. 1(a). While the intensity fronts are tilted, the phase-fronts of such a spatio-temporally modulated beam are still perpendicular to the propagation direction. Therefore, the coupling to the evanescent near-field mode is not affected. In fact, the group velocity of the envelope of the synchronous near-field is matched to its phase velocity. By imaging the surface of the reflective diffraction grating using a cylindrical lens with focal distance of $f_{\mathrm{cyl}} = 70\,\mathrm{cm}$ and the final focusing lens (asphere, $f_{\mathrm{fin}} = 25\,\mathrm{mm}$), an intensity-front angle θ_{PFT} is reached in the interaction region.[48] The magnification of the imaging setup in the dispersion plane determines the angle $\theta_{\mathrm{PFT}}=76°$, which fulfills the relation $\tan(\theta_{\mathrm{PFT}})=\tan(\theta) f_{\mathrm{cyl}}/f_{\mathrm{fin}}$, where $\theta = 8°$ is the diffraction angle of light at wavelength $\lambda = 1.93\,\mu\mathrm{m}$ at the diffraction grating. To avoid spatio-temporal distortions of the laser beam, we use a geometry in which the diffracted beam is perpendicular to the diffraction grating.[49]

The PFT laser beam at a wavelength of $\lambda = 1.93\,\mu\mathrm{m}$ is characterized using cross-correlation with a flat intensity front beam on a silicon-based charge-coupled device (CCD) chip utilizing the two-photon absorption process of the IR pulse [see the sketch of the cross-correlation measurement in the inset of Fig. 2(b)]. The transverse position of the peak of the cross-correlation signal in the electron propagation direction *z* is plotted in Fig. 2(b) as a function of the longitudinal shift of the PFT beam with respect to the flat intensity-front beam. The measured PFT angle $\theta_{\mathrm{PFT}} = 74°$ leads to perfect synchronization of the group velocity of the near-fields with electrons propagating along the grating surface with velocity $v_e = 1/\tan(\theta_{\mathrm{PFT}})c = 0.29c$ (*c* is the speed of light). With the PFT laser beam, the interaction distance is only limited by the transverse laser spot size in the electron propagation direction ($\approx$100 μm) and the electron beam dynamics during the interaction.

D. Electron detection setup

The setup for detection of electron energy spectra after the interaction with optical near-fields consists of a home-built Elbek-type electromagnetic spectrometer[42,50] and a microchannel-plate detector (MCP, Chevron type) with a phosphor screen imaged by a CCD camera [see the layout in Fig. 3(a)]. The spectrometer is designed to offer a large

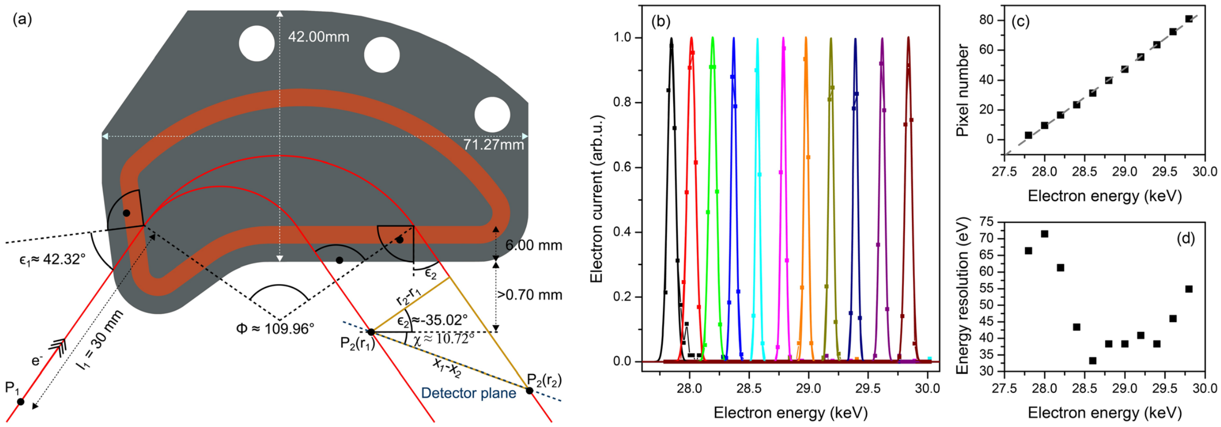

FIG. 3. (a) Layout of the magnetic spectrometer. The point P_1 indicates the position of the input slit (focus of the electron beam). (b) Measured response functions (squares) of the magnetic spectrometer at different electron energies fitted by Gaussian functions (curves). (c) Measured dispersion curve of the spectrometer. (d) Resolution the spectrometer determined from the FWHM of the measured response functions shown in (b).

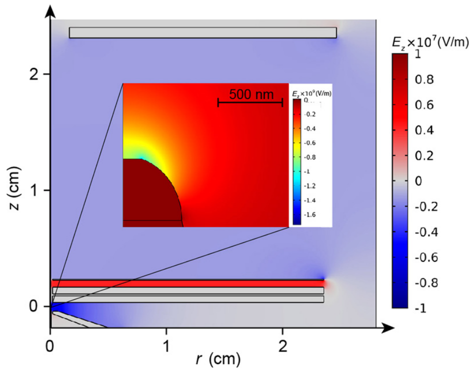

FIG. 4. Geometry of the numerical model of the electron gun with the longitudinal component of the static electric field E_z calculated by COMSOL multiphysics. Displayed electrodes are the suppressor cylinder (lower left corner), extractor and condenser plates, and grounded plate for electron acceleration to the final energy (top). Inset: Details of the distribution of E_z around the tip apex.

energy acceptance window of $\delta E_k = 20$–80 keV and close to the linear dispersion relation. Its performance is verified using a calibration procedure, where the initial electron energy is varied by changing the USEM DC accelerating voltage in the range 27.8–29.6 keV. The dispersion and resolution of the spectrometer are measured [see Figs. 3(b)–3(d)]. The initial energy width of the electron distribution $\Delta E \sim 0.5$ eV is negligible for the resolution measurement. For data acquisition, two modes are available at different experimental conditions. At the low repetition rate of 1 kHz, the electron counting mode is used to suppress the dark noise. Here, the individual peaks in images from the CCD camera with amplitudes above a threshold, which is higher than the noise level, are attributed to single electrons located in the center of mass of each peak and integrated by an acquisition software. Via this procedure, the spectral resolution of <40 eV [see the measured FWHM of the response function in Fig. 3(d)] and the high signal/noise ratio are experimentally reached. This is close to the numerically calculated 20 eV limited by the pixel size of the MCP detector. In this regime, the electron current has to be low enough to allow resolving individual electron density peaks. The background in the measured spectra of 0.001 counts/(s bin) is only caused by the dark count rate of the MCP. At higher electron currents, the second mode is used where the total above-threshold image intensity from the CCD camera is integrated. Here, the spectral resolution is limited to $\sim$100 eV due to the spatial resolution of the MCP phosphor screen.

III. NUMERICAL SIMULATIONS

A virtual model of all active elements within the electron gun head is built in order to solve for the electric field distribution in the gun head. The dimensions for this geometry as well as the applied voltages are taken from the technical drawings of the microscope itself. The Schottky cathode is modeled as a conical tip terminated by a hemispherical apex with a radius of curvature of $r = 470$ nm. To mimic the end facet of the emitter, the cone tip is cut perpendicular to the cone axis such that a flat surface with 300 nm diameter is formed. The static electric fields shown in Fig. 4 are calculated using the electrostatics module of COMSOL multiphysics in two dimensions (all the elements are cylindrically symmetric). The field maps are then revolved around the electron beam axis to yield the fully three-dimensional field distribution.

Electron trajectories (see Fig. 5) are calculated by the 5-th order Runge-Kutta algorithm using the General Particle Tracer (GPT). The initial electron distribution is defined in the following way. The particle coordinates are generated randomly over the end facet of the Schottky cathode, with a two dimensional Gaussian distribution with a FWHM diameter of 300 nm. The initial energy distribution is

$$f(E) = \frac{2\sqrt{\ln 2}}{\sqrt{\pi}\Delta E_0} e^{-4\ln 2\frac{(E-E_0)^2}{\Delta E_0^2}}, \tag{1}$$

where E_0 is the central energy and ΔE_0 is the FWHM energy width. The energy width defines the magnitude of the initial electron velocity. The direction of the velocity is uniformly distributed in the solid angle of 2π out of the tip surface. In the simulations, E_0=0.2 eV and ΔE_0=0.5 eV (typical values for the single-photon photoemission from a Schottky tip[38]). The distribution of the electron emission time corresponds to the envelope of the UV laser pulse (Gaussian, τ_{FWHM}=100 fs). We note that in addition to the electrostatic elements modelled in COMSOL, magnetic elements such as condenser lenses are included in the particle tracing simulations within GPT to accurately model trajectory effects during electron propagation through the microscope column. The Coulomb repulsion between the particles is taken into account to describe the space-charge effects on the final

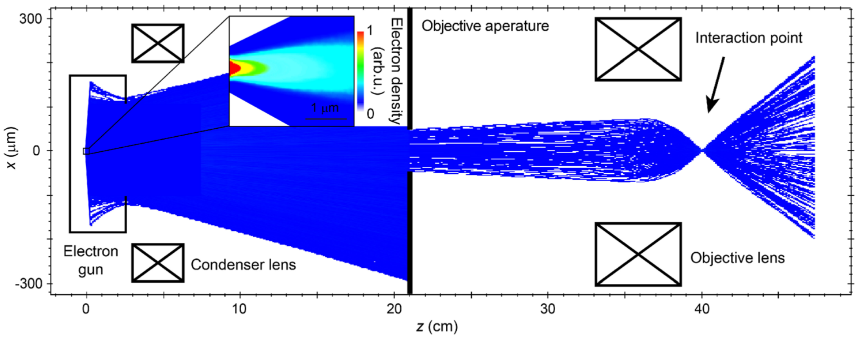

FIG. 5. Electron trajectories calculated by GPT (blue lines). Inset shows the detail of the electron density close to the apex of the Schottky tip (color scale).

pulse duration and transverse dimensions of the probe beam. The position, velocity, energy, and arrival time are evaluated at the interaction point of the experiment located 40 cm downstream from the tip apex.

Each simulation contains a set of $N = 3000$ simulated electrons. For a correct description of statistical effects on the Coulomb interaction for few electrons per pulse, the number of electrons per pulse follows a Poisson distribution:

$$f(N, N_{\mathrm{av}}) = e^{-N_{\mathrm{av}}} \frac{(N_{\mathrm{av}})^N}{N!}, \tag{2}$$

where N_{av} is the average number of electrons per pulse. The bunch duration is evaluated from the Gaussian fit of the histogram of arrival times of all simulated electrons to the interaction point.

IV. RESULTS AND DISCUSSION

In this section, we describe the experimental characterization of the femtosecond pulsed electron beam of the USEM. Furthermore, we show a few examples of measured electron spectra after inelastic scattering of electrons by optical near-fields of silicon nanostructures. To reach efficient energy transfer between the optical near-fields and the electrons, the resonance condition between the phase velocity of the m-th spatial harmonics of the near-field and the propagation velocity β (in units of speed of light c) of the electrons has to be met.[5,7,30,46] This synchronicity condition is fulfilled if $\lambda_{\mathrm{p}}=\beta\lambda m$, where λ_{p} is the period of the structure. During the interaction, a time-periodic sinusoidal modulation of the electron energy is induced. The post-interaction electron energy spectra thus reveal information about the number/density of electrons present at the structure at the same time as the optical near-field pulse. By scanning the relative time delay between the optical pulses generating the near-fields and the electron pulses, the electron pulse duration is measured similar to Refs. 19, 23, and 51. Another option for characterization of the electron pulse duration is to use ponderomotive interaction between the electrons and light.[52–55]

A set of parameters that fully characterize short electron pulses consist of the center energy E_0, an energy spread ΔE arising from the photoemission process and/or Coulomb interactions, the spatial coherence given by the transverse ($\varepsilon_\perp$) and the longitudinal ($\varepsilon_\parallel$) emittances of the beam, duration of the temporal envelope of the pulse, and the total charge.[56] The temporal resolution of experiments with pulsed electron beams is limited by the achievable duration of the pulse envelope (individual pulse envelopes in the case of the attosecond pulse trains[20,26,29,42]) at the studied specimen. There are three main contributions to the final electron pulse duration. The first arises from the short times after photoemission, when the velocity of electrons is small and the relative velocity spread $\Delta v/v$ is high. In the case of flat cathodes, this leads to temporal broadening by $\tau_{acc} \approx (m_0 \Delta E/2)^{1/2}/eE_{acc}$, where E_{acc} is the homogeneous accelerating electrostatic field, m_0 is the electron mass, and ΔE is the initial energy spread.[57–60] However, for tip-based electron sources, the field is strongly inhomogeneous along the electron trajectory. For this case, the acceleration contribution to the electron pulse broadening can be calculated numerically. The arrival time of the on-axis electrons as a function of the initial kinetic energy E_{in} (only longitudinal velocity component assumed) can be written as

$$t = \sqrt{\frac{m_0}{2}} \int_0^d \frac{1}{\sqrt{q(V(0) - V(z)) + E_{\mathrm{in}}}} dz, \tag{3}$$

where $V(z)$ is the potential on the symmetry axis of the electron beam propagating along the z direction. The temporal broadening of the pulse can be approximated as $\tau_{acc} = t(E_{\mathrm{in}} = 0) - t(E_{\mathrm{in}} = \Delta E)$. The potential obtained from the numerical solution of the Laplace equation $\Delta V = 0$ gives the field amplitude on the front facet of the Schottky cathode of 0.8 GV/m. This leads to a temporal broadening of $\tau_{\mathrm{acc}} \approx 30$ fs. The second contribution to the final electron pulse duration is given by the laser pulse duration of $\tau_{\mathrm{laser}} = 100$ fs. The final electron pulse duration (on-axis) can be calculated as $\tau_{electron} \approx \sqrt{\tau_{laser}^2 + \tau_{acc}^2}$. However, because of the relatively large emission angle of the electrons due to the distribution of the electrostatic field on the tip surface, additional broadening of the electron pulse arises from the trajectory effect (see the calculated electron trajectories in Fig. 5), the third contribution. The transverse distribution of electrons along the beam path leads to different lengths of their trajectories between the emission site and the interaction in the chamber. From numerical modelling, we obtained a value of ∼400 fs for the minimum electron pulse duration, which can be obtained in the presented SEM-based setup.

A. Electron pulse duration measurement

The electron pulse duration is measured by acquiring the post-interaction electron spectra as a function of the time delay between the UV laser photoemission pulse and the IR pulse (with PFT) that serves for the near-field generation on the surface of the single silicon grating with a period $\lambda_{\mathrm{p}} = 620$ nm. The electron beam energy in these experiments is 28 keV ($v_{\mathrm{e}} = \beta c = 0.32\ c$) to fulfill the resonance condition. The electron velocity is thus slightly faster than the group velocity of the synchronous mode obtained using the PFT leading to shortening of the interaction distance to ∼50 μm. In Fig. 6(a), the electron spectra are plotted as a function of the time delay between the UV and IR laser pulses. The cross-correlation signal [squares in Fig. 6(b)] is obtained by integrating each electron spectrum out of the spectral window marked by the two dashed lines in Fig. 6(a) (28.27–28.53 keV). Because the nanostructure used to generate the near-fields is nonresonant and because the tilted pulse fronts lead to equal values of the group velocity of both optical near-fields and electrons in the perpendicular coupling geometry, the temporal envelope of the near-fields in the electron rest frame is given by the temporal envelope of the laser pulse. For a sufficiently high energy cut-off and with laser pulses significantly shorter than the electron pulse duration, the cross-correlation signal corresponds to the temporal envelope of the electron pulse $f_{\mathrm{e}}(t)$.[28]

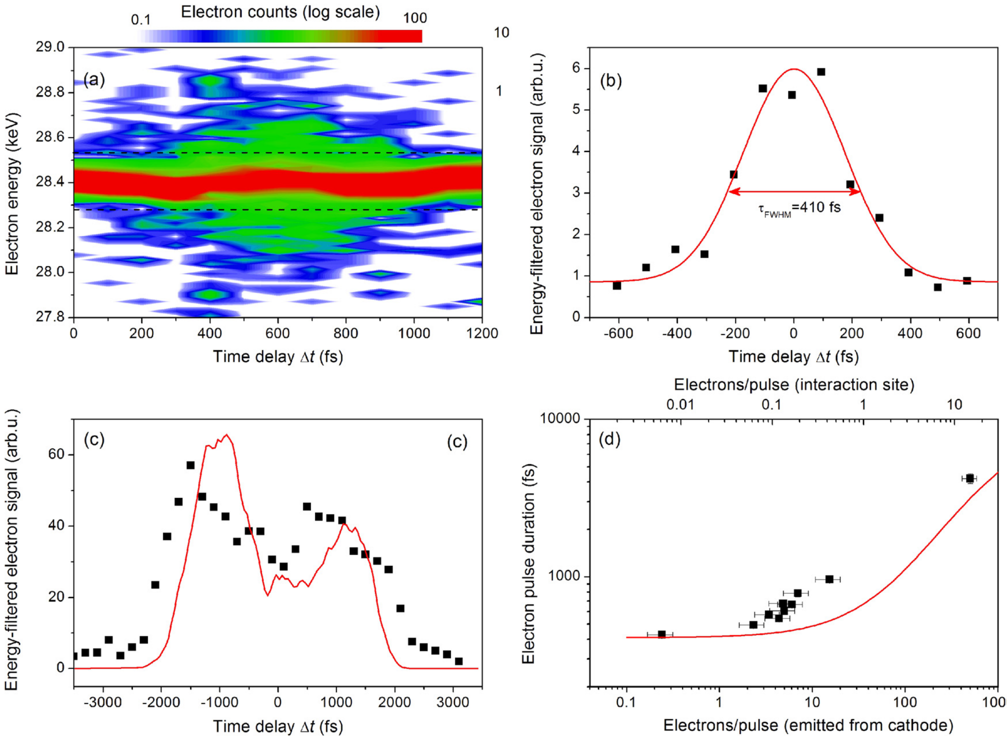

FIG. 6. Electron pulse duration measurements. (a) Electron spectra as a function of the time delay between the electron and laser pulses (in Fig. 1, Δt is varied). (b) Cross-correlation signal obtained from (a) by integrating electrons in each spectrum out of the region of the initial electron energy spectrum marked by the two dashed lines (squares). The data are fitted by a Gaussian function with τ_{FWHM}=410 fs (red curve) with an average charge per pulse emitted from the cathode ~0.2 electrons (0.03 aC). (c) Same as (b), with an average charge per pulse emitted from the cathode of 500 electrons (80 aC). The red curve represents numerical simulation including Coulomb interaction. (d) Measured (squares) and calculated (red curve) electron pulse duration as a function of number of electrons emitted from the cathode per laser pulse (bottom scale) and number of electrons per pulse in the interaction region (upper scale, USEM objective lens aperture with the diameter of 100 μm).

The measured data are fitted with a Gaussian curve with $\tau_{\mathrm{e,FWHM}} = 410 \pm 30$ fs. This corresponds well to the numerical simulations predicting $\tau_{\mathrm{e,FWHM}} = 400$ fs. Such short pulses are only obtained in the regime of <1 electron/pulse emitted from the cathode. We further investigate the dependence of the electron pulse duration on the number of photoemitted electrons during a single laser pulse. For very high pulse charges corresponding to 500 electrons/pulse emitted from the cathode, the temporal envelope of the electron pulse shows a double-peak structure [see Fig. 6(b)] due to the Coulomb repulsion shortly after emission. The two peaks correspond to the front and back parts of the electron pulse that are repelled in the longitudinal direction and accelerated to the final energy. Such a double-peak structure is not observed for pulsed electron beams generated at flat photocathodes.[61] This can be explained by the difference in the current density shortly after photoemission. With 500 electrons per pulse emitted from the front facet of the tip, the maximum density is approximately 50 times higher than the current density with 10^4 electrons per pulse in a typical experiment with a flat photocathode.[61] The Coulomb interaction causes acceleration of the front part and deceleration of the trailing part of the pulse, leading to the observed two peaks of electron density.

Apart from the initial energy spread due to the photoemission process, the electrons in the interaction region have a correlated energy spread due to the spectral broadening shortly after the photoemission and subsequent dispersive propagation. Therefore, also the multi-electron pulses can be in principle compressed back to sub-picosecond durations by RF[62–64] or THz compression techniques.[65]

In Fig. 6(d), we compare the measured pulse duration as a function of electrons/pulse emitted from the cathode (lower scale) and delivered to the chamber (upper scale) with the numerical results. The probe current is limited by the diameter d_{ap}=100 μm of the USEM objective lens aperture and the setting of the condenser lens. The combination of these two parameters effectively sets the transverse emittance ε_t of the probe beam, which needs to be lower than 0.1 nm rad for experiments investigating the interaction between electrons and optical near-fields of periodic nanostructures due to the short transverse decay length of the near-fields. The probe current grows approximately linearly with the area of the objective lens aperture. However, for large aperture diameters, the transverse size of the probe beam in the focus grows significantly (up to ~1 μm with d_{ap}=500 μm) due to aberrations of the electron optics. For experiments with less stringent requirements on the transverse emittance and spot size of the electron beam, currents corresponding to the lower scale in Fig. 6(d) can be used with the objective aperture fully open (d_{ap}>500 μm). Also the pulse duration grows with the aperture size due to the trajectory effects. The electrons propagating further from the symmetry axis have longer trajectories than the on-axis electrons leading to temporal broadening of the pulse. The minimum measured pulse duration with the objective lens aperture fully open is $\tau_{\mathrm{e,FWHM}}=730 \pm 30$ fs.[42]

B. Electron spectra after the interaction with optical near-fields

When the resonance condition is fulfilled, the electrons gain or lose kinetic energy dependent on their injection time with respect to the phase of the optical near-field and on their distance from the surface of the nanostructure.[7,30] The resulting electron spectrum is broadened with exponentially decaying tails [see the spectra with and without laser fields in Fig. 7(a)]. The exponential decay is a consequence of the transverse spatial shape of the accelerating/decelerating fields.[30] The energy gain of an electron interacting with a near-field mode with constant phase velocity in the impulse approximation assuming a small electron velocity change $\Delta v_{\mathrm{e}} \ll v_{\mathrm{e}}$ is given by the integral

$$\Delta E = q \int_{-\infty}^{\infty} E_{\mathrm{long}}^{\mathrm{synch}}(\boldsymbol{r}, t)\mathrm{d}s, \tag{4}$$

where q is the electron charge, $E_{\mathrm{long}}^{\mathrm{synch}}(\boldsymbol{r}, t)$ is the longitudinal component of the electric field of the synchronous harmonic, and ds is the element along the electron trajectory. This approximation, however, is only valid for our experimental parameters when $\Delta E < 0.5$ keV. For higher amplitudes of the velocity modulation ($\Delta v_{\mathrm{e}}/v_{\mathrm{e}}$>1%–3%), the electrons slip over the initial phase of the near-field acting during the interaction and dephasing takes place.[30] This limits the maximum energy gain using periodic nanostructures to approximately 1–3 keV, depending on the interaction distance and the field amplitude applied.[10]

1. *The role of the resonance condition for the interaction between electrons and near-field*

If the resonance condition is exactly fulfilled when the interaction starts and the electron velocity modulation during the interaction is small ($\Delta v_{\mathrm{e}}/v_{\mathrm{e}}$<0.5%), the final electron spectra are symmetric as a consequence of the temporal periodicity of the net force applied to the electrons. This translates to the spatial periodicity in the electron propagation direction. The maximum energy gain and loss before the onset of dephasing are given by Eq. (4). However, when the electrons are initially slower than the optical mode, the spectrum becomes asymmetric due to different phase-matching (resonance) conditions for accelerated and decelerated electrons. In Figs. 7(b) and 7(c), we show the measured (b) and calculated (c) spectra for electrons with different initial velocity β. The phase velocity of the accelerating mode was fixed in all the measurements. The deviation from resonance leads to a difference in the dephasing length and corresponding energy change of the electrons that gain or lose energy. If the electrons are initially slower than the optical mode, the acceleration brings part of the electron distribution to the resonance before dephasing occurs and these can be further accelerated to higher velocities. However, for the decelerated population, the dephasing comes earlier. As a consequence, the beam obtains a net energy gain.

2. *Controlling the resonance condition during the interaction*

To overcome the dephasing and to allow the electrons to be accelerated over longer distances, the phase velocity of the near-field mode has to be controlled during the interaction either by the frequency chirp introduced to the laser pulse or by the chirp of the period of the nanostructure. Because of the limited spectral bandwidth of the laser pulses, we use the second approach. The structure period adiabatically grows along the electron trajectory as $\lambda_{\mathrm{p}} = \lambda_{\mathrm{p0}} + az$,

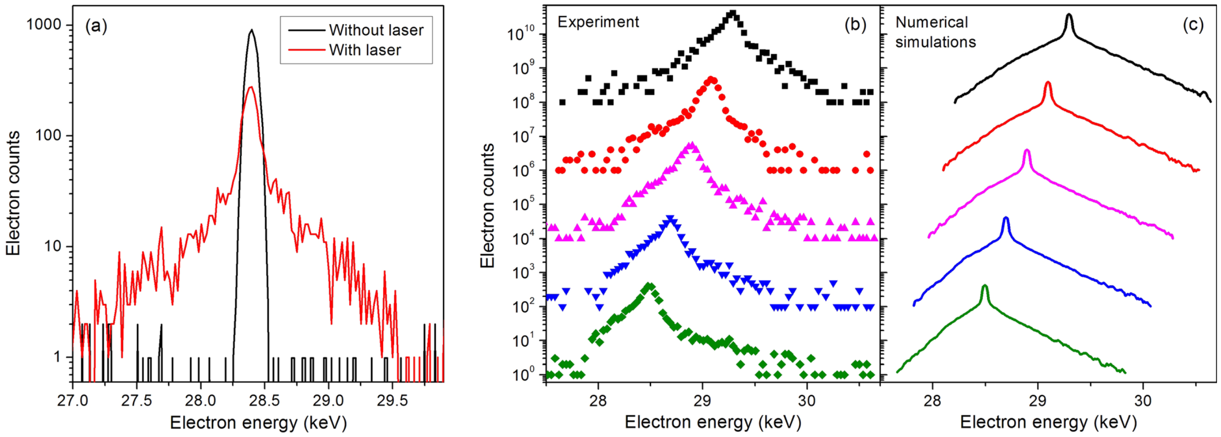

FIG. 7. (a) Electron spectra after passing by the surface of the silicon grating without (black) and with (red) the pulsed laser beam present, exciting the synchronous near-fields. (b) Measured and (c) calculated post-interaction electron spectra for different initial electron energies 28.5–29.3 keV (spectra were vertically shifted for clarity). The resonance condition is met for the black spectra. An initial electron velocity smaller than the synchronous mode phase velocity leads to an asymmetric shape of the spectra as a consequence of different dephasing lengths for accelerated and decelerated electrons.

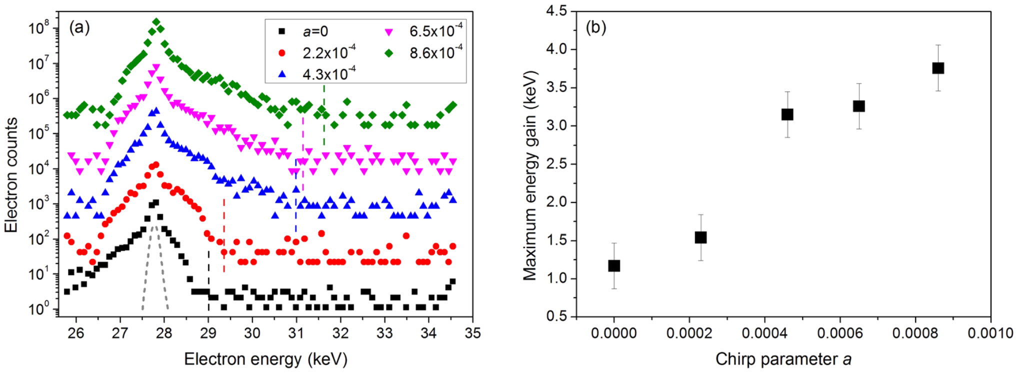

FIG. 8. (a) Measured electron spectra after the interaction with optical near-fields of a linearly chirped grating structure (grating period adiabatically grows as $\lambda_p = \lambda_{p0} + az$) with different values of the linear chirp parameter a. Data are vertically shifted for clarity. (b) Maximum observed energy gain of the electrons as a function of a.

where λ_{p0} is the initial structure period, $a \ll 1$ is the parameter of the linear chirp, and z is the electron propagation direction. In Fig. 8(a), we show the electron spectra after the interaction with the optical near-fields of a chirped single-grating structure as a function of the chirp parameter a. The peak electric field of the laser beam with optimized PFT is measured to be 1.5 GV/m. The maximum measured energy gain as a function of a is shown in Fig. 8(b).

The highest observed energy gain of 3.8 keV is limited by several factors. The first limitation is due to the signal to noise ratio achievable in the presented setup with electron pulses containing less than 1 electron per pulse and the repetition rate of only 1 kHz. The second limiting factor is the sharp dependence of the longitudinal and transverse forces both on the injection phase of the electrons and on their distance from the surface of the nanostructure. Therefore, the amount of electrons that can propagate along the chirped structure with the acceleration exactly matching the phase velocity of the mode decreases exponentially with the travelled distance. In other words, the electron beam experiences a non-uniform growth of both transverse and longitudinal emittance preventing further interaction with the appropriate phase of the optical near-field.

In RF accelerators, for instance, the electrons become relativistic during one field oscillation and then propagate with the velocity close to c. Therefore, the relative changes of both transverse and longitudinal velocities during one period of the accelerating field become very small. However, even with GeV/m gradients reached in dielectric laser accelerators,[66] the energy gain over one grating period for electrons initially at 30 keV is of the order of 1 keV. Therefore, the electrons need to oscillate in the optical near-field many times before they reach relativistic energies. Furthermore, the accelerating mode in a typical RF cavity is cylindrically symmetric allowing the use of focusing elements along the beamline to keep the beam transversally confined. The lack of the transverse spatial symmetry of the accelerating fields makes the electron dynamics of dielectric laser accelerators extremely complicated. For the future success of the particle accelerators driven by optical near-fields, a configuration allowing stable acceleration of electrons trapped in a fraction of the phase space (both longitudinal and transverse) has to be developed.

V. CONCLUSIONS

The experimental setup based on an ultrafast scanning electron microscope was developed for the investigation of the interaction between free electrons and optical near-fields or optical fields in general (see, for example, the inelastic scattering of electrons at a ponderomotive potential of an optical travelling wave described in Ref. 42). Due to its variability, it can also serve for time-resolved electron diffraction and microscopy experiments. The characterization of the pulsed electron beam confirms the possibility of directly (without further compression) reaching femtosecond temporal resolution with this setup with the lower limit for the electron pulse duration of $\tau_{e,\mathrm{FWHM}}$=410 fs. The implementation of the pulse front tilt to the femtosecond pulsed laser beam further allows increasing the interaction distance between the electrons and high-amplitude optical near-fields far beyond the limit for the flat-intensity front beam. We show that by controlling the resonance condition between the propagating electrons and the optical near-fields, the shape of the electron spectra changes. By chirping the structure period, the synchronous interaction for electrons accelerated along the structure is reached leading to the increase in the maximum energy gain to 3.8 keV. Entering the regime of laser-driven electron dynamics brings many challenges for the further development of the dielectric laser accelerators. Reaching transverse and longitudinal beam stability will require the generation of focusing forces based on near-field[10] or ponderomotive interaction.[67] The implementation of these advanced schemes is the next step towards developing a miniaturized electron accelerator driven by optical fields. The USEM presented here will be helpful to provide the well-controlled electron beam with widely varying and well-matching beam parameters.

ACKNOWLEDGMENTS

We thank H. Deng, K. J. Leedle, and J. S. Harris for fabrication a part of the nanostructures used in this study.

The authors acknowledge funding from ERC grant "Near Field Atto," the Gordon and Betty Moore Foundation through Grant GBMF4744 "Accelerator on a Chip International Program – ACHIP" and BMBF via a project with Contract No. 05K16WEC.

[1] J. Rosenzweig, A. Murokh, and C. Pellegrini, Phys. Rev. Lett. **74**, 2467 (1995).

[2] T. Plettner, P. P. Lu, and R. L. Byer, Phys. Rev. Spec. Top.—Accel. Beams **9**, 111301 (2006).

[3] K. Shimoda, Appl. Opt. **1**, 33 (1962).

[4] K. Mizuno, S. Ono, and O. Shimoe, Nature **253**, 184 (1975).

[5] T. Plettner, R. L. Byer, E. Colby, B. Cowan, C. M. S. Sears, J. E. Spencer, and R. H. Siemann, Phys. Rev. Spec. Top.-Accel. Beams **8**, 121301 (2005).

[6] E. A. Peralta, K. Soong, R. J. England, E. R. Colby, Z. Wu, B. Montazeri, C. McGuinness, J. McNeur, K. J. Leedle, D. Walz, E. B. Sozer, B. Cowan, B. Schwartz, G. Travish, and R. L. Byer, Nature **503**, 91 (2013).

[7] J. Breuer and P. Hommelhoff, Phys. Rev. Lett. **111**, 134803 (2013).

[8] R. J. England, R. J. Noble, K. Bane, D. Dowell, C. K. Ng, J. E. Spencer, S. Tantawi, R. L. Byer, E. Peralta, K. Soong, C. M. Chang, B. Montazeri, S. J. Wolf, B. Cowan, J. Dawson, W. Gai, P. Hommelhoff, Y. C. Huang, C. Jing, C. McGuiness, R. B. Palmer, B. Naranjo, J. Rosenzweig, G. Travish, A. Mizrahi, L. Schachter, C. Sears, G. R. Werner, and R. B. Yoder, Rev. Mod. Phys. **86**, 1337 (2014).

[9] K. J. Leedle, A. Ceballos, H. Deng, O. Solgaard, R. F. Pease, R. L. Byer, and J. S. Harris, Opt. Lett. **40**, 4344 (2015).

[10] J. McNeur, M. Kozák, N. Schönenberger, K. J. Leedle, H. Deng, A. Ceballos, H. Hoogland, A. Ruehl, I. Hartl, O. Solgaard, J. S. Harris, R. L. Byer, and P. Hommelhoff, Optica **5**, 687–690 (2018).

[11] M. Kozák, M. Förster, J. McNeur, N. Schönenberger, K. Leedle, H. Deng, J. S. Harris, R. L. Byer, and P. Hommelhoff, Nucl. Instrum. Methods Phys. Res. Sect. A **865**, 84 (2017).

[12] K. J. Leedle, R. Pease, and R. L. Byer, Optica **2**, 158 (2015).

[13] J. Breuer, R. Graf, A. Apolonski, and P. Hommelhoff, Phys. Rev. Spec. Top.—Accel. Beams **17**, 021301 (2014).

[14] B. Barwick, D. J. Flannigan, and A. H. Zewail, Nature **462**, 902 (2009).

[15] F. J. García de Abajo, A. Asenjo-Garcia, and M. Kociak, Nano Lett. **10**, 1859 (2010).

[16] S. T. Park, M. Lin, and A. H. Zewail, New J. Phys. **12**, 123028 (2010).

[17] M. T. Hassan, J. S. Baskin, B. Liao, and A. H. Zewail, Nat. Photonics **11**, 425 (2017).

[18] L. Piazza, T. T. A. Lummen, E. Quiñonez, Y. Murooka, B. W. Reed, B. Barwick, and F. Carbone, Nat. Commun. **6**, 6407 (2015).

[19] A. Feist, K. E. Echternkamp, J. Schauss, S. V. Yalunin, S. Schäfer, and C. Ropers, Nature **521**, 200 (2015).

[20] K. E. Priebe, C. Rathje, S. V. Yalunin, T. Hohage, A. Feist, S. Schäfer, and C. Ropers, Nat. Photonics **11**, 793 (2017).

[21] K. E. Echternkamp, A. Feist, S. Schäfer, and C. Ropers, Nat. Phys. **12**, 1000 (2016).

[22] B. Barwick and A. H. Zewail, ACS Photonics **2**, 1391 (2015).

[23] M. Kozák, J. McNeur, K. J. Leedle, H. Deng, N. Schönenberger, A. Ruehl, I. Hartl, J. S. Harris, R. L. Byer, and P. Hommelhoff, Nat. Commun. **8**, 14342 (2017).

[24] M. T. Hassan, H. Liu, J. S. Baskin, and A. H. Zewail, Proc. Natl. Acad. Sci. U. S. A. **112**, 12944 (2015).

[25] Y. Morimoto and P. Baum, Phys. Rev. A **97**, 033815 (2018).

[26] Y. Morimoto and P. Baum, Nat. Phys. **14**, 252 (2018).

[27] D. J. Flannigan and A. H. Zewail, Acc. Chem. Res. **45**, 1828 (2012).

[28] F. O. Kirchner, A. Gliserin, F. Krausz, and P. Baum, Nat. Photonics **8**, 52 (2014).

[29] M. Kozák, N. Schönenberger, and P. Hommelhoff, Phys. Rev. Lett. **120**, 103203 (2018).

[30] J. Breuer, J. McNeur, and P. Hommelhoff, J. Phys. B: At. Mol. Opt. Phys. **47**, 234004 (2014).

[31] P. Hommelhoff, Y. Sortais, A. Aghajani-Talesh, and M. A. Kasevich, Phys. Rev. Lett. **96**, 077401 (2006).

[32] P. Hommelhoff, C. Kealhofer, and M. A. Kasevich, Phys. Rev. Lett. **97**, 247402 (2006).

[33] B. Barwick, C. Corder, J. Strohaber, N. Chandler-Smith, C. Uiterwaal, and H. Batelaan, New J. Phys. **9**, 142 (2007).

[34] M. Schenk, M. Krüger, and P. Hommelhoff, Phys. Rev. Lett. **105**, 257601 (2010).

[35] R. Bormann, M. Gulde, A. Weismann, S. V. Yalunin, and C. Ropers, Phys. Rev. Lett. **105**, 147601 (2010).

[36] V. A. Lobastov, R. Srinivasan, and A. H. Zewail, Proc. Natl. Acad. Sci. U. S. A. **102**, 7069 (2005).

[37] A. Feist, N. Bach, N. R. da Silva, T. Danz, M. Möller, K. E. Priebe, T. Domröse, J. G. Gatzmann, S. Rost, J. Schauss, S. Strauch, R. Bormann, M. Sivis, S. Schäfer, and C. Ropers, Ultramicroscopy **176**, 63 (2017).

[38] D.-S. Yang, O. F. Mohammed, and A. H. Zewail, Proc. Natl. Acad. Sci. U. S. A. **107**, 14993 (2010).

[39] Z. Wu, R. J. England, C.-K. Ng, B. Cowan, C. McGuinness, C. Lee, M. Qi, and S. Tantawi, Phys. Rev. Spec. Top.—Accel. Beams **17**, 081301 (2014).

[40] H. Deng, J. Jiang, Y. Miao, K. J. Leedle, H. Li, O. Solgaard, R. L. Byer, and J. S. Harris, preprint arXiv:1701.08945 (2017).

[41] M. Kozák, P. Beck, H. Deng, J. McNeur, N. Schönenberger, C. Gaida, F. Stutzki, M. Gebhardt, J. Limpert, A. Ruehl, I. Hartl, O. Solgaard, J. S. Harris, R. L. Byer, and P. Hommelhoff, Opt. Express **25**, 19195 (2017).

[42] M. Kozák, T. Eckstein, N. Schönenberger, and P. Hommelhoff, Nat. Phys. **14**, 121 (2018).

[43] MS. Brongsgeest, "Physics of Schottky electron sources," Ph.D. thesis (Delft University of Technology, 2009).

[44] H. Kawano, Prog. Surf. Sci. **83**, 1 (2008).

[45] G. M. Caruso, F. Houdellier, P. Abeilhou, and A. Arbouet, Appl. Phys. Lett. **111**, 023101 (2017).

[46] T. Plettner and R. L. Byer, Phys. Rev. Spec. Top.—Accel. Beams **11**, 030704 (2008).

[47] D. Cesar, J. Maxson, P. Musumeci, X. Shen, R. J. England, K. P. Wootton, and S. Tan, preprint arXiv:1804.00634v2 (2018).

[48] S. Akturk, X. Gu, E. Zeek, and R. Trebino, Opt. Express **12**, 4399 (2004).

[49] D. Kreier and P. Baum, Opt. Lett. **37**, 2373 (2012).

[50] J. Borggreen, B. Elbek, and L. Perch Nielsen, Nucl. Instrum. Methods **24**, 1 (1963).

[51] M. Kozák, J. McNeur, K. J. Leedle, H. Deng, N. Schönenberger, A. Ruehl, I. Hartl, H. Hoogland, R. Holzwarth, J. S. Harris, R. L. Byer, and P. Hommelhoff, Opt. Lett. **41**, 3435 (2016).

[52] B. J. Siwick, A. A. Green, C. T. Hebeisen, and R. J. D. Miller, Opt. Lett. **30**, 1057–1059 (2005).

[53] C. T. Hebeisen, R. Ernstorfer, M. Harb, T. Dartigalongue, R. E. Jordan, and R. J. D. Miller, Opt. Lett. **31**, 3517–3519 (2006).

[54] C. T. Hebeisen, G. Sciaini, M. Harb, R. Ernstorfer, T. Dartigalongue, S. G. Kruglik, and R. J. D. Miller, Opt. Express **16**, 3334–3341 (2008).

[55] V. R. Morrison, R. P. Chatelain, C. Godbout, and B. J. Siwick, Opt. Express **21**, 21–29 (2013).

[56] P. Baum, Chem. Phys. **423**, 55 (2013).

[57] K. Kinoshita, M. Ito, and Y. Suzuki, Rev. Sci. Instrum. **58**, 932 (1987).

[58] M. Aidelsburger, F. O. Kirchner, F. Krausz, and P. Baum, Proc. Natl. Acad. Sci. U. S. A. **107**, 19714 (2010).

[59] J. Hoffrogge, J. P. Stein, M. Krüger, M. Förster, J. Hammer, D. Ehberger, P. Baum, and P. Hommelhoff, J. Appl. Phys. **115**, 094506 (2014).

[60] A. Paarmann, M. Gulde, M. Müller, S. Schäfer, S. Schweda, M. Maiti, C. Xu, T. Hohage, F. Schenk, C. Ropers, and R. Ernstorfer, J. Appl. Phys. **112**, 113109 (2012).

[61] B. J. Siwick, J. R. Dwyer, R. E. Jordan, and R. J. D. Miller, J. Appl. Phys. **92**, 1643 (2002).

[62] T. van Oudheusden, E. F. de Jong, S. B. van der Geer, W. P. E. M. Op 't Root, O. J. Luiten, and B. J. Siwick, J. Appl. Phys. **102**, 093501 (2007).

[63] T. van Oudheusden, P. L. E. M. Pasmans, S. B. van der Geer, M. J. de Loos, M. J. van der Wiel, and O. J. Luiten, Phys. Rev. Lett. **105**, 264801 (2010).

[64] A. Gliserin, M. Walbran, F. Krausz, and P. Baum, Nat. Commun. **6**, 8723 (2015).

[65] C. Kealhofer, W. Schneider, D. Ehberger, A. Ryabov, F. Krausz, and P. Baum, Science **352**, 429 (2016).

[66] K. P. Wootton, Z. Wu, B. M. Cowan, A. Hanuka, I. V. Makasyuk, E. A. Peralta, K. Soong, R. L. Byer, and R. J. England, Opt. Lett. **41**, 2696 (2016).

[67] B. Naranjo, A. Valloni, S. Putterman, and J. B. Rosenzweig, Phys. Rev. Lett. **109**, 164803 (2012).

Author contribution for publication:

“A miniaturized electron source based on dielectric laser accelerator operation at higher spatial harmonics and a nanotip photoemitter”

Authors: J. McNeur, M. Kozák, D. Ehberger, N. Schönenberger, A. Tafel, A. Li and P. Hommelhoff

Journal of Physics B: Atomic, Molecular and Optical Physics, **2016**

Co-Author’s contributions:

- Writing of the manuscript
- Setting up experiments
- Conducting experiments
- Analyzing results

A.Tafels contributions:

- Support in writing of the manuscript
- Support in setting up experiments
- Support in conducting experiments

Journal of Physics B: Atomic, Molecular and Optical Physics

PAPER

A miniaturized electron source based on dielectric laser accelerator operation at higher spatial harmonics and a nanotip photoemitter

To cite this article: Joshua McNeur *et al* 2016 *J. Phys. B: At. Mol. Opt. Phys.* **49** 034006

View the article online for updates and enhancements.

Related content

- Dielectric laser acceleration of electrons in the vicinity of single and double grating structures—theory and simulations
  John Breuer, Joshua McNeur and Peter Hommelhoff
- Attosecond physics phenomena at nanometric tips
  Michael Krüger, Christoph Lemell, Georg Wachter et al.
- Attosecond physics in photoemission from a metal nanotip
  M Krüger, M Schenk, M Förster et al.

Recent citations

- Divergence study and emittance measurements for the electron beam emitted from a diamond pyramid
  D. Kim *et al*
- Spontaneous and stimulated emissions of a preformed quantum free-electron wave function
  Yiming Pan and Avraham Gover
- Enhanced energy gain in a dielectric laser accelerator using a tilted pulse front laser
  D. Cesar *et al*

IOP | ebooks™

Bringing you innovative digital publishing with leading voices to create your essential collection of books in STEM research.

Start exploring the collection - download the first chapter of every title for free.

This content was downloaded from IP address 131.188.6.12 on 15/11/2019 at 13:16

IOP Publishing Journal of Physics B: Atomic, Molecular and Optical Physics

J. Phys. B: At. Mol. Opt. Phys. **49** (2016) 034006 (7pp) doi:10.1088/0953-4075/49/3/034006

A miniaturized electron source based on dielectric laser accelerator operation at higher spatial harmonics and a nanotip photoemitter

Joshua McNeur[1], **Martin Kozak**[1], **Dominik Ehberger**[1,4], **Norbert Schönenberger**[1], **Alexander Tafel**[1], **Ang Li**[1] **and Peter Hommelhoff**[2,3]

[1] Department of Physics, Friedrich Alexander University Erlangen Nuremberg, Staudtstr. 1, D-91058 Erlangen, Germany
[2] Max-Planck-Institute of Quantum Optics, Hans-Kopfermann-Str. 1, D-85748 Garching, Germany
[3] Max-Planck-Institute for the Science of Light, Günther-Scharowsky-Str. 1, D-91058 Erlangen, Germany

E-mail: joshua.mcneur@fau.de

Received 1 June 2015, revised 28 September 2015
Accepted for publication 20 October 2015
Published 21 January 2016

Abstract

Here we propose a miniaturized electron source driven by recent experimental results of laser-triggered electron emission from tungsten nanotips and dielectric laser acceleration of sub relativistic electrons with velocities as low as 5.7×10^7 m s^{-1} or energies as low as 9.6 keV, less than 20% of the speed of light. The recently observed laser-triggered emission of coherent low-emittance electron pulses from tungsten nanotips naturally lends itself towards incorporation with subrelativistic dielectric laser accelerators (DLAs). These structures have previously been shown to accelerate 28 keV electrons and here we report on the utilization of the 4th and 5th spatial harmonics of near fields in the single grating DLA to achieve acceleration of electrons with kinetic energies of 15.2 and 9.6 keV. We then propose the combination of needle tip emitters with subrelativistic accelerators to form a mm-scale device capable of producing electrons with arbitrary energies.

Keywords: laser-driven electron emission, laser-driven electron acceleration, non-relativistic electron beam, inverse Smith–Purcell effect

(Some figures may appear in colour only in the online journal)

1. Introduction

Dielectric laser acceleration, the acceleration of charged particles by the near fields of optical and NIR lasers traversing micron-scale dielectric structures [1], has previously been shown to impart energy to electrons injected with kinetic energies of 28–100 keV, and 60 MeV [2–4]. The accelerating gradients of these structures have been found to be as high as 300 MeV m^{-1} and are expected to soon exceed 1 GeV m^{-1} [5].

The large field gradients and mm-sized footprint of these structures has motivated a proposed design of a miniaturized electron source that incorporates dielectric laser accelerator (DLA) accelerating sections. However, two challenges have previously stood in the way of realizing such a source. First, in order to miniaturize the design, electrons with energies lower than 28 keV need to be efficiently accelerated by DLAs (so that 28 kV DC accelerating fields and their associated infrastructure do not need to be employed). Second, an appropriate electron source for subrelativistic DLAs needs to

---

[4] Now with Fakultät für Physik, Ludwig-Maximilians-Universität München, Am Coulombwall 1, D-85748 Garching München, Germany.

© 2016 IOP Publishing Ltd Printed in the UK

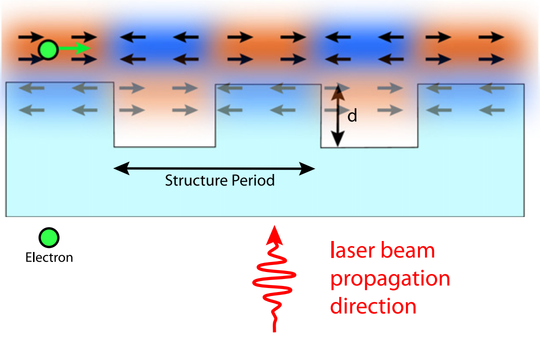

Figure 1. Illustration of two periods of a cross-section of the single grating DLA. A laser pulse incident from below excites near fields with travelling wave modes that can synchronously interact with electrons travelling from left to right above the grating. Here red fields are accelerating and blue fields are decelerating.

be determined. To address the first point, we report here on acceleration of electrons with kinetic energies below 10 keV, permitting the use of a DC injector gun with sub-cm size. State of the art electron guns typically have overall dimensions that are 5 cm or larger, however many of the critical feature sizes in these guns are limited by the breakdown voltage of the metals composing the guns. By operating our proposed electron gun at voltages 3 to 10 times smaller than standard electron gun voltages (30–100 keV), we can reduce these critical feature sizes by a factor of at least three.

To address the second challenge, we note that the typical DLA geometric dimensions place restrictions on potential emitter sources. For instance, in order to traverse the 1 micron tall by 500 micron long acceleration channel in [4] without colliding into the dielectric structure, the accelerated electron beam must have a sub-micron spot size and an emittance below one micron-radian, well below the standard operating conditions of the copper photocathodes in most accelerator facilities. Similar requirements are placed on the emittance of a DLA-appropriate beam if one demands that electrons stay within one transverse decay length of the accelerating fields of the single grating DLA described in [2] and below. Laser-triggered tungsten nano emitters may provide suitable electron beams for DLA operation. We summarize here recent results on the sub-nm emittance, sub-micron spot size electron beams generated by laser triggered emission of tungsten nanotips [6].

Finally, we put forward a preliminary design that incorporates the nanotips with the sub relativistic DLA design to form a miniaturized electron source. We comment on potential applications for such a source and discuss further challenges for improving its efficacy.

2. The single grating DLA as a subrelativistic accelerator

The single grating DLA acts as a phase mask for a laser pulse traversing the structure from below. The diffracted laser pulse generates near fields above the grating that are used to accelerate electrons traveling from left to right in figure 1. Synchronous acceleration occurs if a spatial harmonic of the diffracted near field has a phase velocity matching the traversing electron velocity. This synchronicity condition can be expressed as

$$\beta = \frac{\Lambda}{m\lambda}, \tag{1}$$

where β is the longitudinal speed of the accelerated synchronous electron divided by the speed of light, Λ is the structural periodicity of the single grating, m is the order of the accelerating mode harmonic and λ is the central wavelength of the incident laser pulse. In order to ease the process of miniaturizing a DLA-based electron source, we aim to decrease the velocity of electrons that can be synchronously accelerated. This can be achieved by either decreasing the structural periodicity of the single grating, increasing the order of the harmonic used to accelerate electrons, or increasing the central wavelength of the incident laser source. Decreasing the structural periodicity is limited by fabrication capabilities. Although all approaches are being considered by the authors, we report here specifically on using higher spatial harmonics ($m = 4,\ 5$) to accelerate electrons with kinetic energies much less than 28 keV. We note that all spatial harmonics are excited when the single grating is illuminated. However, only the harmonic which is synchronous with the electron velocity will impart a net acceleration to the electrons. For instance, if a 9.55 keV electron traverses the single grating, it will see a continuous increase in energy due to interaction with the 5th harmonic. Although it will also interact with the fields generated by the fundamental harmonic, it will encounter rapid phase slippage due to the mismatched velocity of the mode and the electron. The electron will see accelerating fields for half of an optical cycle, then decelerating fields the next half optical cycle, resulting in zero net energy gain. Nevertheless, because the amplitude of the non-synchronous lower-order modes are stronger than that for the synchronous 5th order mode, it is important to confirm that acceleration due to interaction with the 5th harmonic is detectable in our setup.

For the fused silica structures tested, the grating periodicity is 750 nm and the depth and width of the grating trench is 280 and 325 nm respectively. This grating period, set by fabrication limits of fused silica, determines the kinetic energy of electrons synchronous with each harmonic. Electrons with a kinetic energy of 15.2 keV are synchronous with the 4th harmonic whereas electrons with a kinetic energy of 9.55 keV are synchronous with the 5th harmonic generated by this structure. The longitudinal electric field profiles of the 3rd–5th harmonics, as computed in a eigenmode field-solver [23], are shown in figure 2. We note two important properties of these field profiles. First, the relative strength of these profiles (generated by a 3 GV m^{-1} incident field) is reduced for higher harmonics. The 4th harmonic has approximately 60% of the maximum field strength of the 3rd harmonic, and the 5th harmonic has approximately 30% the maximum field strength of the 3rd harmonic, corresponding to accelerating

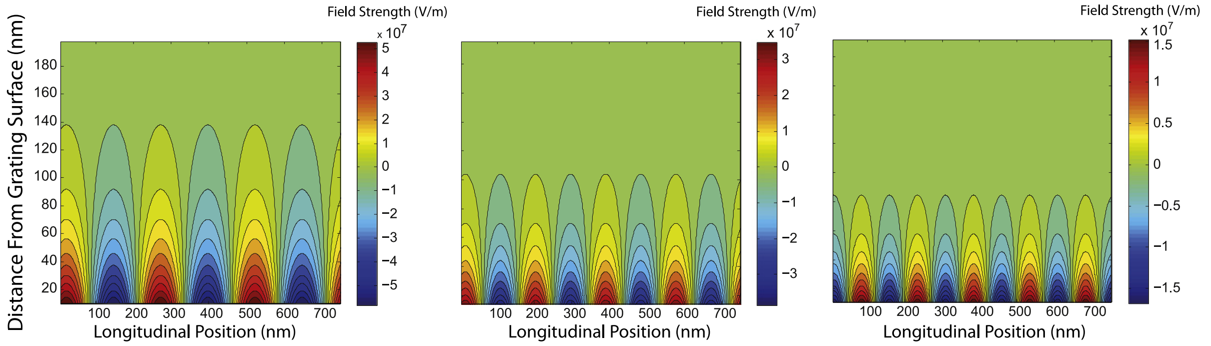

Figure 2. Field profile of the longitudinal component of the electric field directly above one structural period of the single grating DLA for the 3rd harmonic (left), 4th harmonic (center) and 5th harmonic (right). More detail is in the text.

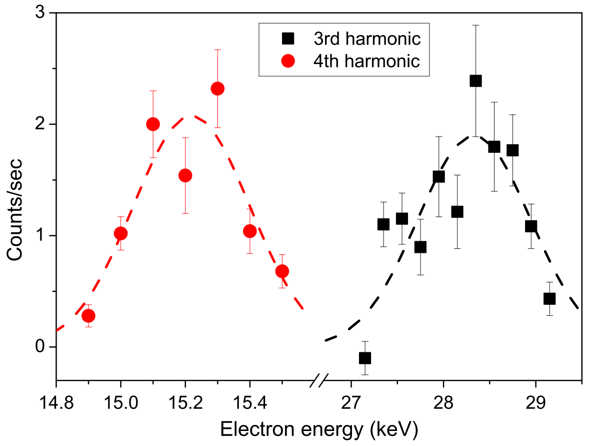

Figure 3. The rate of accelerated electron counts per second on the MCP screen for the 3rd and 4th harmonics as a function of incident electron kinetic energy. Maxima of the distribution correspond to phase synchronous acceleration.

gradients of 18 and 9 MeV m^{-1} for electrons travelling 20 nm above the surface of the grating. As a result, we expect smaller total energy gains. Second, it is clear that as the harmonic number increases, the $1/e$ transverse decay length decreases, consistent with the fact that it scales with $\beta\gamma\lambda$ [5]. Consequently, the requirements of electron beam transverse size and alignment with the DLA sample are stricter when higher harmonics are used. Further, the fraction of electrons that are accelerated is reduced for higher harmonics, as we discuss below.

2.1. Single grating subrelativistic acceleration: experimental setup

Our DLA experimental setup is described in detail in [7] and summarized here. A scanning electron microscope (SEM) column (Hitachi S-570) serves as a DC electron source with a tunable electron emission energy in the range of 5–30 keV. The width of the electron energy distribution at 28 keV is typically 10 eV. The beam is aligned so that it is parallel to the surface of transparent fused silica grating (grating period 750 nm) and focused by a condenser magnet so that the spot size ($1/e$ radius) is 70 nm at 28 keV and 250 nm at 9.6 keV. Femtosecond laser pulses from a long-cavity Ti:sapphire oscillator with a repetition rate of 2.7 MHz, a pulse length of 115 fs, a center wavelength of $\lambda = 787$ nm and a pulse energy of 160 nJ are used to excite the accelerating mode of the grating. The laser beam is focused to an elliptical spot shape with gaussian radii $w_1 = 8.6\ \mu$m, $w_2 = 3.6\ \mu$m and is perpendicularly incident on the grating surface in the geometry shown in figure 1. The long axis of the laser spot profile is parallel with the direction of electron travel. The spatial overlap between electron and laser beams was adjusted using the electron-induced scintillation of phosphorus grains deposited on the top of the substrate. The incident laser polarization is parallel to the electron propagation direction. After interaction with the laser field, electrons pass through a retarding field spectrometer that only allows the traversal of electrons that have gained energy. Transmitted electrons were detected by a micro channel plate (MCP) detector downstream of this effective energy filter. To decrease the background photon signal on the MCP, electrons were deflected by pair of coils and high energy photons emitted from the SEM column were blocked.

In our setup only a small fraction of the DC electron beam can interact with the short laser pulses. The effective electron current interacting with the laser beam can be written as $I_{\text{eff}} = I_{\text{b}}\tau_{\text{p}}f_{\text{rep}}$ where I_{b} is the electron current from the SEM column, and τ_{p} and f_{rep} are the pulse length and repetition rate of the incident laser respectively. Due to the fact that electrons sample all injection phases of the accelerating mode, accelerated electrons represent only a fraction of interacting electrons. To detect count rates on the order of one electron per second we used a time-resolved detection scheme where the time delay between each count on the MCP and the following laser pulse was measured by a time to digital conversion unit. Laser pulses were detected by an avalanche photodiode. The temporal resolution of this setup is 1–2 ns. The resulting time delays were plotted in a histogram (as shown in figures 4 (b) and (c)). The background counts (due to the MCP dark current, high energy photons and electrons emitted from the spectrometer) are equally distributed in time but the signal counts of accelerated electrons appear as a peak with a fixed time delay. To determine the count rate, the

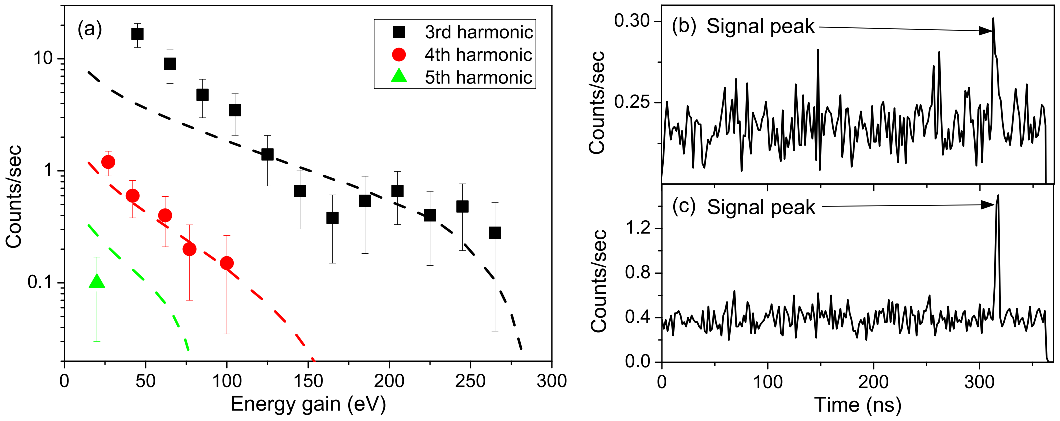

Figure 4. (a) The rate of accelerated electron counts per second on the MCP screen for the 3rd (black), 4th (red) and 5th (green) harmonic as a function of energy gain of the accelerated electrons. The resulting maximum field gradients are 27, 15 and 7.5 MeV m^{-1} respectively. (b) MCP integrated counts/sec as a function of time after part of the incident laser pulse was picked off and sent to a avalanche photodiode. The accelerated signal (corresponding to 9.6 keV electrons in (b) and 15.2 keV electrons in (c)) is at 320 ns.

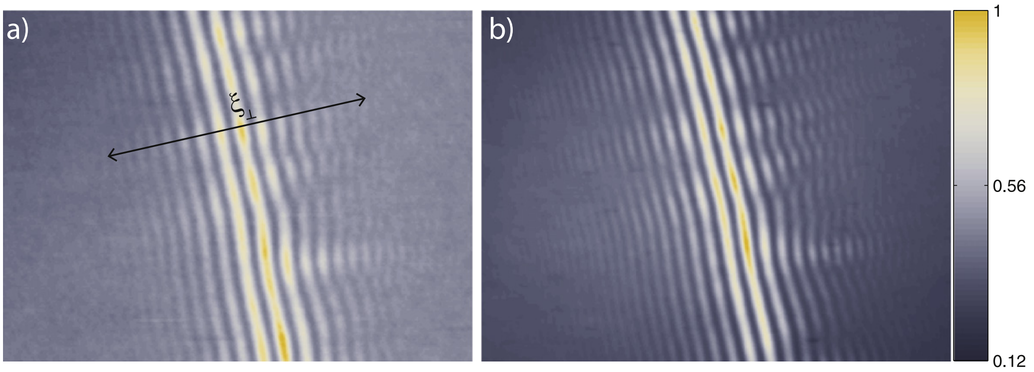

Figure 5. Evidence of transverse coherence of laser-triggered (a) and dc-field (b) emitted electrons, with the transverse coherence length $\xi_\perp$ highlighted. In the former case, the tip is held at –41 V as a near-uv laser (with a 3.1 eV photon energy) is focused onto the tip apex. In the latter case the tip is held at –53 V. To generate these interference fringes, the emitted electrons pass a freestanding carbon nanotube beam splitter placed in close vicinity to the tip and are then incident upon a downstream micro-channel plate detector. We note that this data is taken from the same data set used in [6], but with a different carbon nanotube position. For more details, see [6].

signal was then integrated over the peak width (a 3 ns time window) and the average background count rate was subtracted. The resulting signal was then divided by the integration time.

2.2. Single grating subrelativistic acceleration: results and discussion

In all accelerators working with time-dependent fields, synchronicity between the acceleration modes and electron velocity must be met for efficient operation. In the case of the DLA, electrons with β given by equation (1) feel the highest acceleration gradient. However, due to the spectral width of the incident laser pulses and the short interaction distance of the electrons and laser pulse, the energy acceptance of the DLA is non-zero. As we show in figure 3, the width of this distribution changes for different spatial harmonics. We compare count rates of accelerated electrons in dependence on initial electron beam energy for the 3rd (energy gain above 100 eV) and 4th (energy gain above 30 eV) spatial harmonic. Gaussian fits show FWHM widths of 1.4 keV for 3rd and 0.42 keV for 4th harmonic, respectively, corresponding to relative widths of the initial velocity distributions of 2.3% and 1.3%. Thus, when experimental conditions are kept constant (laser power, wavelength, spot size), the velocity 'acceptance' of electrons which can be accelerated becomes narrower for higher spatial harmonics. This can be explained as follows: The acceleration mode for mth spatial harmonic contains m oscillations per grating period. For an electron to be accelerated, it has to 'surf' on the accelerating wave. However, for higher spatial harmonics, the spatial distance between acceleration and deceleration fields decreases. Moreover, the interaction time increases because of smaller electron velocity. Therefore a smaller relative change in the electron initial velocity causes the electron to dephase from accelerating to decelerating fields; thus preventing efficient acceleration. Finally, we note that we obtain peak count rates for electron energies 28.4 and 15.2 keV. Further measurements have been carried out at these energies.

In figure 4(a) we show accelerated electron count rates as a function of the voltage difference between the retarding field spectrometer and the center of the electron beam energy distribution. This difference corresponds to a threshold energy gain of electrons detected at each point. Initial electron beam energies were 28.4, 15.2 and 9.6 keV for the 3rd–5th spatial harmonics, respectively. The measured data matches the theoretical curves obtained by FDTD simulations and particle tracking quite well. For our custom-made FDTD code, we use Yee's algorithm [8] with a cartesian grid with spatial and temporal sampling of 10 nm and 10 as respectively. Particle tracking was performed with standard finite difference methods.

In our calculations we took into account the dependence of the electron current and spot size on electron initial energy. Due to the significantly larger electron spot size at 9.6 keV, the electron density at the sample surface decreases. Moreover, our SEM electron energy cannot be tuned continuously in this energy region and we cannot reach the ideally synchronized electron energy for 5th harmonics (9.55 keV). This fact also contributes to the low count rate observed in the 5th harmonic measurement.

3. Laser-triggered nanotip electron source

The single grating DLA scheme requires excellent injector beam quality in order to obtain a small beam in close vicinity to the grating as the acceleration efficiency drops quickly on a typical length scale of one optical wavelength (more precisely, $\delta = \frac{\beta\gamma\lambda}{2\pi}$, see [5], typically on the order of 100 nm or less). In other DLA geometries such as the double grating geometry described in [4], merely transmitting the electron beam through the acceleration channel, typically 1 micron tall by 1 mm long, requires an electron beam with extraordinarily low divergence. Thus, an electron source exhibiting an emittance of well below 1 micron-rad is crucial.

The property of small emittance is related in a large degree with a large transverse coherence length [6]. The highest quality electron beams feature large transverse coherence lengths and a narrow energy spread along with a small emittance. Metal needle tips (nanotips) operated in (cold) dc-field emission are regarded as electron sources which perfectly meet these conditions for practical purposes [9]. They typically have apex radii of 10 ,..., 100 nm, which leads to a large static field enhancement. The underlying physics of the dc-field emission process is covered within the Fowler–Nordheim framework [10].

The transverse coherence length $\xi_\perp$ is defined as the distance between two points for which interference can still be observed. Employing the van Cittert–Zernicke theorem (see for example [11]), we obtain $\xi_\perp$ at a certain distance d from the source. This can be directly related to its (effective) radius r_{eff} as $\xi_\perp = (d \cdot \lambda_{\text{db}})/(\pi \cdot r_{\text{eff}})$, where λ_{db} is the de Broglie wavelength. Hence, the smaller the source the beam seems to be originating from, the larger the coherence width. Nanotips in dc-field emission typically exhibit values for r_{eff} on the order of 1 nm and below [12, 13], clearly smaller than the geometrical emission surface, which is quite remarkable as it means that there is already a non-zero coherence length at the emission site. Therefore these emitters are said to be partially coherent. As the beam quality does not only depend on the emission process (see e.g. thermal emission, Schottky emission and variants thereof), but also on the coherence of the electrons inside the conduction band [12], it has been unclear whether these well-known properties are preserved in a laser-triggered emission process—even though their use as an ultrafast electron source has been proposed almost a decade ago [14–16].

In a recent experiment [6] an upper bound for r_{eff} of a tungsten tip triggered by a near-UV laser (photon energy of 3.1 eV) has been obtained and directly compared to the value in dc-field emission. It has been shown the value of 0.8 nm for a tungsten tip of ~10 nm radius triggered by a laser beam in a one-photon emission process is quite comparable to the one obtained in dc-field emission (0.6 nm) from the same tip. Moreover, the geometric root mean square electron beam emittance at 44 eV is as low as 0.08 nm rad, corresponding to a normalized rms emittance of 1 nm mrad. For the purpose of DLA this renders a laser triggered needle tip emitter an ideal source, as a small beam diameter in close vicinity to the grating can be easily achieved with suitable electron optics, which ensures a homogeneous acceleration coefficient across the entire beam. Synchronization of the electron beam with the accelerating laser pulse is inherently given as the same (frequency doubled) laser beam can be used for triggering electron emission from the tip as for accelerating.

4. Proposed electron source

The aforementioned tip source is suitable for integration with a DLA section based on the subrelativistic acceleration presented above. Electrons are emitted from the tip with a normalized emittance of approximately 1 nm-mrad and a spot size that can be collimated to a size of less than 100 nm, suitable for traversing DLA accelerating regions with typical sizes of 100 s of nm. In the double grating structure described in [4], this means the electrons can easily traverse the structure without colliding with the walls of the accelerating channel. In the single grating structure described above, this means that the electrons can traverse the fields without bending away from the region in which accelerating field are significant.

In order to accelerate electrons to 10 keV (the lowest kinetic energy of electrons that have been accelerated via DLA interaction), we propose the use of a DC electric field generated by a –10.0 kV anode on the order of 1 mm away from the apex of a laser-triggered tungsten nanotip floating at –10.1 kV. Approximately 5 mm downstream of the –10 kV anode is an anode at –100 V, designed to accelerate the electrons to 10 keV while maintaining collimation. This separation distance between each element is dictated by the breakdown threshold of metal in vacuum (~25 MV m^{-1}) [17]

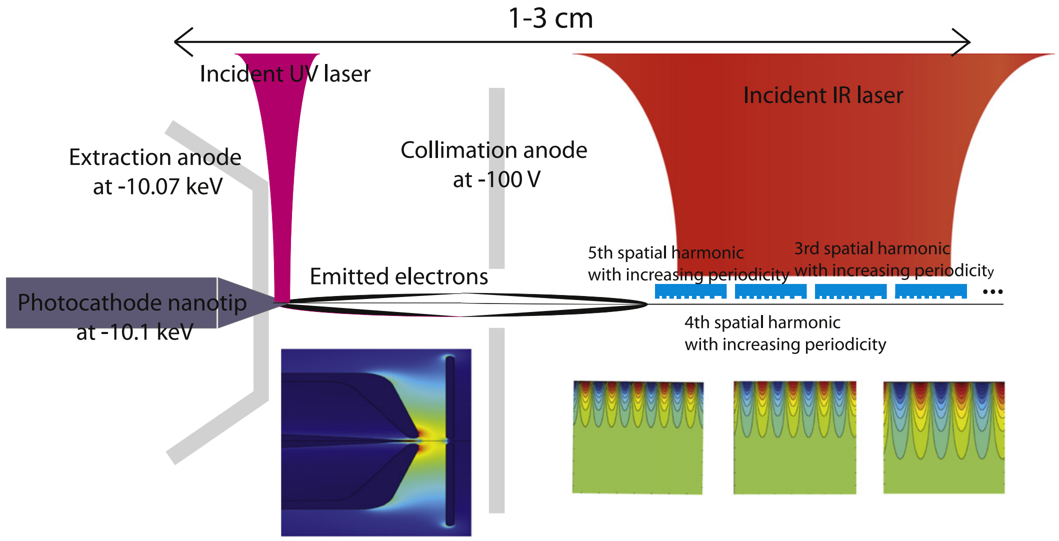

Figure 6. Proposed DLA-based electron source. Electrons that are accelerated to 10 keV by the DC photogun are then accelerated by multiple sections of DLA. Simulated fields in the gun section of the electron source are shown on the bottom left. Field strength is limited by breakdown of the metals composing the gun. Electrons leave the gun at 10 keV. The periodicity of the DLA sections is varied so that the phase velocity of the accelerating mode matches the increasing electron velocity.

as well as the dc field emission threshold at the laser-triggered tip (approximately 2 GV m^{-1}), taking into account the dc field enhancement at the 100 nm scale radius tip. A schematic of our proposed design is given in figure 6.

As mentioned above, it is critical that the electrons reaching the DLA components are collimated. Otherwise, they will either crash into the DLA structure or be thrown away from the strong accelerating fields. To achieve this collimation, we first consider the beam envelope equation [18]:

$$r_\mathrm{m}'' + \frac{\gamma' r_\mathrm{m}'}{\beta^2\gamma} + \frac{\gamma'' r_\mathrm{m}}{2\beta^2\gamma} + k_\mathrm{f} r_m - \frac{\epsilon_\mathrm{n}^2}{\beta^2\gamma^2 r_\mathrm{m}^3} - \frac{K}{r_\mathrm{m}} = 0. \qquad (2)$$

Here, ϵ_n is the normalized emittance, r_m is the beam radius, k_f is the transverse focusing coefficient due to external fields, and $K = 2I/(I_0\beta^3\gamma^3)$ is the generalized perveance, with the Budker or Alfvén current for electrons: $I_0 = 17\,000$ A. The perveance is a measure if the space charge effect [18, 19]. To determine the necessary focusing strength, we assume the case of balanced or Brillouin flow, in which a focusing lens balances the defocusing forces due to emittance and coulomb repulsion. That is, $r_m^{0000''} = \gamma' = 0$. By equating the focusing term with the perveance term in the resulting simplified beam envelope equation, we find that

$$k_\mathrm{f} = \frac{2I}{\beta^3\gamma^3 r_m^2 I_0}. \qquad (3)$$

By then assuming a kinetic energy of 10 keV, a beam radius of 100 nm and a space-charge limited peak current of 1 mA [5], we find that the required focusing strength is less than 0.1 $\mu\mathrm{m}^{-2}$. Such focusing forces are easily achievable for the electrostatic collimating gate scheme demonstrated in [21], for instance. By scaling down the design dimensions in [20], we expect the size of this gun (with collimating gates included) to be less than 2.5 cm in the direction of electron propagation. Simulated fields in figure 6 confirm this scaling.

Once electrons reach an energy of 10 keV, they are then injected into the DLA accelerating sections. As the electrons are accelerated, their velocities increase, and the geometry of the structure is modified to match the phase velocity of the accelerating mode to this increasing electron velocity. Additionally, when the electrons have reached an energy of 15 keV, the structure is adapted so that the 4th harmonic is the synchronous accelerating mode, when they reach 28 keV, the 3rd harmonic is the synchronous mode and so on. Within a few mm, the electrons can then reach energies approaching 1 MeV. To reach this energy in a small distance, the accelerating gradients will need to approach 100 s of MeV m^{-1}. Work is underway to improve the accelerating gradients at these low energies by changing the dielectric material (to silicon or anodic alumina, for instance), the geometric parameters of the grating, and the incident laser wavelength.

Moreover, the interaction distance between the electrons and the laser pulse will need to be increased by more than an order of magnitude. This requires a pulse energy that scales with the beam diameter squared (to operate slightly below the damage threshold of the material), and pulse front tilting of the intensity front of the incoming laser relative to its phase front. Pulse front tilting will remove the limitation on the interaction length imposed by the temporal pulse length of the incoming pulse [22].

A MeV electron source with a footprint of less than a cm can potentially be used for applications such as tumor or neuronal endplate irradiation. Such a device would fit on the end of a catheter or endoscope and could be used in a surgical setting [1]. However, to realize such a device, a few technical challenges must first be addressed. First, the electron beam produced by such a source must remain focused as it travels through the DLA (after it has exited the aforementioned external electrostatic focusing fields) even as it potentially sees the deflecting fields of the accelerating mode. To maintain beam collimation, the transverse forces of the DLA fields (experimentally detected in [3]) could be utilized to create focusing fields, such as those proposed in [22].

Finally, we note that the current produced from the nanotips will need to be increased in order to make for an effective tumor irradiation. In [6], single electron per pulse (and thus pA average current, depending on the repetition rate of the triggering laser) beams are proposed with the aforementioned emittance values. This emitted electron beam, when implemented in our proposed electron gun, is appropriate for applications such as ultrafast electron diffraction. However, for effective tumor irradiation for example, nA average currents are necessary. To achieve this, higher laser fluences will need to be used to trigger the emission. In [20], 2000 electrons per pulse were laser-triggered using a similar tungsten tip and a 6 fs 80 MHz Ti:Sappphire laser. Although the emission current remained stable over a time scale of 10 min, tip stability, potentially improved with a larger tip radius, will be further studied to ensure a robust electron source for potential DLA applications. Moreover, the assumption of Brillouin flow used to derive equation (3) is no longer valid, and more involved simulations will be implemented to fully characterize the particle dynamics of collimation.

5. Conclusion and outlook

We have demonstrated DLA-based acceleration of the slowest electrons tested with DLAs to date. The acceleration of electrons with energies as low as 10 kV, combined with new results demonstrating sub-nm emittance of electrons emitted from a laser-triggered tungsten nanotip leads to the possibility of a novel compact electron gun which is briefly described here. To fully realize the applications of such an electron source, future work is focused on beam collimation and generating sufficient currents from the laser-triggered tips.

Acknowledgments

This research is funded in part by the Gordon and Betty Moore Foundation Quantum Electron Microscope project, the DFG Cluster of Excellence Munich Centre for Advanced Photonics and the ERC Grant NearFieldAtto.

References

[1] England R J *et al* 2014 *Rev. Mod. Phys.* **86** 1337
[2] Breuer J and Hommelhoff P 2013 *Phys. Rev. Lett.* **111** 134803
[3] Leedle K, Pease R and Byer R L 2015 *Optica* **2** 158–61
[4] Peralta E A *et al* 2013 *Nature* **503** 91–4
[5] Breuer J, McNeur J and Hommelhoff P 2014 *J. Phys. B: At. Mol. Opt. Phys.* **47** 234004
[6] Ehberger D, Hammer J, Eisele M, Krüger M, Noe J, Hoegele A and Hommelhoff P 2015 *Phys. Rev. Lett.* **114** 227601
[7] Breuer J, Graf R, Apolonski A and Hommelhoff P 2014 *Phys. Rev. ST Accel. Beams* **17** 021301
[8] Yee K 1866 *IEEE Trans. Antennas Propag.* **14** 302–7
[9] Spence J 2013 *High-Resolution Electron Microscopy* (Oxford: Oxford University Press)
[10] Fowler R H and Nordheim L W 1928 *Proc. R. Soc.* A **119** 173
[11] Lichte H and Lehmann M 2008 *Rep. Prog. Phys.* **71** 016102
[12] Cho B, Ichimura T, Shimizu R and Oshima C 2004 *Phys. Rev. Lett.* **92** 246103
[13] Spence J, Qian W and Silverman M P 1994 *J. Vac. Sci. Technol.* A **12** 542
[14] Hommelhoff P, Sortais Y, Aghajani-Talesh A and Kasevich M A 2006 *Phys. Rev. Lett.* **96** 077401
[15] Hommelhoff P, Kealhofer C and Kasevich M A 2006 *Phys. Rev. Lett.* **97** 247402
[16] Ropers C, Solli D R, Schulz C P, Lienau C and Elsaesser T 2007 *Phys. Rev. Lett.* **98** 043907
[17] Alston L L 1968 *High Voltage Technology* (Oxford: Oxford University Press)
[18] Reiser M 2007 *Theory and Design of Charged Particle Beams* (New York: Wiley)
[19] Lawson J D 1958 Journal of Electronics and Control *J. Electron. Control* **5** 146
[20] Hoffrogge J, Stein J P, Kruger M, Forster M, Hammer J, Ehberger D, Baum P and Hommelhoff P 2014 *J. Appl. Phys.* **115** 094506
[21] Helfenstein P, Kirk E, Jefimovs K, Vogel T, Escher C, Fink H-W and Tsujino S 2011 *Appl. Phys. Lett.* **98** 061502
[22] Plettner T, Byer R L, McGuinness C and Hommelhoff P 2009 *Phys. Rev. ST Accel. Beams* **12** 101302
[23] Pai D M and Awada K A 1991 *J. Opt. Soc. Am.* A **8** 755–62

Additional publications

L. Assaud, J. Schumacher, A. Tafel, S. Bochmann, S. Christiansen and J. Bachmann, ”Systematic increase of electrocatalytic turnover at nanoporous platinum surfaces prepared by atomic layer deposition”, *Journal of Materials Chemistry A*, vol. 3, no. 16, pp. 8450-8458, sep 2015.

J. McNeur, M. Kozak, N. Schönenberger, A. Li, A. Tafel, and P. Hommelhoff, ”Laser-driven acceleration of subrelativistic electrons near a nanostructured dielectric grating: From acceleration via higher spatial harmonics to necessary elements of a dielectric accelerator,” *Nuclear Instruments and Methods in Physics Research Section A: Accelerators, Spectrometers, Detectors and Associated Equipment*, vol. 829, pp. 50-51, sep 2016.

U. Niedermayer, A. Adelmann, S. Bettoni, M. Calvi, M. Dehler, E. Ferrari, F. Frei, D. Hauenstein, B. Hermann, N. Hiller, R. Ischebeck, C. Lombosi, E. Prat, S. Reiche, L. Rivkin, R. Aßmann, U. Dorda, I. Hartl, W. Kuropka, F. Lemery, B. Marchetti, F. Mayet, H. Xuan, J. Zhu, D. S. Black, P. N. Broaddus, R. L. Byer, A. Ceballos, H. Deng, S. Fan, J. Harris, T. Hirano, T. W. Hughes, Y. Jiang, T. Langenstein, K. Leedle, Y. Miao, A. Ody, A. Pigott, N. Sapra, O. Solgaard, L. Su, S. Tan, J. Vuckovic, K. Yang, Z. Zhao, O. Boine-Frankenheim, T. Egenolf, E. Skär, D. Cesar, P. Musumeci, B. Naranjo, J. Rosenzweig, X. Shen, B. Cowan, R. J. England, Z. Huang, H. Cankaya, M. Fakhari, A. Fallahi, F. Kärtner, T. Feurer, P. Hommelhoff, J. Illmer, A. Li, A. Mittelbach, J. McNeur, N. Schönenberger, R. Shiloh, A. Tafel, P. Yousefi, M. Kozak, M. Qi, Y. J. Lee, Y.-C. Huang, and E. Simakov, ”Challenges in simulating beam dynamics of dielectric laser acceleration”, *International Journal of Modern Physics A*, vol. 34, p. 1942031, nov 2019.

Acknowledgment

This work would not have been possible without the support of many persons and I am deeply thankful to every single one of you.

Special thanks goes to my supervisors Prof. Peter Hommelhoff and Prof. Jürgen Risten. I enjoyed having all those long and fruitful discussions very much! Thank you very much for your openness, creativity and support. I value that your doors were always open, no matter what the topic was.

To all the co-authors who made this cumulative work possible: I do not take this for granted and I am very grateful for your support. You will always be a part of my (soon to be) title. Thank You!

I am very grateful for having so many great colleagues at work. Thank you for countless Hackysack sessions and for making the everyday work life even more enjoyable.

My dearest love goes to Marlene. Thank you for always having my back and for bringing so much joy to my life.

My dear family, I don't know where I would be without you in my life. Mom & Dad, I cannot even express how thankful I am for everything you helped me achieve and become.